Doctor of Philosophy

The Investigation into the Effective Strategies for Improving the Performance of Organic Solar Cells

The Graduate School
of the University of Ulsan
Department of Physics
Do Hui Kim

February 2022

The Investigation into the Effective Strategies for Improving the Performance of Organic Solar Cells

Supervisor : Shinuk Cho

A Dissertation
Submitted to
the Graduate School of the University of Ulsan
In partial Fulfillment of the Requirements
for the Degree of
Doctor of Philosophy
by

Do Hui Kim

Department of Physics
Ulsan, Korea

February 2022

The Investigation into the Effective Strategies for Improving the Performance of Organic Solar Cells

This certifies that the dissertation/thesis of Do Hui Kim is approved.

Committee Chair Dr. Sunglae Cho

Committee Member Dr. Shinuk Cho

Committee Member Dr. Young-Han Shin

Committee Member Dr. Teun-Teun Kim

Committee Member Dr. Dong Chan Lim

Department of Physics
Ulsan, Korea

February 2022

Abstract

Renewable energy has been developed to solve the serious issue of global climate change caused by increasing carbon dioxide emissions. Organic solar cells (OSCs) have attracted a lot of attention due to their potential for future energy source because of several advantages such as lightweight, low-cost production, and flexibility. Recently, the OSCs with high power conversion efficiency (PCE) over 18% have been realized with the introduction of non-fullerene acceptor (NFA) in which light absorption in near-infrared region (NIR) and adjustable chemical structure and energy level. However, higher PCE and better long-term stability are still required for the commercialization.

Operation principle of OSCs is based on photo-induced charge transfer. Photo generated holes and electrons initially forms the excitons, and these excitons are dissociated at the interface of donor and acceptor. Thus, the effective dissociation of excitons has a significant influence on the performance of OSCs. Created excitons must move to the interface of donor and acceptor to be dissociated. If the phase of each donor and acceptor is larger than the exciton diffusion length, excitons can be recombined before reaching the donor-acceptor interface. Therefore, optimizing the well phase separated morphology of photoactive layer is one of the essential factors to achieve high efficiency. In addition, elimination of various trap sites, including charge transfer state and interface trap, is also an essential factor to obtain higher efficiency and better stability. Thus, in this study, various technologies such as ternary blend, additive engineering, and interfacial treatment have been applied to improve the performance and ensure the stability of OSCs.

In first study, the ternary blend system was employed to diminish energy loss of a fullerene based OSCs. The photoactive layer with ternary blend system was formed by introducing the small molecule DRCN5T into binary system based on wide bandgap polymer donor PBDTTPD-HT and $PC_{71}BM$. It was constructed cascading charge transfer by DRCN5T acting as a bridge and enabled indirect electron transfer from PBDTTPD-HT to $PC_{71}BM$. As a result, a small amount of DRCN5T was introduced into PBDTTPD-HT:$PC_{71}BM$ to avoid the deep charge transfer state between PBDTTPD-HT and $PC_{71}BM$, thereby increasing V_{OC} and improving the efficiency of the device.

In second study, the solid-solvent hybrid additive method was applied to the photoactive layer based on PM6:Y6 for simultaneously optimizing both the macroscopic donor-acceptor phase separation and the microscopic morphology such as π-π stacking and orientation of the inside phase. The solvent additive, 1-chloronaphthalene (CN) was used to optimize the macroscopic donor-acceptor phase

separation and microscopic morphology was optimized using newly synthesized Star-A or Star-F with 3D structure as a solid additive. The effect of solid additive on morphology was confirmed through the measurements of grazing-incidence small-angle X-ray scattering (GISAXS) and grazing-incidence wide-angle X-ray scattering (GIWAXS), which showed enhanced microscopic intermolecular π-π stacking within the phase as well as optimize the phase separation. Therefore, the performance of OSCs was improved by optimizing the morphology of photoactive layer using 1% of small amount of solid additive.

In third study, in order to improve the performance of OSCs and ensure the long-term stability, the interfacial treatment method was applied. The deep trap generated at the interface between photoactive layer and metal oxide-based electron transport layer and shallow trap caused penetrated oxygen-containing defects increase trap-assisted recombination and reduce charge extraction efficiency, resulting in a decrease in V_{OC} and long-term stability of the device. To overcome this issue, the interfacial defect between photoactive layer and electron transport layer was suppressed by chemical modification, thereby the device efficiency was improved to 17.43% and the stability was maintained almost 90% after 1200 h for air storage.

In conclusion, by introducing various techniques, such as ternary blend system, additive engineering, and interfacial treatment to optimize the morphology of photoactive layer and suppressing the defect states, the OSCs with higher PCE and significantly improved stability were successfully demonstrated.

Table of Contents

List of Figures

List of Tables

List of Abbreviations

Abbreviation	Description
AFM	atomic force microscopy
BHJ	bulk-heterojunction
CB	chlorobenzene
CF	chloroform
CN	1-chloronaphthalene
CT	charge transfer
DIO	1,8-diiodooctane
DPE	diphenyl ether
EA	electron affinity
E_g	band gap
EL	electroluminescence
EQE	external quantum efficiency
ETL	electron transport layer
FF	fill factor
FRET	Förster resonance energy transfer
FTPS	Fourier-transform photocurrent spectroscopy
FWHM	full width at half maximum
GISAXS	grazing-incidence small-angle X-ray scattering
GIWAXS	grazing incidence wide angle X-ray scattering
G_{max}	exciton generation rate
HOMO	highest occupied molecular orbital
HTL	hole transport layer
ICL	intermediate connection layer
IMVS	intensity-modulated photovoltage spectroscopy
IP	ionized potential
IPA	isopropanol
IQE	internal quantum efficiency
ITO	indium tin oxide
J_{mpp}	maximum power point current density
J_{ph}	photocurrent density
J_{SC}	Short-circuit current
L_D	exciton diffusion length
LUMO	lowest unoccupied molecular orbital
MPP	maximum power point
NFA	non-fullerene acceptor
NIR	near-infrared
OOP	out-of-plane
OPVs	organic photovoltaics
OSC	organic solar cell

P_C	charge collection probability
PCE	power conversion efficiency
P(E, T)	exciton dissociation probability
PL	photoluminescence
R_s	series resistance
R_{sh}	shunt resistance
SCLC	space-charge-limited current
TCO	transparent conducting oxide
TPC	transient photocurrent
TPV	transient photovoltage
UPS	ultraviolet photoelectron spectroscopy
V_{eff}	effective voltage
V_{mpp}	maximum power point voltage
V_{OC}	open circuit voltage

Chapter 1. Introduction

1.1 Organic Solar Cells (OSCs)

1.1.1 Background of OSCs

Environmental issues such as the emission of carbon dioxide and global climate change have been emerged around the world with increased fossil fuel usage. Renewable energy technology has been developed to overcome these problems. Among the renewable energy resources, solar energy has been received a lot of attention particularly because it is eco-friendly and infinite source. Solar cells are devices that convert into electrical energy using these solar energy sources. Inorganic crystalline silicon solar cells have been widely distributed due to their relative higher power conversion efficiency (PCE) and superior price competitiveness. **(Figure 1.1)**[1] However, inorganic crystalline silicon solar cells are difficult to manufacture in various colors and have limitations in their applications to buildings. On the other hand, organic solar cells (OSCs) have diverse applicability owing to their advantages such as low-cost production, lightweight, flexibility, and semitransparency.

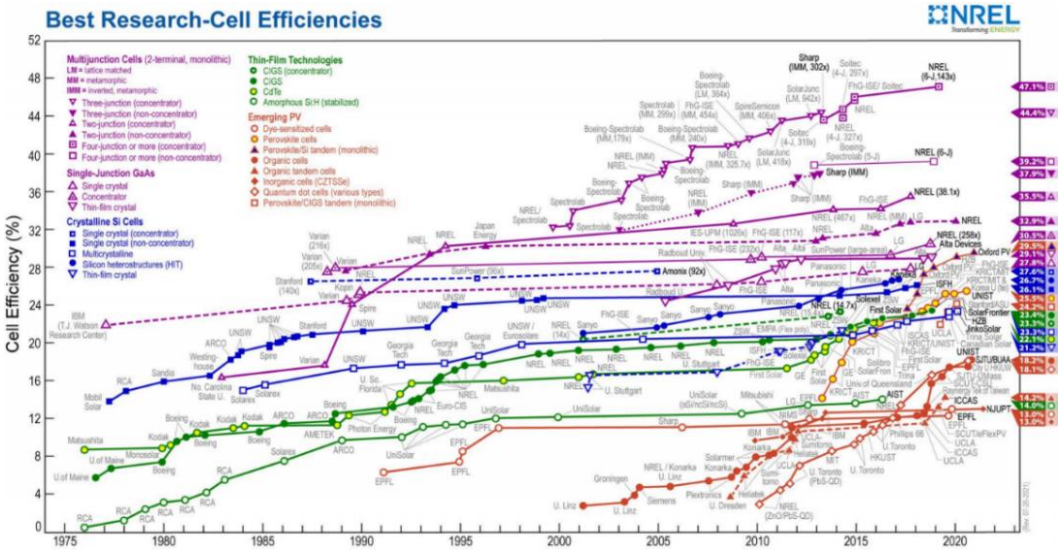

Figure 1.1. Chart of best research-cell efficiencies from National Renewable Energy Laboratory (NREL).

The history timeline of OSCs is represented in **Figure 1.2**. The structure of early OSC was a bilayer reported in 1986 by Tang, as shown in **Figure 1.3a**. Tang's OSC was constructed by stacking of a copper phthalocyanine (CuPc) and a perylene tetracarboxylic derivative between ITO anode and Al cathode, which had a PCE around 1%. It was an innovative result indicating that photovoltaic device was enabled through the p-n junction of organic semiconductor materials.[2] Saricifci discovered effective photoinduced electron charge transfer from the conjugated polymer to the fullerene derivatives of C_{60} in 1992.[3] This discovery indicated the possibility of OSCs using a composition of conjugated polymer and fullerene, and Yu first introduced the bulk-heterojunction (BHJ) structure into OSC in 1995 (**Figure 1.3b**).[4] The BHJ structure, which has more interfaces between donor and acceptor than the bilayer structure, has been dominantly used to date due to providing more efficient charge separation. In 2005, Li achieved the highest P3HT:PCBM solar cell with a PCE of 4.4% by improving the hole mobility and balanced charge transport.[5] As another approach to improve OSC performance, the tandem structure was tried to reduce the fundamental loss of light absorption. The tandem structure is composed of two BHJ active layers with different bandgaps, which are connected with intermediate connection layer (ICL), to cover the wide range of the solar spectrum (**Figure 1.3c**). In 2007, Kim achieved more than 6% PCE of tandem OSCs by introducing TiO_x layer as ICL.[6] However, even with the tandem structure, the wide coverage of the solar spectrum was still insufficient, requiring the development of novel light-absorbing materials.

To overcome the weaknesses of fullerene, for example of weak absorption in the visible region and limited energy level variability, non-fullerene acceptor (NFA) was designed and introduced in 2015.[7] After that, a simple and new strategy to form the active layer of OSCs has been developed, which is ternary OSCs, as showed in **Figure 1.3d**. Ternary OSC is the simplest way to overcome the limitation of light absorption compared to tandem OSCs. The active layer of ternary OSCs is comprised of three photoactive materials, such as two donors and one acceptor (D_1:D_2:A) or one donor and two acceptors (D:A_1:A_2). Xiao achieved a high performance ternary OSC (D:A_1:A_2) with a PCE of 14%.[8] In this case, fullerene was used as the third component of ternary active layer, resulted in enlarging light absorption, facilitating electron transport, reducing charge recombination, and optimizing morphology of the active layer. As shown in **Figure 1.1**, the highest PCE of 18.2% was certified from NREL at the most recent.[9] As described above, tremendous efforts such as various device structures and synthesizing novel photoactive materials, and so on, are being made to achieve further PCE improvements.

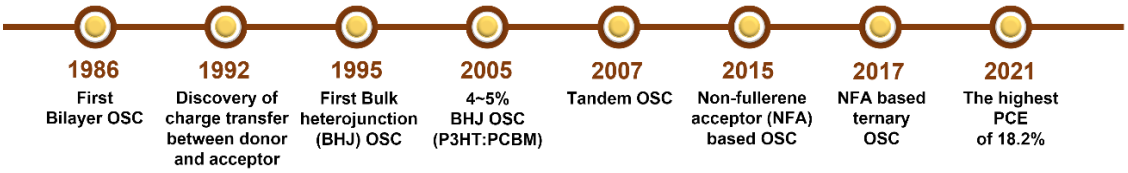

Figure 1.2. The history timeline of OSCs.

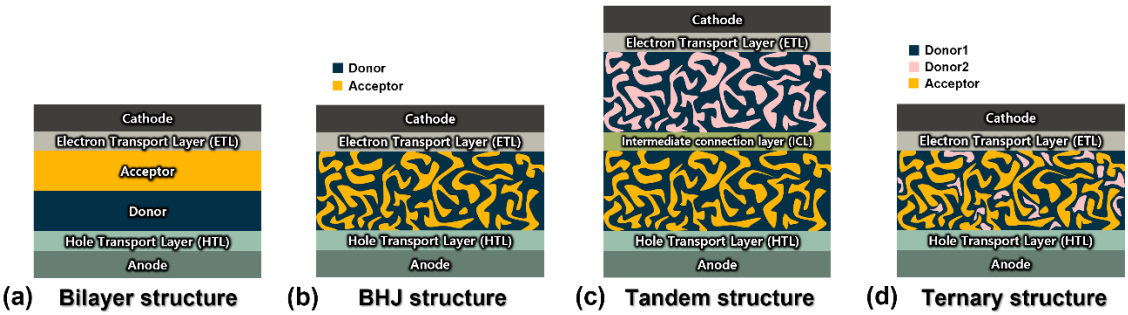

Figure 1.3. Various structures of OSCs. (a) Bilayer structure. (b) BHJ structure. (c) Tandem structure. (d) Ternary structure.

1.1.2 Working Principle of OSCs

Generally, BHJ OSCs are composed of two electrodes with different work functions and one active layer to absorb the photon energy. Normal structure of OSCs is anode/hole transport layer (HTL)/active layer/electron transport layer (ETL)/cathode. These OSCs convert photon energy into electrical photocurrent through the following four steps, as shown in **Figure 1.4**.

Step 1: Light absorption and exciton generation

Transparent conducting oxide (TCO) such as indium tin oxide (ITO) is usually used as an anode of OSCs to transmit the photon energy into the active layer. The other electrode, cathode, use Al or Ag which has high reflectivity and low work function. Photon energy transmitted into the active layer is absorbed depending on the properties of the materials (such as absorption spectra, absorption coefficient and so on) composed of the active layer. The active layer is consisted of donor and acceptor, of which

the polymer donor has a large bandgap and is limited in absorbing light in the long wavelength region. In order to compensate for this weakness of absorption, NFA that can absorb the long wavelength of solar spectrum has recently been developed, leading to a high photocurrent and PCE of OSCs. The high absorption coefficient of organic materials used as photoactive materials (over 10^5 cm^{-1}), requires a thin active layer thickness around 100 nm. Photon energy absorbed by organic materials forms exciton, which is electron and hole pair bounded by Coulombic force.

Step 2: Exciton diffusion

To dissociate into electron and hole, the exciton bounded with 0.3~0.4 eV is diffused to interface between donor and acceptor. In general, the exciton diffusion length (L_D) of organic materials is around 10~20 nm.[10] $L_D = \sqrt{D\tau}$, where D is diffusion coefficient and τ is lifetime of exciton. When L_D is longer than donor and acceptor phase separation length, the exciton is efficiently diffused, otherwise, it is recombined before reaching the interface between donor and acceptor.[11]

Step 3: Exciton dissociation

Exciton is dissociated at the interface between donor and acceptor. Since the exciton lifetime is short about 100 picoseconds (ps), adequate BHJ morphology is mandatory to efficiently dissociate the exciton. Exciton requires more energy than the coulombically binding energy in order to be dissociated to electron and hole. This energy depends on the offset between the highest occupied molecular orbital (HOMO) energy level of donor and the lowest unoccupied molecular orbital (LUMO) energy level of acceptor.

Step 4: Charge transport and collection

The dissociated electron and hole are transported to the electrodes by a built-in potential difference formed by a difference in work function between the cathode and anode. The electron is carried to acceptor material with high electron affinity, while the hole is transferred to donor materials. Electron and hole transported to each organic material are collected to the two electrodes, and charge transport layers are introduced for more efficient charge transfer. The HTL is inserted between the active layer and anode for efficient hole transportation, whereas the ETL, which helps electron transportation, is introduced at the interface between the active layer and cathode. To prevent charge recombination and efficient charge collection, high electron and hole mobility is required. The collected charges in the electrode flow through an external circuit and generate photocurrent.

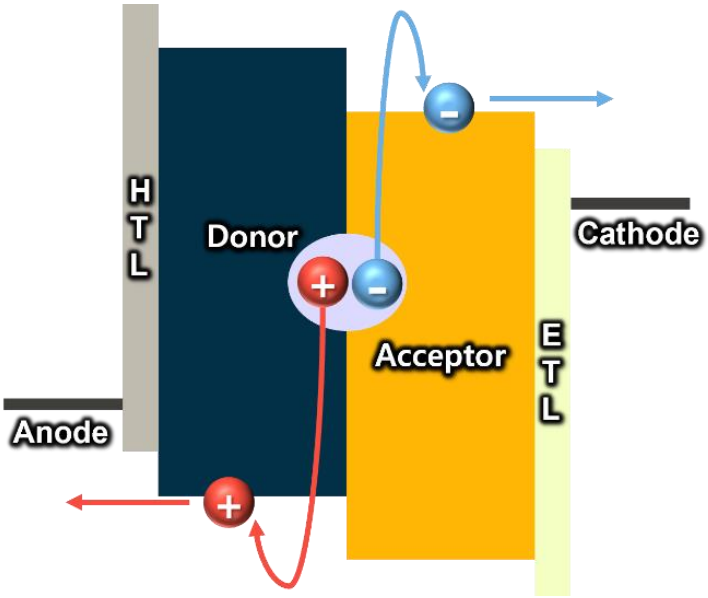

Figure 1.4. Working mechanism diagram of OSCs.

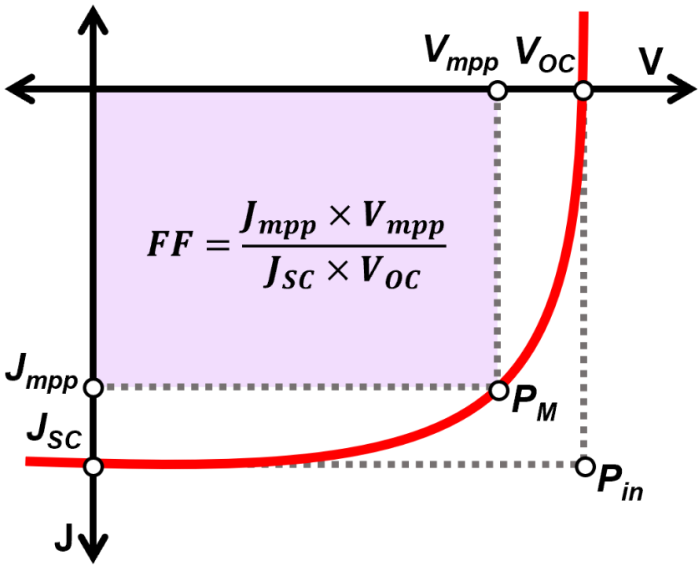

Figure 1.5. Current density-voltage (*J*-*V*) characteristics of OSCs under illumination.

1.1.3 Characterization of OSCs

The OSC is a diode that converts incident light into electrical energy. As shown in **Figure 1.5**, the operating efficiency of OSCs, called PCE, can be acquired from the current density-voltage (*J-V*) characteristic curves. The PCE can be determined by applying an external voltage under illumination of 1 sun (100 mW cm^{-2}) light intensity to measure the change in generating current in the OSCs. The PCE of OSCs is determined by following equation (1.1), where J_{SC} is short-circuit current density, V_{OC} is open-circuit voltage, *FF* is fill factor, P_{in} is the incident power and P_M is the maximum electrical power.[12]

$$PCE\ (\%) = \frac{P_M}{P_{in}} \times 100 = \frac{J_{SC}V_{OC}FF}{P_{in}} \times 100 \qquad \text{Equation (1.1)}$$

1.1.3.1 Short-circuit current density, J_{SC}

The ideal OSC represents electrical behavior by the Shockley diode equation (equation (1.2)).[13] However, the realistic OSC contains the issues of series (R_s) and shunt resistance (R_{sh}). The R_s describes bulk resistance within layers and the interfaces resistance between the organic layer and electrodes. The R_{sh} results from leakage current of OSCs due to film morphology including pinholes and trap states. A real OSC with these resistance elements is applied with equation (1.3).[14] The *n* is an ideal factor that represents how closely a diode behaves like an ideal diode. The J_0 is the saturation current density at reverse bias for an ideal diode, J_{ph} is the photogenerated current density, *V* is the voltage, *T* is the temperature, *e* is the elementary charge (1.6×10^{-19} C), and k_B is the Boltzmann constant, 1.38×10^{-23} $m^2kgs^{-2}K^{-1}$. The first term of equation (1.3) account for how a solar cell operates as a diode in the dark condition. The second term of equation (1.3) represents device leakages, due to parasitic current generated by pinholes. The optimized OSC has characteristics of small R_s and high R_{sh}.[5]

$$J(V) = J_0\left[exp\left(\frac{eV}{nk_BT} - 1\right)\right] \qquad \text{Equation (1.2)}$$

$$J(V) = J_0\left[exp\left(\frac{e(V-JR_s)}{nk_BT}\right) - 1\right] + \frac{V-JR_s}{R_{sh}} - J_{ph} \qquad \text{Equation (1.3)}$$

The short-circuit current density (J_{SC}) is the maximum photocurrent density produced by a device

under illumination at short-circuit conditions, which is primarily depended on the light absorption region and band gap (E_g) of photoactive materials. The small E_g of photoactive materials enable to absorb photons form the broad solar spectrum. In addition, J_{SC} is affected on efficiencies of exciton diffusion, exciton dissociation, charge transport, and charge collection.

1.1.3.2 Open-circuit voltage, V_{OC}

The open-circuit voltage (V_{OC}) is the maximum voltage acquired when generated current is zero. Under open-circuit conditions (V=V_{OC}, J=0), V_{OC} is expressed as equation (1.4) by assuming that infinitely larger R_{sh} than R_s.[15, 16]

$$V_{OC} = \frac{nk_BT}{q} \ln\left(\frac{J_{ph}}{J_0} + 1\right) \qquad \text{Equation (1.4)}$$

The energy offset between the HOMO level of the donor and the LUMO level of the acceptor determines the V_{OC} of OSCs. However, the actual V_{OC} of OSCs represents a value around 0.6 eV less than the difference of energy offset, which is higher than the energy loss of inorganic GaAs solar cells of 0.3 eV.[17] The distinction of 0.6 eV comes from the energy loss generating by charge separation from exciton to free charge. Reduction of energy loss is essential to achieve the high V_{OC} of OSCs. Above all, the selection of photoactive materials which has deep HOMO level of donor and shallow LUMO level of acceptor is important to accomplish of the highest V_{OC} of OSCs. In addition, in order to reduce the energy loss, it is essential to adjust the loss incurred during the recombination process of OSCs. The recombination loss of OSCs is divided in two types. The one is radiative recombination loss that dissipates the energy to emitting photons and the other is non-radiative recombination loss that dissipates the energy to thermal energy.[18] The non-radiative recombination loss is occurred by trap-assisted recombination, which is caused by defects acting as carrier traps at the interface between donor and acceptor. Thus, improving the crystallinity of molecules to suppress molecular vibrations and lowering the defect concentration to minimize the non-radiative loss is essential for optimizing the V_{OC} of OSCs.

1.1.3.3 Fill factor, *FF*

The fill factor (*FF*) indicates how easily the photogenerated charges can be extracted out of OSCs and describes the shape of *J-V* characteristics. It is defined as the ratio of the maximum power point current density (J_{mpp}) and voltage (V_{mpp}) to the product of J_{SC} and V_{OC}, as shown in equation (1.5).[19, 20]

$$FF = \frac{J_{mpp} \times V_{mpp}}{J_{SC} \times V_{OC}} \qquad \text{Equation (1.5)}$$

The ideal *FF* value reaches unity, however, in fact, the OSC has a value of 0.5~0.7, which is lower than that of the inorganic solar cells. This main reason is a recombination of OSCs, and in case of *FF*, it is caused by complex factors such as the behavior of excitons (formation, diffusion, and dissociation) and the transportation and collection of charge carriers. The optimal conditions for achieving the highest *FF* are minimized R_s and maximized R_{sh}. As mentioned in section 1.1.3.1, the R_s is generally affected by bulk resistance of active layer, buffer layer, and electrodes and contact resistance between each layer. It is obtained by the slope of *J-V* curve around V_{OC}. The R_{sh} that is obtained by the slope of *J-V* curve around J_{SC} indicates the current loss, for example, leakage current by the edge of the cell, pinholes, and traps.[19] It is ideal that the curve is close to a square, which means a high *FF*. To achieve the highest *FF*, it is essential to use an outstanding buffer layer diminishing the contact resistance and leakage current and enhance the crystallinity and mobility of photoactive materials.

1.2 Strategies to optimize the performance of OSCs

1.2.1 Ternary system for improving the characteristics of OSCs

Ternary system fabricated by introducing the third component into binary blend system is a simple strategy to obtain the high efficiency of OSCs. It has the effects of broadening the absorption range, optimizing blend morphology facilitated exciton dissociation and charge transport, and reducing energy loss through the single layer fabrication process. When selecting the third component of ternary system, the following conditions are considered to effectively boost the performance of the device; complementary absorption range and suitable energy levels between host components. As show in **Figure 1.6**, the location of the third component incorporated into binary blend system are categorized into four types: (1) positioned at the interface between host donor and acceptor, (2) embedded into the one phase of host donor or acceptor, (3) formed independent phase separated from the donor and acceptor phase, and (4) alloyed with the host donor.[21]

The operation mechanism of ternary systems is highly depended on the energy levels, bandgap, and the location of the third component formed in binary system, which is classified into charge transfer, energy transfer, parallel-like model, and alloy-like model.[22, 23] (**Figure 1.6**) The mechanism of charge transfer is applied when the HOMO and LUMO energy levels of the third component are located between the energy level of the host donor and acceptor, forming the cascade energy level alignment. The third component, in this system, serves as a carrier bridge and removes the charge traps by providing additional charge transfer pathways. Thus, charge recombination is suppressed and the charge transfer process is facilized, leading to improve the performance of the device. The energy transfer mechanism is caused by substantial overlapping between the emission spectrum of donor and the absorption spectrum of acceptor. Unlike the mechanism of charge transfer, in energy transfer mechanism, the third component cannot directly generate free charge, while functions as an energy transfer agent that delivers the excited exciton to host donor or acceptor through Förster resonance energy transfer (FRET) process. The third component harvests the solar photons and transfers the photogenerated excitons to the energy acceptor, in which the photoexcited excitons are dissociated more free charge carriers and generate higher current density. Therefore, energy transfer mechanism is attributed to enhancement of J_{SC} of the device.

The mechanisms of ternary system are classified according to the miscibility characteristics between third component and host materials (donor and acceptor), one of which is the parallel-like model. For example of D_1:D_2:A ternary system, this mechanism is applied when host donor (D_1) and guest donor (D_2) are immiscible and forms the independent charge transfer network. That is, it operated as parallel

connected two sub cell of D_1:A and D_2:A similarly to parallel-linked tandem cell. The V_{OC} in parallel-like model is depended on the composition ratio of third component rather than difference between the donor and acceptor energy levels, and lies between the V_{OC} values of the two binary systems. The other mechanism upon the miscibility between third component and host binary systems is alloy-like model. In case of ternary systems with D_1:D_2:A, the electrical alloy-like model is formed due to miscible between D_1 and D_2. The composite of two donors constructs a new charge transfer state depending on the averaged ionized potential (IP) or electron affinity (EA), leading of the V_{OC} variation.

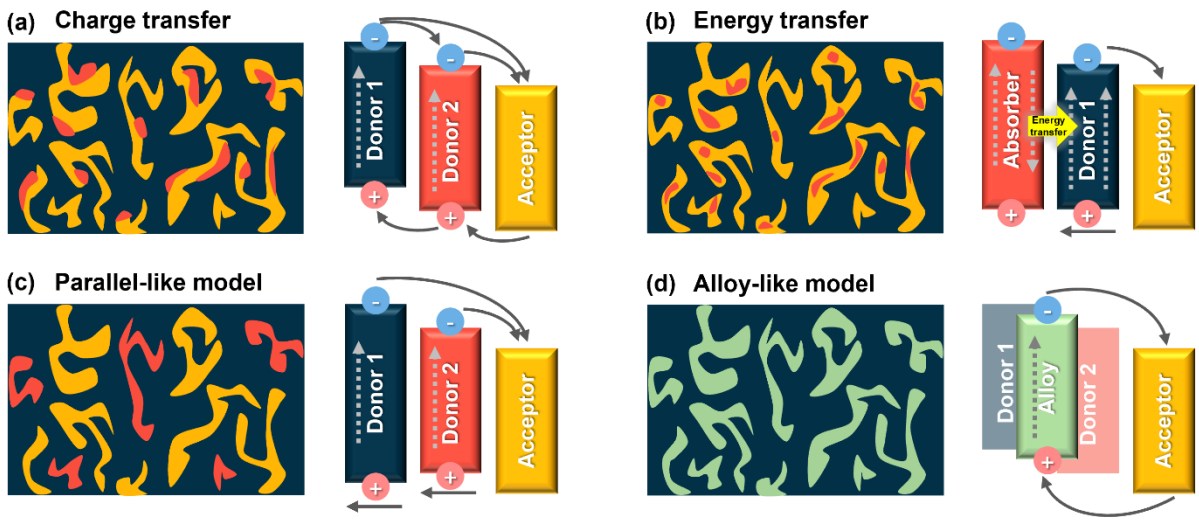

Figure 1.6. Morphology and working mechanism of ternary OSCs based on the blend of D_1:D_2:A.

The first the role of the third component in the ternary solar cell is to absorb a wide range of the solar spectrum. It is a crucial factor to influence the J_{SC} of the device for the reason that it is proportional to the number of absorbed photons. Koppe et al. first reported the ternary blend to increase the J_{SC} of the OSCs, introducing low bandgap polymer (PCPDTBT) into the blend system based on P3HT:PCBM.[24] The host donor, P3HT, which was a polymer with a high bandgap, had light response in a region below 650 nm, leading to a limitation in the efficiency of the device. By adding PCPDTBT as a third component with absorption range of absorbing up to 800 nm and well-matched energy level between P3HT and PCBM, the photocurrent generation in the near-infrared region (NIR) of the spectrum was increased, resulting in the improved J_{SC} and *FF* of the device.

Despite the recent tremendous development of NFA with absorption in NIR region, the OSCs still lose a large fraction of the whole solar spectrum. Li et al. synthesized a new acceptor molecule of GL1 with wide and strong absorption in the range from 600 to 1000 nm.[25] This novel material used as a third component into the binary OSCs based on polymer donor and NFA (PBDB-T:F-2Cl). Consequently, the ternary OSC was revealed the almost 10% increasement in J_{SC} compared to the binary OSC. The third component acts as a morphological regulator in ternary system, which is the second role of it. Huang et al. employed a small-molecule biomaterial of Gly-His-Lys-Cu (GHK-Cu) as a third component in the PBDB-T:ITIC binary system.[26] The exciton dissociation and charge transportation are closely related to the active film morphology, for examples of material crystallinity, phase separation, domain purity, and miscibility between donor and acceptor. However, the PBDB-T:ITIC binary system had a problem of low efficiency due to the inadequate phase separation between PBDB-T and ITIC as well as the weak crystallinity of ITIC. The way to use the GHK-Cu as third component reduced the miscibility and regulated the domain size of ITIC in the binary blend based on PBDB-T:ITIC, which inhibited trap-assisted recombination and increased and balanced the charge mobility. As a result, the efficiency of OSCs was improved by incorporating a small amount of GHK-Cu as a morphology regulator.

The third role of the third component is reducing the energy loss of OSCs. Another factor restricting the efficiency of OSCs is the energy loss, which is defined as $E_g^{opt} - eV_{OC}$ (where the E_g^{opt} is an optical bandgap of photoactive blend film and e is the elementary charge). The energy loss of OSCs is sorted into three parts[27]: (1) energy loss (ΔE_{CT}) occurred during charge transfer process related with the energetic offset between donor and acceptor components, (2) energy loss (ΔE_{rad}) caused by radiative recombination, which is unavoidable in all types of a solar cell according to Shockley-Quisser (SQ) limit, (3) the energy loss (ΔE_{nr}) due to non-radiative recombination, which is correlated with the external electroluminescence quantum efficiency (EQE_{EL}) of the device; $\Delta E_{nr} = -kT\ln(EQE_{EL})$. Among these, the reduction of radiative recombination is almost inevitable, while the non-radiative recombination is suppressed by synthesizing new materials of donor or acceptor and optimizing the morphology of photoactive layer. Liu et al. exhibited a small ΔE_{nr} by incorporating a novel material of high crystalline small molecule donor, BTTzR, into PM6:Y6.[27] The third component of BTTzR possessed the synergetic effects of minimizing ΔE_{nr} and optimizing the blend active layer morphology with more compact molecular stacking, suitable domain purity and domain size. Bi et al. introduced HDO-4Cl into the host binary blend of PBDB-TF:eC9, which is formed an alloy-like HDO-4Cl:eC9.[28] Compared with binary system, the ternary system showed an increased exciton diffusion length that has a significant correlation with J_{SC} from 12.2 to 16.3 nm and exhibited obviously suppressed ΔE_{nr}.

Consequently, Bi et al. revealed the effective way using the ternary strategy to reduce the ΔE_{nr} by regulating the exciton behaviors.

1.2.2 Additive method for optimizing the morphology of photoactive layer

The morphology of photoactive layer has a significant impact on the efficiency of OSCs. The exciton generated by absorbing light energy is separated at the interface of donor and acceptor. If the phases of donor and acceptor are large pure phases, the exciton would undergo geminate recombination prior to reaching the donor and acceptor interface due to the average diffusion length of exciton is only from 5 to 20 nm.[29] These unideal morphologies of photoactive layer such as insufficient or excessive phase separation and lack of ordering of domains consequently lead to a decrease in efficiency. Therefore, the optimization of photoactive layer morphology is a critical factor to achieve the high efficiency of OSCs. To realize the enhanced morphology of photoactive layer, a numerous of approaches have been suggested such as post-thermal annealing, solvent annealing, and additives. Among them, the additive method has advantages of being able to finely adjust morphological properties through the selection of appropriate additive and effectively manipulate the molecular order, orientation, and phase separation of the domain. Types of additives include solvent additives and volatile or nonvolatile solid additives.

Solvent additive, which typically has a higher boiling point than main solvent, enhances the ordering of molecules and enriches the morphology by using the affinity on the component forming the photoactive layer. Materials commonly used as solvent additives include 1.8-diiodooctane (DIO), diphenyl ether (DPE), and 1-chloronaphthalene (CN), which should be selected in consideration of the solubility and boiling point of solvent additives.[30] DIO improves the morphology by selectively dissolving the acceptor so that the dissolved acceptor can be penetrated to the domain of the donor polymer. On the other hand, DPE and CN have co-soluble properties that dissolve not only acceptor but also donor, which enhance the crystallinity and form an outstanding charge transport channel, hence reduces bimolecular recombination. Zhao et al. demonstrated the importance of solvent additive selection by introducing two types of additives, DIO and CN.[31] Comparing to DIO in which only dissolve $PC_{71}BM$, CN for dissolving both polymer donor (PffBT4T-2OD) and $PC_{71}BM$ improved the crystallinity in the (100) direction, which was the alkyl stacking peak of the polymer donor, enhancing the charge transport and increasing *FF* and J_{SC}. In general, chloroform (CF) and chlorobenzene (CB), which are most used as main solvents of photoactive layer, have superior solubility for donor and acceptor materials and low boiling point. However, due to the low boiling point of main solvents, the unstable film morphology is formed by rapidly evaporating of the main solvent during film formation.

This issue is overcome by introducing a solvent additive with a high boiling point to delay drying process and form appropriate self-organization. Like this, the solvent additives can easily tune the morphology of photoactive layer, while the high boiling point of solvent additives cause an issue in the long-term stability of OSCs. Solvent additives with a high boiling point are not completely removed from the blend of photoactive materials. Therefore, when exposed to the light of air, the device is rapidly degraded by residual solvent additives and causes a change in morphology of photoactive layer which reduces the efficiency of OSCs.[32, 33] The unstable morphology caused by evaporation of residual solvent additives during device operation increases the charge recombination, resulting in the activation of the device degradation.

Solid additives refined the drawbacks of solvents additives are categorized into two types of volatile and non-volatile solid additives. First of all, the volatile solid additives are evaporated at the appropriate temperatures in comparison to solvent additives. Such characteristics of volatile solid additives can not only ensure the stability of the device, but also improve charge transport by improving intermolecular π- π stacking.[34] Yu et al. examined the effect of solid additive with different volatilizes on morphology of photoactive layer and device stability.[35] The SA-4 and SA-7 with similar chemical structures and different volatilize were synthesized and applied as solid additives. They determined that both SA-4 and SA-7 enable to enhance the molecular arrangements and π- π interactions of the acceptor (IT-4F) molecules, resulting in promoted absorption and electron mobility. Nevertheless, the device with SA-4 exhibited more improved photovoltaic performance and stability than the device with SA-7 owing to the high volatility of SA-4. The SA-7 solid additive with low volatility caused the incomplete volatilization from photoactive layer, leading negative effect on the morphology and poor deterioration of device performance. As described above, if the solid additive is not completely volatilized through thermal annealing treatment, it remains in the photoactive layer or aggregated on the surface of photoactive film. Thus, it is necessary to novel solid additive with outstanding volatility or non-volatility with stable in thermal.

Non-volatile solid additive is not affected by the manufacturing environment such as temperature and humidity to ensure consistency in morphology of photoactive layer and performance of the device. Liu et al. reported a non-volatile solid additive, chlorine-functionalized graphdiyne (GCl), which was stable within a wide range of temperatures.[36] GCl served as nucleation center improved the ordering of Y6 and enhanced the electron mobility by changing the crystallization habit during film condensation. In addition, the photoactive film used GCl exhibited more pronounced phase separation, resulting in an improvement in exciton dissociation property. Fan et al. applied the bifunctional bis-benzophenone (BP-BP) as non-volatile solid additive, which enabled regulation of the morphology and crystallinity by

remaining in the photoactive blend film.[37] Consequently, the device with BP-BP represented not only balanced the charge mobility of electrons and holes, but also improved charge collection ability by modifying π- π stacking of polymer donor (PBDB-T), with a face-on orientation.

Additive method used only one additive material mainly affects one phase of donor or acceptor, which causes shortcoming that difficult to fine-tune of photoactive morphology. As an alternative of this issue, the binary additive method using two types of additives is suggested. It is possible to finely adjust morphology by selecting two suitable additives. However, as the two additives are used, the efficiency of device can be elevated by considering an appropriate combination of additives. He et al. reported the promoted efficiency of OSCs with the binary additive, CN and DIO.[38] The two additives of DIO and CN were exhibited different solubility for acceptor. DIO with poor solubility for acceptor (IDCIC) used as acceptor induced aggregation and increased the domain size and domain purity of FTAZ:IDCIC blend film, while CN with tremendous solubility for IDCIC inhibited aggregation and molecular packing, inducing the diffusion of IDCIC into FTAZ, hence reduced the domain size and domain purity. In conclusion, the various additive methods as mentioned above will be an effective strategy to facilitate morphology optimization when utilizing the advantages of each additive.

1.2.3 Interfacial treatment to enhance stability of OSCs

For the commercialization of OSCs in the near future, the issue of device stability must be overcome. There are some factors that limit the stability, for instance, unstable morphology of photoactive layer, diffusion of electrodes and buffer layer, oxygen and water, irradiation, heating, and mechanical stress. Among them, the most dominant factors affecting the device stability when actual operation of OSCs are oxygen, moisture, and irradiation. The penetrated oxygen in the photoactive layer induces the photo-oxidation reaction with donor and acceptor materials, leading to the change of absorption property, energy level, and charge carrier mobility. Moreover, the oxygen doping in the photoactive layer cause the increased hole concentration, which decreased the FF and V_{OC} of the device owing to the increase of the deep trap density.

The moisture also affects to the stability of the device. When the moisture penetrates into the device, it interacts with fullerene and induces excessive aggregation. It decreases the interface between donor and acceptor, resulting in reduced exciton dissociation and degradation of the performance of OSCs.[39] The OSCs has instability under long-term irradiation, which is mainly caused by photochemical degradation due to the photo-oxidation in the photoactive layer. The photo-oxidation reaction affects the change of structure and energy alignment of donor and acceptor materials. It forms the sub-bandgap

states of materials, which increase the energetic disorder in the photoactive layer and diminish the electric field for facilitating charge separation. Peter et al. demonstrated the formation of sub-band states of active layer causing the degradation of efficiency, through the device of PCDTBT:$PC_{70}BM$ operating over 100 h.[40] The generated sub-band states of exposed over long-term irradiation cause trap-mediated recombination, reduce mobility, and increase the space-charge in traps, resulting in lower stability. Clarke et al. also reported the photodegradation mechanism of OSCs.[41] They exhibited that the exposure of device into the light induces a deep and broader charge carrier trap state, which leads to enhancing the trapped charge carrier and charge recombination.

To resolve these stability issues, the researchers have been developed various strategies, such as synthesized the novel materials, device engineering of the active layer, optimizing buffer layers, and so on. The instability of OSCs based on fullerene is mostly attributed to the morphology of the photoactive film. Li et al. demonstrated the correlation between device stability and morphology stability of photoactive layer by comparing fullerene and non-fullerene acceptor.[42] The P3HT:$PC_{61}BM$ film induces numerous aggregates after thermal treatment, whereas the P3HT:$SF(DPPB)_4$ remains homogeneous morphology and no aggregation is revealed due to the near amorphous nature of $SF(DPPB)_4$. Such unstable morphology has a major influence on device performance. In fact, the device stability examination showed a similar tendency with the result of morphology stability. The device using NFA of $SF(DPPB)_4$ showed almost 80% higher stability than the device with fullerene after thermal treatment over 150 min.

In contrast, the degradation mechanism of OSCs used NFA is apparently different compared to the device with fullerene. The stability of NFA based OSCs is hindered by the chemical interactions with interface materials. Among those strategies to improve the stability as mentioned above, the method of optimizing interfacial layer is more suitable for NFA based OSCs. Jiang et al. reported the enhanced device stability by replacing the electron transporting layer (ETL) from ZnO to SnO_2.[43] The ZnO had a photocatalytic activity under UV region, leading to the degraded stability of device. The photocatalytic activity of ZnO disrupted the C=C linkage in non-fullerene acceptors, which caused a disappearance of the intramolecular charge transfer absorption bands. In contrast, the SnO_2 with a wide bandgap appeared mitigated photocatalytic effect due to transparency in UV region, resulting in improved photostability of device by using SnO_2 instead of ZnO. Wang et al. demonstrated that the unavoidable interfacial reaction between PEDOT:PSS and ITIC caused the decrease of the built-in potential across photoactive layer and instability of device.[44] As an alternative, MoO_3 interfacial passivation layer was utilized to suppress an inevitable reaction in PEDOT:PSS with ITIC, leading to the enhanced long-term stability of device.

Chapter 2. Elimination of Charge Transfer Energy Loss by Introducing a Small-Molecule Secondary Donor into Fullerene-Based Polymer Solar Cells

2.1 Research background

Organic solar cells based on bulk heterojunction (BHJ) mixtures of organic semiconducting donor and acceptor materials have attracted considerable attention as a promising energy source for future mobile devices due to their advantages of low cost, flexibility, and processability.[45-47] However, the relatively poor long-term stability and low efficiency of this technology are serious drawbacks that must be addressed to allow commercialization.[48-50] Tremendous effort has been devoted to efficiency improvements by means including the development of higher-quality donor and acceptor materials,[51-53] morphology control of active layers,[54-56] and interface engineering for improved energy alignment.[57, 58] As a result, organic BHJ solar cell efficiencies have steadily increased since the first organic BHJ solar cell was reported in 1995.[4, 59]

After the first achievement of over 10% power conversion efficiency (PCE) in 2014, from an organic BHJ solar cell based on a blend of PTB7-Th and $PC_{71}BM$,[60] the efficiency of organic photovoltaics (OPVs) remained around 10% for several years. The large energy losses of fullerene-based acceptor materials such as $PC_{61}BM$ and $PC_{71}BM$ have been cited as a reason for this stagnation. However, an absence of alternative acceptor materials to fullerene derivatives persisted as an obstacle to increased efficiency.[61-63] This problem was eventually overcome through the development of high-quality non-fullerene acceptors (NFAs) such as ITIC, IDIC, and Y6, leading to the recent achievement of PCEs over 16%.[64-66]

Energy loss (E_{loss}) in organic solar cells is mainly analyzed in three terms: energy loss during charge transfer (ΔE_{CT}), radiative loss (ΔE_r), and nonradiative loss (ΔE_{nr}):[67]

$$E_{loss} = \Delta E_{CT} + \Delta E_r + \Delta E_{nr} = E_g - qV_{OC} \qquad \text{Equation (2.1)}$$

where E_g is the energy band gap, q is the electron charge, and V_{oc} is the open circuit voltage. In

general, the total E_{loss} of a fullerene-based solar cell is known to be greater than 0.7 eV, of which ΔE_{CT} > 0.3 eV and ΔE_{nr} is 0.3–0.4 eV.[68] In the case of solar cells based on NFAs, the total E_{loss} of NFA-based organic solar cells is 0.6 eV or less, of which ΔE_{CT} is 0.1–0.2 eV and ΔE_{nr} is 0.2–0.3 eV.[69] The E_{loss} of organic solar cells based on NFAs is known to be less than that of the solar cells based on fullerene acceptors. The lower E_{loss} in NFA-based solar cells is generally attributed to the greater molecular volumes and greater dielectricities of NFAs. The greater molecular volumes of NFAs result in lower exciton binding energies compared to fullerene acceptors, and thus in lower ΔE_{CT}.[70] In addition, the higher dielectricities of NFAs correspond to weaker intermolecular couplings and lower intermolecular reorganization energies during non-radiative recombination.[71] Ultimately, a minimum energy offset between the charge transfer (CT) state and the singlet exciton state is required for the effective dissociation of excitons to free holes and electrons. However, this energy offset limits the maximum V_{oc} that can be achieved. NFAs have relatively small energy offsets compared to fullerene acceptors, and thus produce less energy loss by increasing the energy of the CT state and reducing ΔE_{nr}.[18, 72]

Similar trends have been observed in many previous studies. In the case of solar cells using the PTB7-Th donor, although the PCEs were rather low with NFAs, V_{oc} tended to increase.[73, 74] In the case of using the wide-band-gap PBDB-T polymer, the overall performance of the solar cell was improved by using NFA due to increases in both V_{oc} and short-circuit current (J_{sc}).[73-75] Another wide-band-gap polymer, PBDTTPD-HT, also showed enhanced performance due to a reduction in E_{loss} resulting from the use of an NFA.[34] A solar cell based on PBDTTPD-HT:$PC_{71}BM$ showed the relatively low PCE of 7.3%. However, a solar cell based on PBDTTPD-HT:ITIC showed the enhanced PCE of 10.2% due to lower E_{loss} (with a corresponding increase of V_{oc} from 0.88 to 0.97 V).[76] According to several reports, it seems clear that NFA has the advantage of reducing E_{loss} while also offering strong absorption in the visible region and tunable energy levels.[73-75] If so, can't the problem of energy loss also be avoided when using a fullerene acceptor?

So far, several approaches that diminish recombination loss through enhancement of film morphology and decrease trap states through improvement of crystallinity of active components have been suggested as means to improve V_{oc} while reducing E_{loss}.[68-70] However, the adjustment of trap density through morphology control has an inevitable limit. Thus, in this work, we attempted the use of a ternary configuration as an alternative way to eliminate the effect of E_{loss} in fullerene-based BHJ solar cells. To avoid the miscibility problem between the active materials, we designed the configuration of the ternary active layer to have a primary polymer donor, a secondary small-molecule donor, and a fullerene acceptor. The operation concept was very simple: by adding the secondary small molecule donor, electrons are not transported directly from the primary polymer donor to the fullerene acceptor,

but instead are transported indirectly through the small-molecule donor (See **Figure 2.1**).

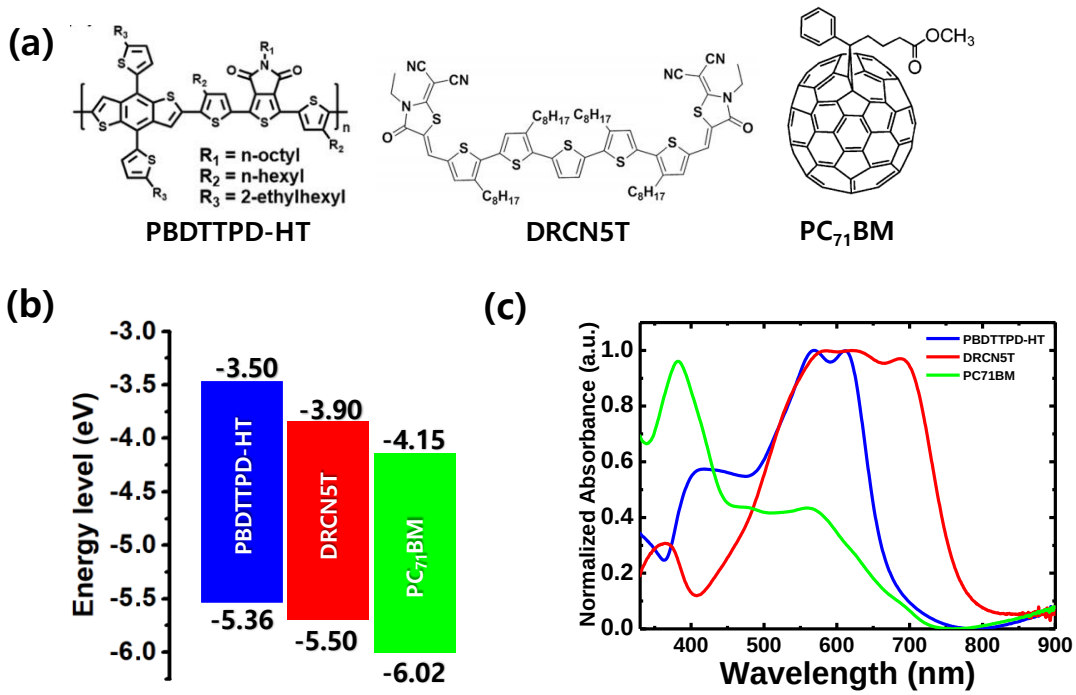

Figure 2.1. (a) Chemical structures of active materials PBDTTPD-HT, DRCN5T and $PC_{71}BM$. (b) Energy level diagram of ternary blended materials. (c) Normalized absorption spectra of PBDTTPD-HT, DRCN5T, and $PC_{71}BM$ films.

In the present work, we utilized DRCN5T as the secondary small-molecular donor.[77] DRCN5T has a wide absorption range and a good absorption coefficient, with an absorption onset of 800 nm. Thus, if the photoactive layer is composed of a polymer having a wide band gap, more light can be absorbed from a wider spectral region. Moreover, the composition DRCN5T:$PC_{71}BM$ has the low energy loss (ΔE_{CT}) of 0.03 eV because of its high E_{CT} level, which is close to the energy of the singlet state of DRCN5T.[78] Therefore, if electrons excited in the primary polymer donor pass through the DRCN5T to the $PC_{71}BM$, it would be possible to avoid the energy loss occurring during direct transport from the primary polymer donor to the fullerene. In a ternary system based on the wide-band-gap polymer PBDTTPD-HT, the small molecule DRCN5T, and $PC_{71}BM$, cascading charge transfer from PBDTTPD-HT through DRCN5T to $PC_{71}BM$ was observed. Consequently, the incorporation of a small amount of

DRCN5T as a secondary donor into the PBDTTPD-HT:$PC_{71}BM$ system induced an enhancement of PCE, which was mostly attributed to enhancement of V_{oc} arising from the elimination of charge transfer energy loss.

2.2 Experiment

Fabrication of ternary organic solar cells:

Patterned ITO glass substrates were cleaned by means of sequential ultrasonic treatment with acetone and isopropanol (IPA) and then dried in an oven overnight at 100 °C, followed by UV-ozone treatment for 1 h. PEDOT:PSS (Heraeus, AI 4083) was spin coated at 5,000 rpm onto pretreated ITO substrate and annealed at 150 °C for 10 min. PEDOT:PSS-coated substrates were transferred in an N_2-filled glove box and coated with the active layer using a PBDTTPD-HT:$PC_{71}BM$ binary blend solution (1:1.4, w:w) or PBDTTPD-HT:DRCN5T:$PC_{71}BM$ ternary blend solution (1:0.2:1.4, w:w:w) in chloroform with 0.8 vol% of 1,8-diiodooctane (DIO) at 4,000 rpm for 40 s. The ETL was then formed by spin coating a dilute ZnO nanoparticle solution (2.5 wt%) in IPA (1:10, v:v) at 5,000 rpm for 30 s, followed by annealing at 80 °C for 10 min. Finally, a 100 nm aluminum layer was deposited by means of thermal evaporation at 2×10^{-6} Torr.

Solar cell characterization:

The J–V characteristics of the binary and ternary OSCs were measured using a Keithley 2401 source measurement unit under AM 1.5G simulated illumination (100 mW cm^{-2}). The simulated light intensity was corrected by using a standard Si photodiode detector with a KG-3 filter (Newport Co., Oriel). External quantum efficiency (EQE) and internal quantum efficiency (IQE) were measured using a solar cell spectral response/QE/IPCE measurement system (Newport Co., Oriel IQE-200B). The light intensity at each wavelength was calibrated using a standard single-crystal Si photovoltaic cell. Absorption spectra were measured using a UV/Vis spectrometer (Varian, Cary 5000).

GIWAXS measurements:

GIWAXS was measured at the Pohang Accelerator Laboratory on the PLSII- 9A U-SAXS beamline; the beam of wavelength 0.1103 nm was incident on the samples at the angle of 0.13°. GIWAXS patterns were estimated with a charge-coupled device (CCD) detector (Rayonix SX165, PI-SCX: 4300).

AFM measurements:

The surface morphologies of the binary blend film based on PBDTTPD-HT:$PC_{71}BM$ and of ternary blend films incorporating various amounts of DRCN5T were measured by means of AFM. AFM images (scan area: 2 μm × 2 μm) were obtained using a Seiko E-Sweep atomic force microscope operated in tapping mode.

Impedance spectroscopy:

The recombination times of binary and ternary OSCs were measured by means of IVMS by using an impedance analyzer (IVIUM tech., IviumStat) operated in the frequency range from 1 MHz to 1 Hz. The DC and AC components of the illumination were provided by using an LED of wavelength 635 nm, where the modulation depth of the AC component superimposed on the DC light was 10%. IMVS was carried out under open-circuit conditions and the recombination times were calculated as $\tau_r = 1/(2\pi f_{min})$. The frequency-dependent capacitance was measured by means of impedance spectroscopy (IVIUM tech., IviumStat) at zero bias under dark conditions over the frequency range from 1 MHz to 1 Hz.

2.3 Results and discussion

Figure 2.1a shows the chemical structures of the active materials used in this study. Synthesis and characterization details of PBDTTPD-HT have been reported previously.[76] **Figure 2.1b** shows the schematic energy band diagram of the active materials. The highest occupied molecular orbital (HOMO) level and the lowest unoccupied molecular orbital (LUMO) of the primary polymer donor PBDTTPD-HT are −5.36 and −3.50, respectively.[76] The HOMO and LUMO energy levels of $PC_{71}BM$ are −6.02 and −4.15 eV, respectively.[76, 79] In the case of DRCN5T, it is known that the HOMO energy level is −5.50 eV, and the LUMO energy level is −3.90 eV,[77] both of which are between those of PBDTTPD-HT and $PC_{71}BM$. Therefore, DRCN5T satisfies the basic condition for cascade charge transfer in the ternary system. In addition, DRCN5T has a wide and absorption range, from 400 to 800 nm (**Figure 2.1c**). Thus, it can be said that DRCN5T complements well the binary composition of PBDTTPD-HT and $PC_{71}BM$, both optically and electrically.

The secondary donor DRCN5T was configured in conventionally structured solar cell devices with PBDTTPD-HT and $PC_{71}BM$ (**Figure 2.2a**). PEDOT:PSS was used as a hole transport layer, and ZnO

was utilized as an electron transport layer. The current density–voltage (*J*–*V*) characteristics of both a binary solar cell (b-SC) with PBDTTPD-HT:$PC_{71}BM$ and a ternary solar cell (t-SC) with PBDTTPD-HT:DRCN5T:$PC_{71}BM$ were measured under AM 1.5G illumination of light at an intensity of 100 mW/cm^2 (**Figure 2.2b and Table 2.1**). Experimental results related to the optimal incorporation ratio of DRCN5T are shown in **Figure 2.3** and **Table 2.2**. Direct comparison of *J*–*V* characteristics between b-SC, without DRCN5T, and t-SC, with 0.2 wt% DRCN5T, indicated that the overall photovoltaic performance of t-SC with DRCN5T was significantly better, with enhancement of parameters J_{sc}, *FF*, and V_{oc}. The b-SC cell, without DRCN5T, yielded PCE of 7.72%, J_{sc} of 12.4 mA/cm^2, V_{oc} of 0.869 V, and *FF* of 0.714, whereas the t-SC cell, with DRCN5T, yielded PCE of 9.08%, J_{sc} of 13.0 mA/cm^2, V_{oc} of 0.929 V, and *FF* of 0.749.

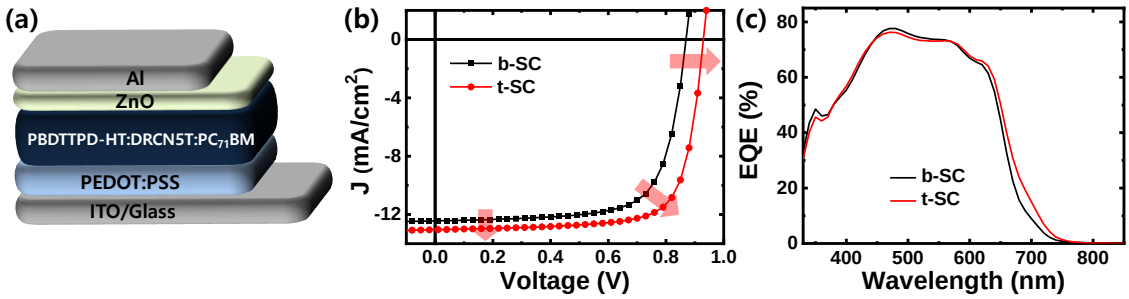

Figure 2.2. (a) Schematic illustration of solar cell structure. (b) *J*–*V* characteristics of b-SC and t-SC. (c) EQE spectra of b-SC and t-SC.

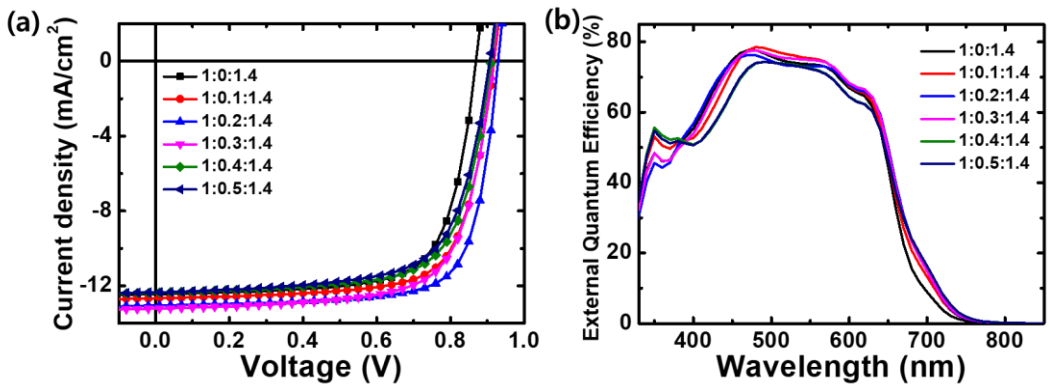

Figure 2.3. (a) Current density–voltage (J–V) characteristics and (b) external quantum efficien cy spectra of OSCs including various contents of DRCN5T.

Table 2.1. Summary of photovoltaic parameters of PBDTTPD-HT:$PC_{71}BM$ (binary) and PBDT TPD-HT:DRCN5T:$PC_{71}BM$ (ternary) solar cells.

	J_{SC} [mA cm^{-2}]	$J_{SC\text{-}EQE}$ [mA cm^{-2}]	V_{OC} [V]	FF	PCE [%]
PBDTTPD-HT:$PC_{71}BM$	12.4	12.2	0.869	0.714	7.72
PBDTTPD-HT :DRCN5T:$PC_{71}BM$	13.0	12.8	0.929	0.749	9.08

Table 2.2. Summary of photovoltaic parameters of PBDTTPD-HT:$PC_{71}BM$ (b-SC) and PBDTT PD-HT:DRCN5T:$PC_{71}BM$ (t-SC) including various contents of DRCN5T.

PBDTTPD-HT:DRCN5T:$PC_{71}BM$	J_{SC} [mA cm^{-2}]	V_{OC} [V]	FF	PCE [%]
1:0:1.4	12.4	0.869	0.714	7.72
1:0.1:1.4	12.7	0.918	0.721	8.38
1:0.2:1.4	13.1	0.929	0.749	9.08
1:0.3:1.4	13.2	0.915	0.706	8.54
1:0.4:1.4	12.4	0.911	0.702	7.90
1:0.5:1.4	12.3	0.907	0.687	7.69

To explore the influence of the additional absorption of DRCN5T upon J_{sc} in detail, J–V curves were replotted with net photocurrent density (J_{ph}) versus effective voltage (V_{eff}) as shown in **Figure 2.4a**. J_{ph} is defined as $J_{ph} = J_L - J_D$, where J_L is the current density measured under illumination and J_D is the current density measured in darkness. Dark current density is plotted in **Figure 2.4b**. V_{eff} is defined as $V_{eff} = V_0 - V_a$, where V_0 is the voltage when $J_{ph} = 0$, and V_a is the applied bias voltage.[80, 81] Saturation of

J_{ph} indicates that all photogenerated excitons are dissociated and collected without any bimolecular recombination. In this condition, saturation current density (J_{sat}) is governed by the incident photon flux only; thus the exciton generation rate (G_{max}) is simply given by $J_{sat} = q \cdot L \cdot G_{max}$, where q and L are respectively the elementary charge and the thickness of the active layer. In addition, the charge separation probability (P(E,T)) can be extracted using the ratio J_{ph}/J_{sat}.[81] Extracted G_{max} and P(E,T) values are listed in **Table 2.3**. Comparison between b-SC and t-SC indicated that t-SC, with DRCN5T, exhibited slightly increased G_{max}, from 7.56×10^{27} $m^{-3}s^{-1}$ to 7.95×10^{27} $m^{-3}s^{-1}$. Interestingly, P(E,T) also increased from 94.3% for b-SC to 97.5% for t-SC. This increase in G_{max} was attributed simply to the additional absorption of DRCN5T. However, the increase in P(E,T) could not be attributed solely to absorption enhancement.

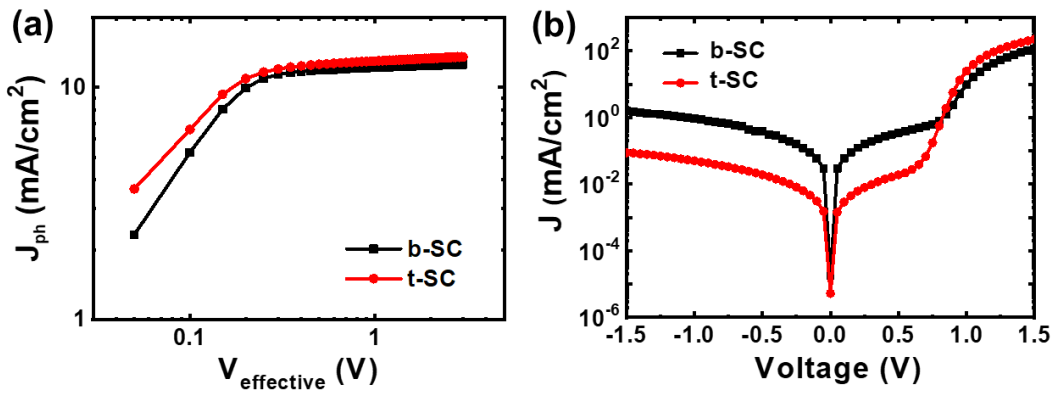

Figure 2.4. (a) Photocurrent density (J_{ph}) versus effective voltage (V_{eff}). (b) J–V measured und er dark conditions.

Table 2.3. Exciton generation rate (G_{max}) and charge separation probabilities (P(E,T)) of b-SC and t-SC.

	G_{max} [m^{-3} s^{-1}]	P(E,T)
PBDTTPD-HT:$PC_{71}BM$	7.56×10^{27}	94.3%
PBDTTPD-HT:DRCN5T:$PC_{71}BM$	7.95×10^{27}	97.5%

P(E,T) (i.e., the ratio J_{ph}/J_{sat}) is basically influenced by either exciton dissociation efficiency or charge collection efficiency. One of the significant factors that can influence the charge collection efficiency is the charge carrier mobility. So, to investigate hole and electron mobility, we measured space-charge-limited current (SCLC) using hole- and electron-only devices as shown in **Figure 2.5** in the Supporting Information.[82, 83] The hole-only and electron-only devices were constructed respectively in the following structures: ITO/PEDOT:PSS/active layer/MoO_3/Ag and ITO/ZnO/active layer/Al. The estimated hole and electron mobilities of b-SC and t-SC are presented in **Table 2.4**. The extracted hole mobilities were 9.1×10^{-5} $cm^2V^{-1}s^{-1}$ for b-SC and 1.8×10^{-4} $cm^2V^{-1}s^{-1}$ for t-SC. In the case of electron mobility, the extracted values were 4.3×10^{-6} $cm^2V^{-1}s^{-1}$ for b-SC and 1.0×10^{-5} $cm^2V^{-1}s^{-1}$ for t-SC. Although both hole and electron mobilities were slightly increased by the incorporation of DRCN5T, this was not enough to raise P(E,T) to the observed level. Rather, the observed increase in P(E,T) was most likely due to a direct increase in exciton dissociation efficiency.

The slight increase observed in hole and electron mobilities seems to have been due to the change in morphology. Although the surface morphology observed by means of atomic force microscopy (AFM) did not show any significant differences (**Figure 2.6**), further study using grazing incidence wide angle X-ray scattering (GIWAXS) data showed slightly changed crystallinity and π–π stacking orientation in t-SC. **Figure 2.7** shows the 2D GIWAXS pattern images and out-of-plane line cuts of PBDTTPD-HT, $PC_{71}BM$, PBDTTPD-HT:$PC_{71}BM$, and PBDTTPD-HT:DRCN5T:$PC_{71}BM$. The neat PBDTTPD-HT film exhibited a (010) π–π stacking reflection peak in the out-of-plane (OOP) direction at $q_z = 1.644$ $Å^{-1}$.[79] Compared to the neat film, the PBDTTPD-HT:$PC_{71}BM$ binary blend film exhibited very weak π–π stacking peaks in the OOP direction, indicating that the $PC_{71}BM$ disturbed the crystallinity of PBDTTPD-HT. However, the ternary blend film consisted of PBDTTPD-HT:DRCN5T:$PC_{71}BM$ exhibited an obviously increased intensity of the π–π stacking peak in the OOP direction, which indicated that the crystallinity of PBDTTPD-HT with a face-on orientation was recovered by incorporating DRCN5T. Thus, the small increase in mobility appears to be due to this change in crystallinity.

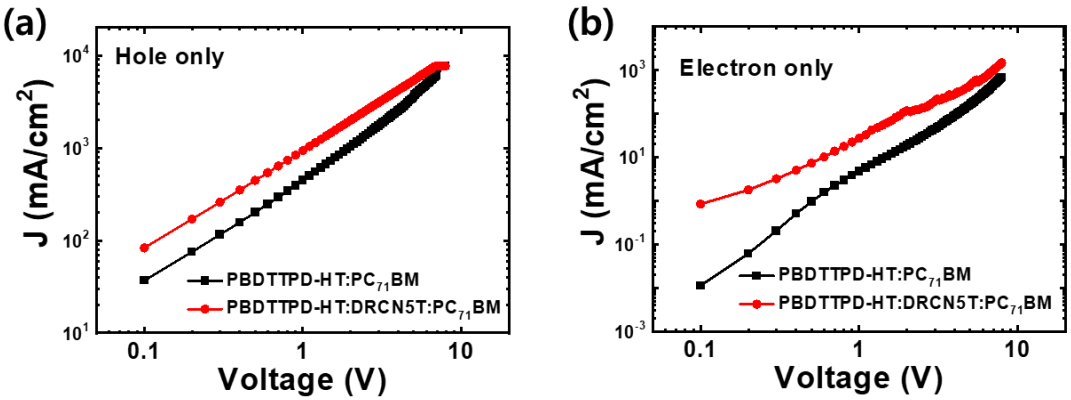

Figure 2.5. J–V characteristics of (a) a hole-only device and (b) an electron-only device.

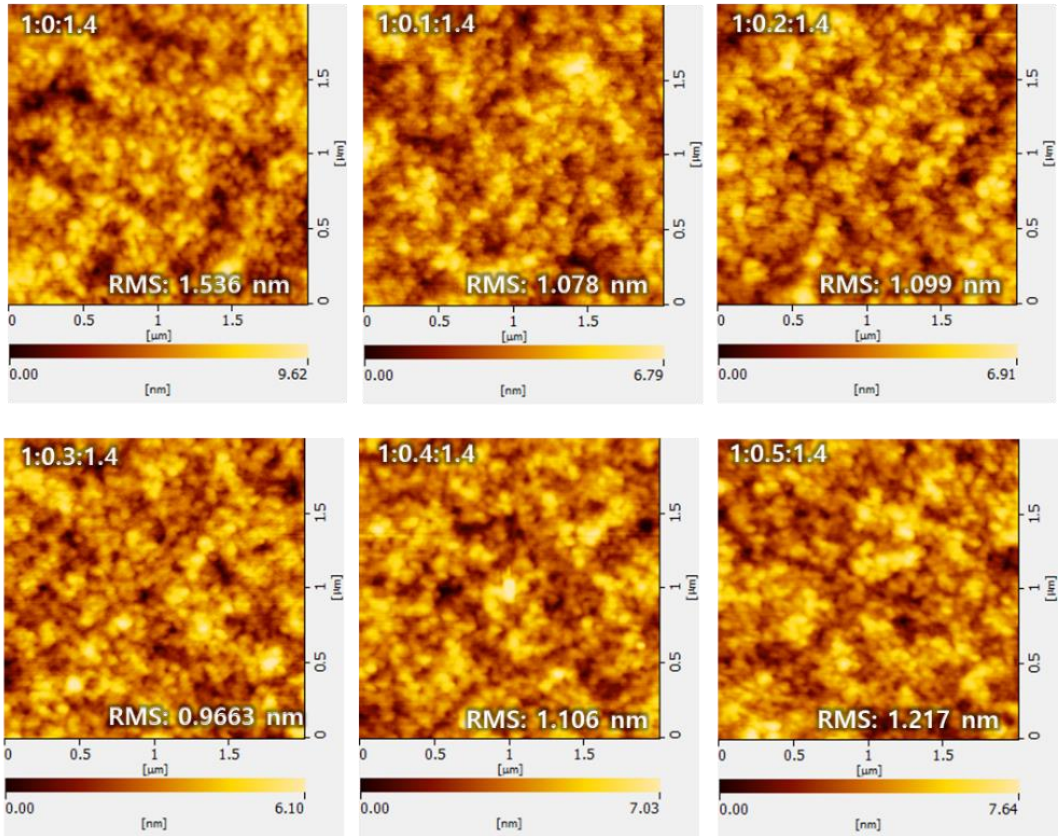

Figure 2.6. Atomic force micrographs of binary and ternary blend films including various contents of DRCN5T.

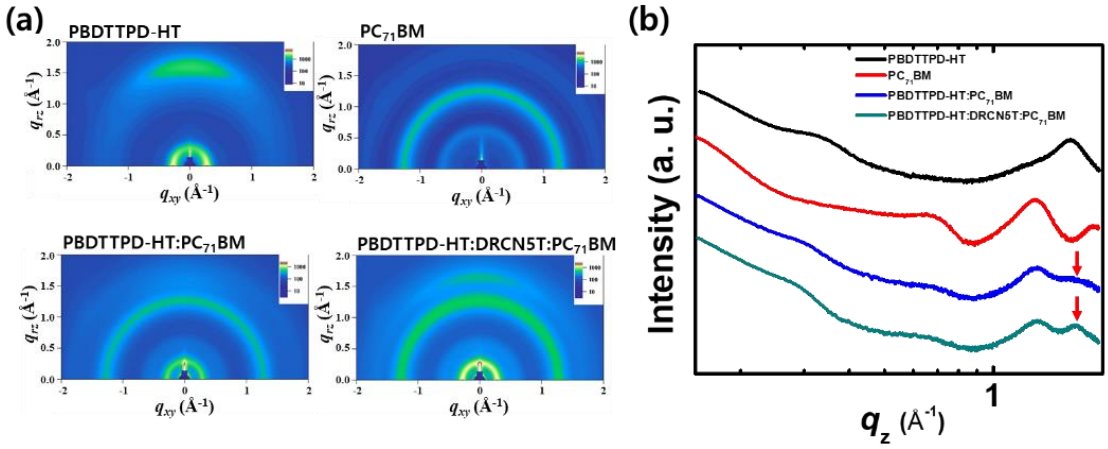

Figure 2.7. (a) 2D pattern GIWAXS images and (b) out-of-plane line cuts of PBDTTPD-HT, $PC_{71}BM$, PBDTTPD-HT:$PC_{71}BM$, and PBDTTPD-TH:DRCN5T:$PC_{71}BM$.

Table 2.4. Hole and electron mobilities of b-SC and t-SC.

	μ_h [$cm^2V^{-1}S^{-1}$]	μ_e [$cm^2V^{-1}S^{-1}$]
b-SC	9.1×10^{-5}	4.3×10^{-6}
t-SC	1.8×10^{-4}	1.0×10^{-5}

Another possible interpretation of the increase in *P*(E,T) is that the charge carriers created in the primary donor PBDTTPD-HT may have transferred to the DRCN5T. If the electron transfers directly to $PC_{71}BM$, the probability of geminate recombination and trap-assisted bimolecular recombination through CT states increases, which causes energy loss in BHJ solar cells. However, since the composition of DRCN5T:$PC_{71}BM$ produces a high E_{CT} level that is close to the energy of the singlet state of DRCN5T,[78] if the charge carriers transfer to $PC_{71}BM$ through DRCN5T, recombination mediated by the CT state can be reduced, resulting in increased charge separation probability. To confirm the cascading transfer from PBDTTPD-HT to DRCN5T, we performed photoluminescence (PL) measurements as shown in **Figure 2.8a**. The emission peaks of neat PBDTTPD-HT and DRCN5T were

at 710 and 759 nm, respectively. Although a portion of these PL spectra overlapped slightly, there seems to be no problem in distinguishing which part of the spectrum is attributable to which material. For the PBDTTPD-HT:DRCN5T film without the $PC_{71}BM$ acceptor, PL peaks originating from DRCN5T were only observed with increased intensity, whereas the PL peak of PBDTTPD-HT almost disappeared. Such PL results clearly indicate that there was charge transfer between the two donors PBDTTPD-HT and DRCN5T.

There are two transport models to describe the V_{oc} in ternary solar cells: the parallel-transport model and the cascade-transport model. In parallel-transport t-SC devices, in which absorption and exciton dissociation occur individually, V_{oc} lies between the values of the binary blends, and the V_{oc} is often to close that of the b-SC with the lowest V_{oc}.[21, 79] Actually, in a similar ternary configuration consisting of PTB7-Th:DRCN5T:$PC_{71}BM$, which obeys the parallel-transport model,[84] V_{oc} was close to (and higher than) that of a PTB7-Th:$PC_{71}BM$ binary device. Thus, the PCE improvement observed in the parallel-transport t-SC device is mainly attributable to an improvement in J_{sc}. However, in our t-SC, the addition of the DRCN5T induced an increase in all photovoltaic parameters (V_{oc}, J_{sc}, FF) simultaneously; among these, the increase in V_{oc} was particularly noticeable. In addition, the measured V_{oc} was closer to the V_{oc} of the DRCN5T:$PC_{71}BM$ binary device (see **Figure 2.9**) than that of the PBDTTPD-HT:$PC_{71}BM$ binary device. If the cascading charge transfer were incomplete and coexisted with parallel transport, the V_{oc} of the ternary device would have been altered by the effective energy levels of the two donors. Therefore, the finding of the same V_{oc} value for PBDTTPD-HT:DRCN5T:$PC_{71}BM$ t-SC and DRCN5T:$PC_{71}BM$ b-SC indicates that most charges were transferred by means of the complete cascading mechanism though DRCN5T.

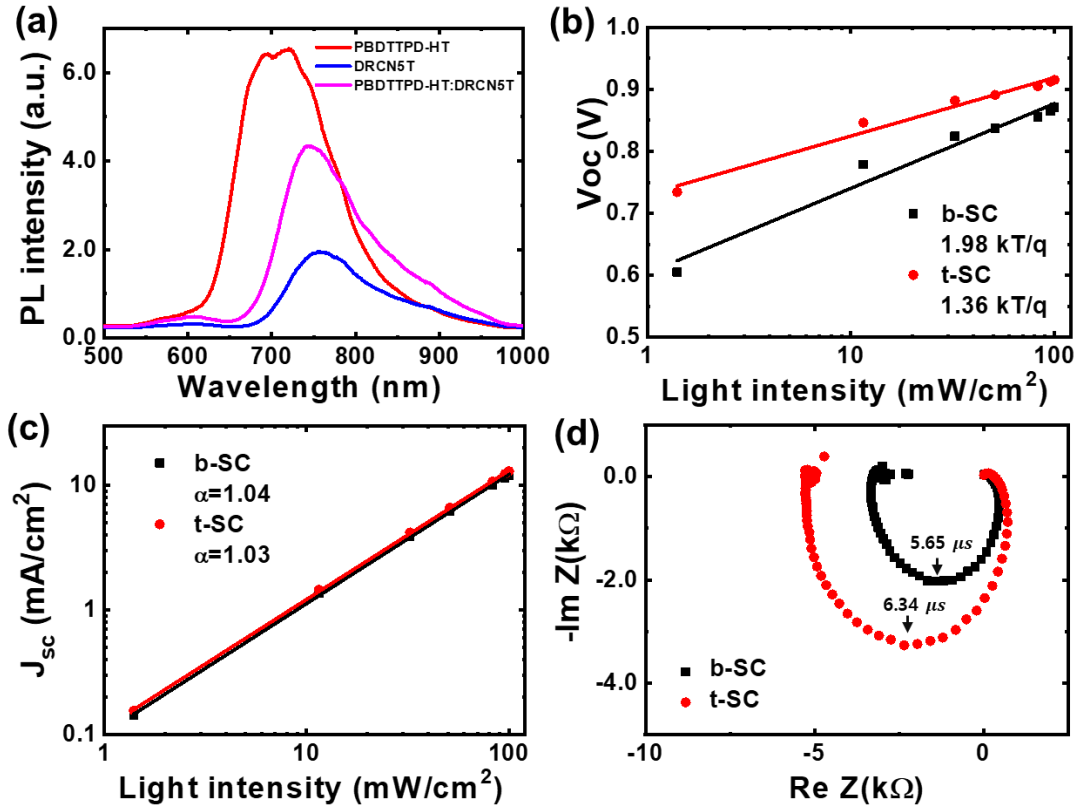

Figure 2.8. (a) PL spectra of PBDTTPD-TH film, DRCN5T film, and PBDTTPD-TH:DRCN5T mixed film. (b) V_{oc} versus light intensity for b-SC and t-SC. (c) J_{sc} versus light intensity for b-SC and t-SC. (d) Intensity-modulated photovoltage spectrographs of b-SC and t-SC.

In general, if the charge separation occurs through the CT state, there is a possibility for first-order recombination to occur (i.e., decay from the CT state to the ground state). If the electron moved to DRCN5T directly without going through the CT state created between PBDTTPD-HT and $PC_{71}BM$, this first-order recombination would be suppressed. To verify this suppression, we examined the light intensity (I) dependence for both J_{sc} and V_{oc}. **Figure 2.8b** shows V_{oc} versus light intensity for b-SC and t-SC. The data were fitted to the linear law

$$V_{OC} \propto n\left(\frac{kT}{q}\right) lnI \qquad \text{Equation (2.2)}$$

where k is the Boltzmann constant and T is the absolute temperature.[85-88] The extracted slope value

was 1.98 for b-SC. In the case of t-SC, a much smaller slope value of 1.36 was observed, indicating that first-order recombination was indeed suppressed in t-SC, which contained DRCN5T. The relationship between J_{sc} and light intensity followed the power law $J_{sc} \propto I^{\alpha}$ (**Figure 2.8c**). In general, bimolecular recombination becomes negligible under short-circuit conditions as α approaches 1.0 (weak bimolecular recombination).[85-88] The fitted α values were 1.04 for b-SC and 1.03 for t-SC, both close to 1, indicating that both b-SC and t-SC were nearly free from bimolecular recombination loss. Intensity-modulated photovoltage spectroscopy (IMVS) carried out under open-circuit conditions showed a consistent result (**Figure 2.8d**). IMVS provides information about the carrier lifetime and electron–hole recombination dynamics under open-circuit conditions.[89] The recombination times calculated using the frequency minimum were longer for t-SC (6.34 μs) than for b-SC (5.65 μs). This result coincided with the light intensity dependence of V_{oc}. We interpret this to be a result of reduced first-order recombination probability because of cascading transfer through DRCN5T.

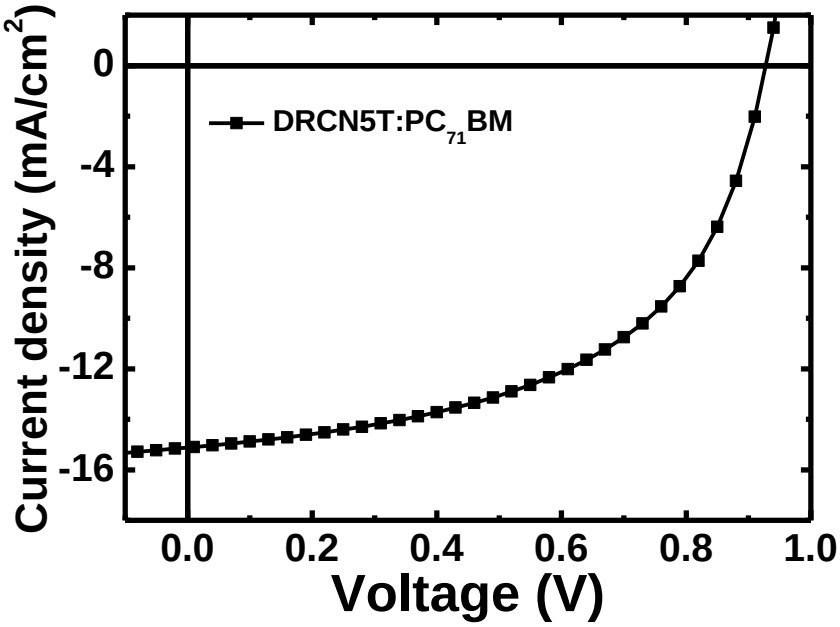

Figure 2.9. J–V characteristics of DRCN5T:PC_{71}BM OSC.

To investigate the trap density change directly, the frequency-dependent capacitance was measured for b-SC and t-SC as shown in **Figure 2.10a**. In the high-frequency region, the level of the high frequency plateau corresponding to the shallow traps was almost the same for b-SC and t-SC, which indicated that the density of shallow traps was not changed by incorporating DRCN5T. In the low frequency region, t-SC exhibited lower capacitance than b-SC, demonstrating a lower density of deep trap states. The trap level with respect to the valence band maximum (E_ω) is related to angular frequency (ω) as follows:

$$E_\omega = k_B T \ln(\frac{\omega_0}{\omega}) \qquad \text{Equation (2.3)}$$

where the ω_0 is the attempt-to-escape frequency; in general, ω_0 is assumed to be ~10^{11} s^{-1}.[90] Using the applied ω, the trap density was extracted from the derivative of the capacitance using the relation

$$N_t = -\frac{V_{bi}}{qW}\frac{dC}{d\omega}\frac{\omega}{k_B T} \qquad \text{Equation (2.4)}$$

where V_{bi} is the built-in potential and W is the depletion width.[90] A comparison of distributions of trap density extracted from the low frequency regions of **Figure 2.10a** for shows that the trap density of t-SC was clearly lower than that of b-SC (**Figure 2.10b**). In particular, the abnormal trap density observed around the 0.3 eV level for in b-SC was nearly absent for t-SC.

To give more solid experimental evidence of the elimination of charge transfer energy loss by incorporating DRCN5T, we tried to measure E_{loss} directly using EQE and EL spectra of t-SC and b-SC as shown in **Figure 2.10c and 2.10d**. The E_{loss} in PSC is generally analyzed in terms of two energy losses: charge transport energy loss and recombination energy loss ($E_{loss} = \Delta E_{CT} + \Delta E_{rec}$). ΔE_{CT} occurs during charge generation as $\Delta E_{CT} = E_g - E_{CT}$, where E_g is the optical gap of the device and E_{CT} is the energy level of CT state. ΔE_{rec} is generated during the charge recombination process as $\Delta E_{rec} = E_{CT} - qV_{oc}$.[91-93] E_{CT} can be extracted from the intersection of the EQE and EL spectra.[15, 94, 95] The extracted E_{CT} values of b-SC and t-SC were 1.76 and 1.81 eV, respectively. E_g values for t-SC and b-SC were extracted from absorption measurements (see **Figure 2.11**). Although t-SC showed weak absorption caused by DRCN5T below the edge of the main absorption, it was not reflected in the extracted E_g because the oscillation strength was very weak. The extracted ΔE_{CT} values were 0.11 eV for b-SC and 0.01 eV for t-SC. The charge transfer energy loss in t-SC was almost negligible. The calculated ΔE_{rec} values were almost same, with 0.89 eV for b-SC and 0.88 eV for t-SC. This result was consistent with the that obtained from the trend of J_{sc} versus light intensity. Finally, the calculated E_{loss} for b-SC was

1.0 eV, but t-SC showed a lesser E_{loss} of 0.89 eV. The energy loss of t-SC was mostly recombination energy loss. Such reduced E_{loss} was attributed to the elimination of ΔE_{CT} by means of the cascading charge transfer process.

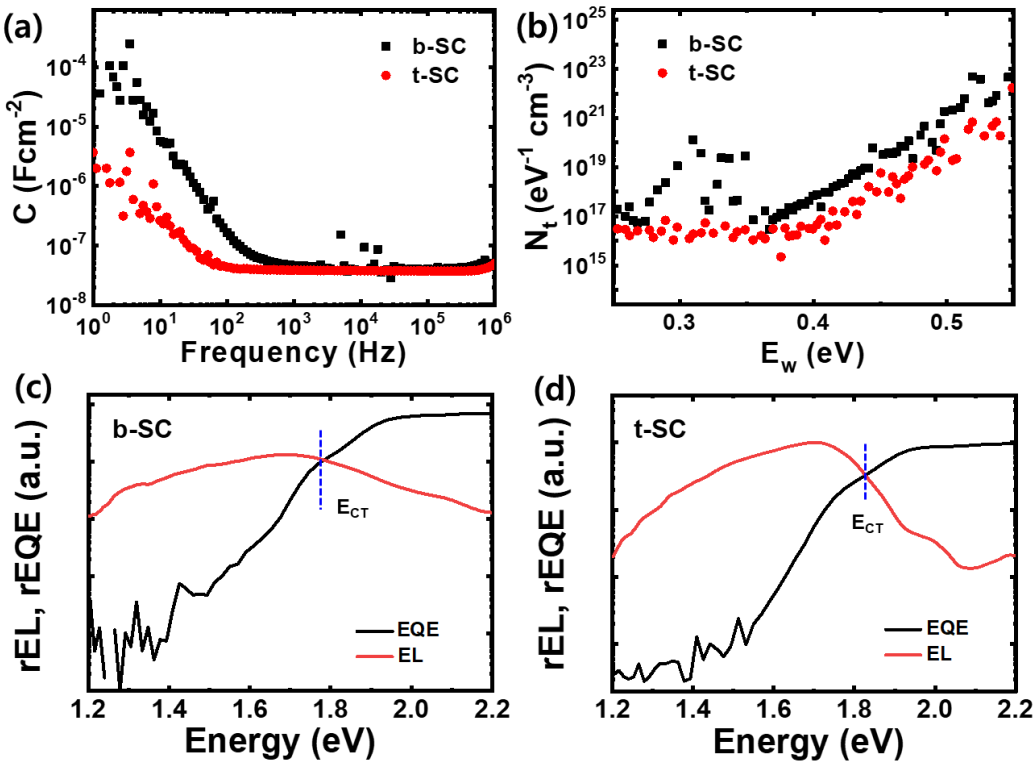

Figure 2.10. (a) Trap density versus trap energy level of b-SC and t-SC. (b) Distributions of trap density extracted from the low frequency region. (c) EQE and electroluminescence (EL) of b-SC. (d) EQE and electroluminescence (EL) of t-SC.

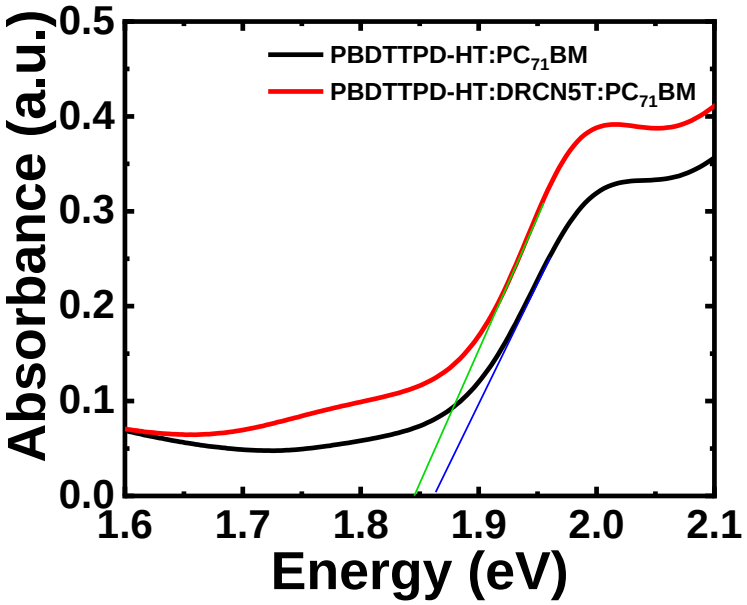

Figure 2.11. Absorbance of PBDTTPD-HT:$PC_{71}BM$ and PBDTTPD-HT:DRCN5T:$PC_{71}BM$ films.

Another weak point of fullerene-based solar cells is relatively poor long-term stability because of aggregation tendency of fullerene derivatives. **Figure 2.12** shows the PCE stability for the binary solar cell and ternary solar cell. The stability data obtained from PM6:Y6 non-fullerene solar cell was presented together to comparison. General J-V characteristics of PM6:Y6 non-fullerene solar cell is presented in Supporting Information (**Figure 2.13**). In the stability test conducted with the devices stored in N_2-filled glove box under dark condition, the binary and ternary solar cell exhibited similar stability. Although PM6:Y6 non-fullerene solar cell showed significantly higher PCE, the stability was still very poor than that of fullerene-based sola cell. The stability test conducted with devices stored in air under continuous illumination condition showed the stability of ternary devices slightly better than that of binary solar cell. In AFM study to investigate the morphology change (**Figure 2.14**) for the as-prepared fresh active layer and aged active layer, surface morphology of aged active layer showed slightly aggregated morphology with increased RMS roughness. However, no discernible change was observed in ternary active layer. Therefore, we concluded that that slightly better stability of ternary solar cell was because the added DRCN5T played a role in retarding the aggregation of $PC_{71}BM$.

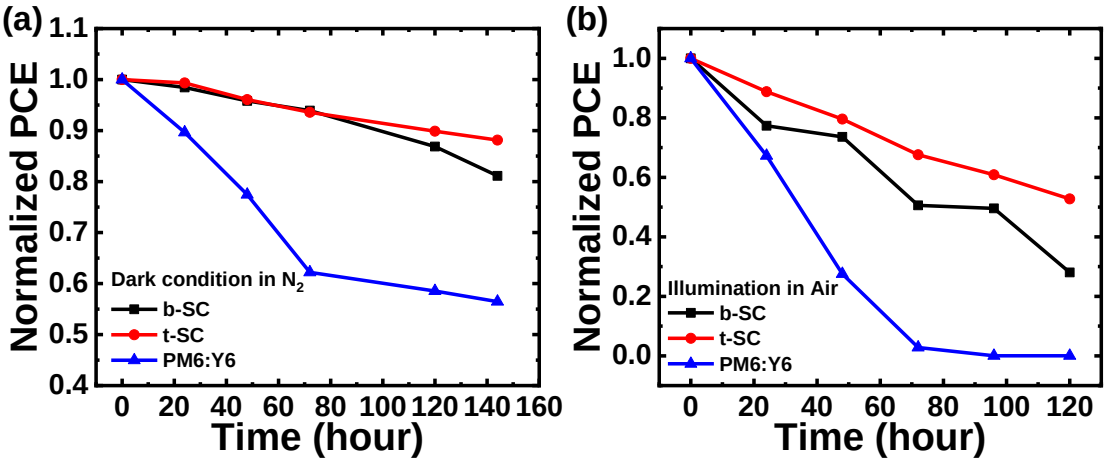

Figure 2.12. (a) PCE stability of b-SC and t-SC stored in N_2-filled glove box under dark condition, (b) PCE stability of b-SC and t-SC stored in air under continuous illumination.

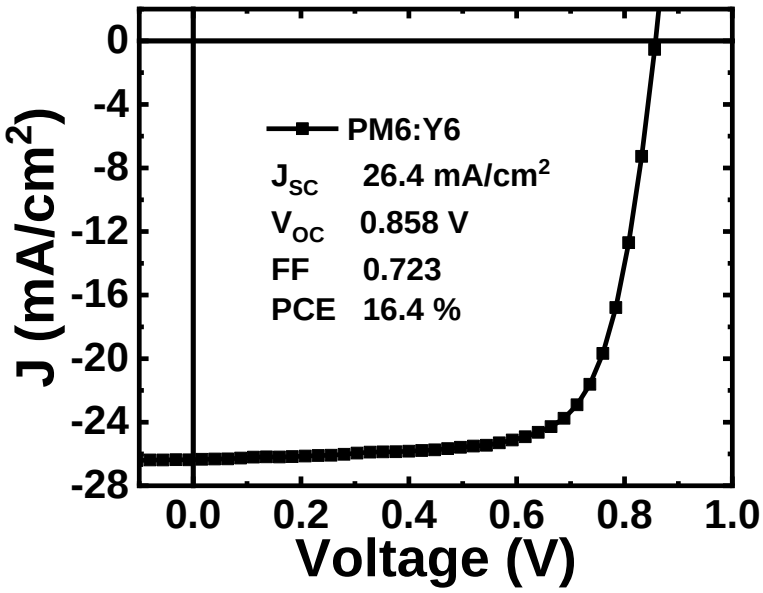

Figure 2.13. J–V characteristics of PM6:Y6 non-fullerene solar cell.

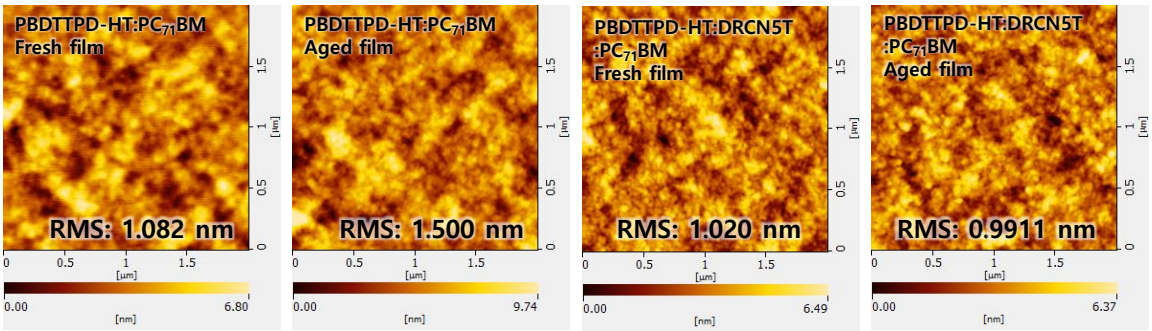

Figure 2.14. AFM images for the as-prepared fresh active layer and aged active layer.

2.4 Conclusion

To reduce the charge transfer energy loss in fullerene-based BHJ solar cells, we introduced a ternary structuring strategy by which a small-molecule secondary donor is added. A ternary system based on the wide-band-gap polymer PBDTTPD-HT, small molecule DRCN5T, and $PC_{71}BM$ showed cascading charge transfer from PBDTTPD-HT through DRCN5T to $PC_{71}BM$, thus allowing transfer of electrons without going through the deep CT state created between PBDTTPD-HT and $PC_{71}BM$. Low energy loss between DRCN5T and $PC_{71}BM$occurred because the high E_{CT} level of $PC_{71}BM$ was close to the singlet state energy of DRCN5T, significantly reducing the probability of first-order recombination. Consequently, the addition of a small amount of DRCN5T as a secondary donor into the PBDTTPD-HT:$PC_{71}BM$ system enhanced the PCE, which was mostly attributed to improved V_{oc} by means of eliminated charge transfer energy loss. The present work clearly showed that using this donor–donor–acceptor ternary configuration could be a way to avoid the high energy loss problem of fullerene acceptors. In order to achieve this effect, the selection of suitable secondary donor materials is very important. The second donor material must be selected as a material that can induce cascading charge transport and it must have a high E_{CT} level, which is close to the energy of the singlet state of secondary donor materials.

Chapter 3. Solid-Solvent Hybrid Additive for the Simultaneous Control of the Macro- and Micro- Morphology in Non-Fullerene-Based Organic Solar Cells

3.1 Research background

As a promising solar energy-harvesting technology, organic solar cells (OSCs) have advantages of being light-weight, facile to process, flexible, and potentially inexpensive along with a large-area fabrication capability.[96-98] In the past few decades, efforts made in organic material design and process optimization such as the bulk heterojunction (BHJ) and mechanism of charge transfer have contributed significantly to increase the power conversion efficiency (PCE). Recently, a high PCE was achieved in a binary blend system due to the development of non-fullerene acceptors (NFA) with a low bandgap.[99-101] In particular, Zou's group reported a Y6 acceptor with a high electron mobility and a wide absorption range of up to 930 nm, which achieved an efficiency exceeding 16% PCE with a single-junction photoactive layer.[102] Thus far, devices based on Y6 or its derivatives as electron acceptors have displayed the highest PCEs among binary OSCs.[103-105]

Currently, most BHJ OSCs are fabricated with the assistance of high boiling point solvent additives to optimize the phase separation and domain size of the active layer. Particularly, in PM6:Y6 solar cells, the use of a co-soluble solvent additive such as 1-chloronaphthalene (1-CN) is mandatory due to the inherent strong self-aggregation tendency of PM6 and Y6. The self-aggregation tendency of active materials helps to increase crystallinity within the phase, but too large grain formation reduces the donor-acceptor (D/A) interface regions needed for exciton dissociation, leading to exciton recombination caused by the short exciton diffusion length.[106, 107] The large phase separation is mainly due to the insufficient compatibility of the D/A materials. The BHJ morphology with compatibility, domain size, and microstructure has a significant impact on the charge transport efficiency and device performance.[108-110]

In general, macroscopic phase separation can be controlled using a high boiling point solvent based

on the selective solubility and low volatility. However, the control of the microscopic morphology of the inside phase is mainly dependent on the interaction energy and self-assembly characteristics of each donor and acceptor.[111] Enhancing the intermolecular microscopic π-π stacking morphology of the inside phase is crucial to the facilitation of both exciton diffusion before charge separation and charge transport after charge separation. Although the solvent additive process adjusts the macroscopic morphology through selective phase separation, it has limitations in simultaneously optimizing the microscopic morphology (e.g., π-π stacking, orientation). Therefore, additional agents that can further control the microscopic π-π stacking morphology are required to overcome these limitations. Recently, there were some reports which demonstrated that the introduction of solid additives can enhance the intermolecular π–π stacking of the non-fullerene acceptor and thus, facilitate the charge transport properties in the active layers.[111, 112] However, since conventional solid additives are typically insulating, they have the potential to prevent charge transport by acting as a charge trap-site.[113-115] In addition, linear (1D) solid additives are prone to agglomeration and poor dispersion properties, resulting in a lower efficiency compared to three-dimensional (3D) materials.[116, 117]

In the present work, we introduced a hybrid additive method on PM6:Y6 solar cells using both a solvent additive and a solid additive at the same time (**Figure 3.1**). For the solvent additive, the well-known 1-CN solvent additive, which is generally utilized in PM6:Y6 solar cells, was used to optimize the macroscopic donor-acceptor phase separation morphology.[118] Note that since the PM6:Y6 blend normally shows a strong self-aggregation tendency, the role of the solvent additive is to prevent excessive phase separation.[106] Thus, a co-soluble 1-CN additive that can dissolve both the PM6 donor polymer and Y6 acceptor is commonly applied. For the solid additive, newly synthesized star-shaped solid additives (Star-A and Star-F) were used to further optimize the microscopic π-π stacking morphology. The structures of Star-A and Star-F were designed as A-D-A, where an electron accepting unit (A) is connected in series with an electron donating unit (D), which is beneficial for an efficient intramolecular push-pull electronic structure.[119, 120] Recently, a high OSC performance was reported using indacenodithiophene (IDT), Y6-series (Y-series), and naphthalenediimide (NDI) as central cores to enhance the π-π stacking, leading to facilitated charge transfer. However, highly coplanar fused ring cores induce excessive self-aggregation.[121-124] Meanwhile, a highly distorted 3D central core (e.g., spirobifluorene, tetraphenylethylene) was also developed to inhibit strong self-aggregation.[125] The distorted core structure improves the dispersion property of the additives in the BHJ morphology, thereby effectively optimizing the morphology with only a small amount of additive. Therefore, the ideal solid semiconductor additives simultaneously require a suitable balance of coplanarity and distortion characteristics. 10,15-Dihydro-5H-diindeno[1,2-a;1',2'-c]fluorene (truxene) is easy to synthesize and has high π-conjugation characteristics by sharing fluorene, which is advantageous for π-

π stacking.[126, 127] The truxene with a 3D star-shaped structure facilitates the control of self-aggregation compared to linear molecules. This feature suggests that truxene can be a promising building block for solid semiconductor additives. In addition, an extended π linker and two terminal group types were introduced to modulate electrical properties, in accordance to active material results of density functional theory (DFT) calculations at the B3LYP/6-31G (d,p) level.

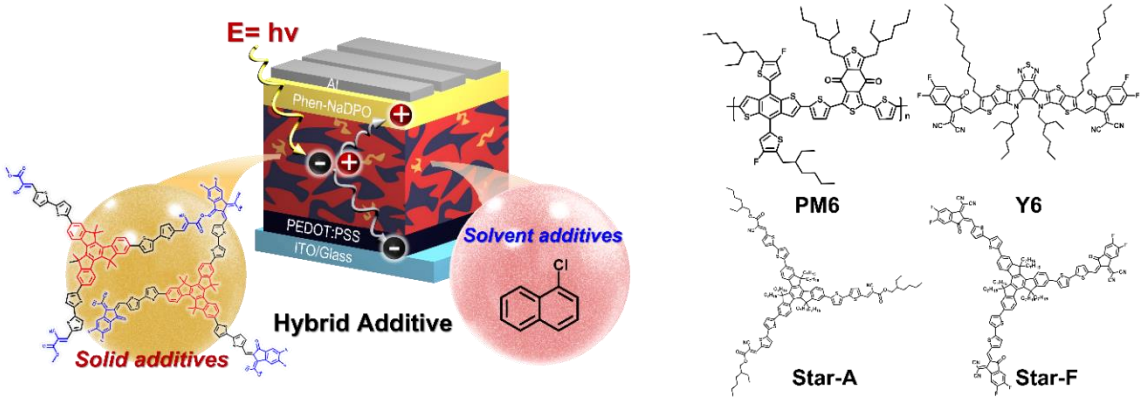

Figure 3.1. Schematic of the operating OSC devices with solid additives (Star-A and Star-F) and solvent additive (1-CN). Molecular structures of the polymer donor PM6, non-fullerene acceptor Y6, and star-shaped solid additives (Star-A and Star-F).

Unlike conventional solid additives, the star-series additives exhibit a semiconducting property for charge transport (e.g., intra- and intermolecular charge transport). In particular, DFT calculations of the electrostatic potential (ESP) reveal that electrostatically negative and positive potential regions coexist. The locally different ESPs contribute to compatibility between the donor and acceptor.[128] In addition, the star-shaped 3D structure suppresses excessive phase separation of PM6 and Y6 together with the co-soluble solvent additive 1-CN. We experimentally verified that these star solid additives can prevent the strong self-phase separation of the PM6:Y6 BHJ blend and improve compatibility through microstructure analysis including atomic force microscopy (AFM), grazing-incidence small-angle X-ray scattering (GISAXS), and Flory–Huggins parameter calculations. Further, grazing incidence wide-angle X-ray scattering (GIWAXS) measurements showed that the star additives induced dense and strong intermolecular π-π stacking and face-on dominant orientation in the microscopic morphology.

Consequently, we achieved further enhancement of photovoltaic performance with only 1% addition of the star-shaped solid additives.

3.2 Experiment

Synthesis procedures and characterization:

Synthesis of **compound 1**: 1-indanone (5 g, 23.8 mmol) was added to a mixed solution of acetic acid (60 mL) and concentrated hydrochloric acid (30 mL). Then the solution was heated to 100 °C for 24 h. After cooling to room temperature, the mixture was poured into 800 ml of ice water, and stirred for 1 h. The yellow precipitate was filtered, and washed with water, ethanol, cold acetone and cold dichloromethane. Compound 1 was obtained as light yellow solid (9.2 g, 63.9%). ^{1}H NMR (500 MHz, CDCl3, δ): 7.96 (d, J = 7.7 Hz, 3H), 7.70 (d, J = 7.4 Hz, 3H), 7.50 (d, J = 7.5 Hz, 3H), 7.41 (d, J = 7.3 Hz, 3H), 4.28 (d, *J* = 4.6 Hz, 6H).

Synthesis of **compound 2**: Compound 1 (5.0 g, 14.6 mmol) was dissolved in 120 mL dry THF under N_2 atmosphere. After cooling to -78 °C, n-BuLi (73 mL, 146.02 mmol, 2.4 M in n-hexane) was added dropwise and the mixture was stirred at -78 °C for 5 h. A solution of $C_7H_{15}Br$ (31.54 g, 17518.22 mmol) in 50 mL THF was injected slowly. The mixture was slowly warmed to room temperature and stirred overnight. Then the solution was quenched with saturated ammonium chloride solution (150 mL), extracted with ethyl acetate, dried over MgSO4. After the organic phase was concentrated under reduced pressure, the crude product was purified by column chromatography on silica gel using petroleum ether as the eluent. Compound 2 was obtained as off-green solid (9.78 g, 72.1%). ^{1}H NMR (600 MHz, Chloroform-*d*) δ 8.36 (d, 3H), 7.46 (d, *J* = 7.2 Hz, 3H), 7.38 (p, *J* = 7.2 Hz, 6H3.04 – 2.89 (m, 6H), 2.16 – 2.00 (m, 6H), 0.98 – 0.77 (m, 40H), 0.59 (t, J = 7.1 Hz, 18H), 0.48 (m, 12H). ^{13}C NMR (151 MHz, Chloroform-*d*) δ 153.65, 144.85, 144.83, 140.35, 138.38, 126.32, 125.94, 124.65, 124.63, 122.17, 55.62, 36.97, 31.49, 29.67, 29.49, 29.37, 23.89, 22.27, 22.21, 14.11, 13.86, 13.84.

Synthesis of **compound 3**: A compound 2 (8.72 g, 9.37 mmol) was dissolved into DCM (40 mL) was carefully degassed before bromine was added. A bromine (5.17 g, 32.79 mmol) was added dropwise under ice bath. The mixture was gradually warmed to room temperature and stirred for 48 h. After quenching with saturated $NaHSO_3$ aqueous solution, the mixture was extracted with chloroform for three times, and the organic phase was dried over MgSO4. After the solvent was removed, the crude product was purified by column chromatography on silica gel (silica gel; eluent: hexane:DCM= 7:3) Compound 3 was obtained as pale yellow solid (8.1g, 74.3%) ^{1}H NMR (600 MHz, Chloroform-d) δ 8.17 (d, J = 8.4 Hz, 3H), 7.56 (d, J = 2.0 Hz, 3H), 7.51 (dd, J = 8.4, 2.0 Hz, 3H), 2.83 (m, 6H), 2.01 (m,

6H), 1.26-0.98(m, 40H), 0.55 (t, J= 7.2 Hz, 18H), 0.51 – 0.41 (m, 12H), ^{13}C NMR (151 MHz, Chloroform-d) δ 155.90, 144.94, 138.88, 137.64, 129.39, 125.92, 125.55, 121.07, 55.98, 36.75, 31.47, 29.71, 29.62, 28.84, 23.89, 22.48, 14.12, 13.88, 13.85.

Synthesis of **compound 4**: A mixture of compound 3 (3.0 g, 3.22 mmol), bis(pinacolato)diboron (4.91 g, 19.34 mmol), AcOK (2.46 g, 24.51 mmol), and DMF (90 mL) was carefully degassed before $Pd(dppf)_2Cl_2$ (150 mg, 0.246 mmol) was added. The mixture was stirred for 48 h at 90 °C under N_2. After the solution was cooled to room temperature, water (150 mL) and CH_2Cl_2 (150 mL) were added. The organic layer was separated and washed with water for three times. After removal of the organic solvent, the crude product was purified by column chromatography (silica gel; eluent: petroleum ether:ethyl acetate = 2:1) to afford compound 4 (2.57 g, yield: 60.9%) as a light yellow solid. ^{1}H NMR (400 MHz, Chloroform-*d*) δ 8.54 (d, *J* = 2.1 Hz, 3H), 8.16 (d, *J* = 2.1 Hz, 3H), 7.62 (d, J = 5.2 Hz, 3H) 2.77 – 2.75 (m, 6H), 2.02 (m, 6H), 1.26-0.89 (m, 52H), 0.55 (t, J= 7.2 Hz, 18H), 0.51 – 0.41 (m, 12H), ^{13}C NMR (151 MHz, Chloroform-*d*) δ 155.86, 145.98, 145.67, 145.29, 140.67, 138.36, 136.74, 129.61, 129.52, 129.48, 129.26, 129.21, 129.16, 127.29, 127.26, 125.96, 125.89, 125.84, 125.66, 125.62, 125.60, 123.10, 56.06, 55.99, 55.97, 55.89, 36.77, 36.72, 36.69, 36.66, 36.62, 31.47, 29.59, 29.58, 29.55, 29.53, 29.51, 28.82, 28.81, 28.79, 26.33, 23.93, 23.92, 23.87, 22.65, 22.50, 22.47, 13.88, 13.85, 13.68.

Synthesis of **compound 5**: 5'-bromo-[2,2'-bithiophene]-5-carbaldehyde (0.77 g, 2.82 mmol), compound 4 (0.62 g, 0.47 mmol), $Pd(PPh_3)_4$ (0.11g, 0.096 mmol) and K_2CO_3 (4.98g, 36.03 mmol) were dissolved in Toluene (20 mL) and the reaction mixture was heated at 120 °C overnight under Ar. After the reaction mixture was cooled to room temperature, the solution was quenched with water and extracted with CH_2Cl_2. The combined organic layer was washed with brine for several times, and then dried over anhydrous MgSO4. After the solvent was removed off under reduced pressure, the crude product was purified by column chromatography (silica gel; eluent: petroleum ether: diethyl ether = 8:2) to afford compound 5 (0.51 g, yield: 72.1%) as an orange solid. ^{1}H NMR (600 MHz, Chloroform-*d*) δ 9.81 (d, *J* = 16.9 Hz, 3H), 8.33 (d, *J* = 8.2 Hz, 3H), 7.67 (m, 6H), 7.35 (q, *J* = 3.7 Hz, 3H), 7.33 (m, 3H), 7.31 (m, *J* = 3.9 Hz, 3H), 7.26 (m, *J* = 3.2 Hz, 3H), 2.90 (d, *J* = 5.1 Hz, 6H), 2.08 (d, *J* = 5.0 Hz, 6H), 0.99 – 0.72 (m, 40H), 0.58 -0.51 (m, 18H), 0.55 – 0.45 (m, `12H). ^{13}C NMR (151 MHz, $CDCl_3$) δ 182.47, 182.43, 154.59, 147.30, 146.66, 145.82, 145.65, 142.07, 141.58, 140.43, 137.96, 137.41, 137.26, 137.13, 135.17, 135.13, 135.10, 135.06, 134.91, 132.14, 132.08, 131.94, 131.75, 131.20, 130.51, 130.45, 130.37, 128.54, 128.46, 128.37, 128.06, 128.01, 127.97, 127.93, 127.87, 127.25, 127.09, 126.20, 125.10, 124.39, 124.26, 124.20, 124.13, 123.97, 119.28, 114.17, 77.22, 77.01, 76.80, 55.89, 37.00, 31.47, 31.41, 29.70, 28.85, 24.87, 23.98, 22.76, 22.48, 13.87, 13.84, 13.74. HRMS: Calcd for $[C_{96}H_{114}O_3S_6 + H]^+$, m/z = 1509.2642. Found: m/z = 1508.2444 $[M+H]^+$.

Synthesis of **Star-A**: compound 5 (0.58 g, 0.38 mmol) and 2-ethylhexyl cyanoacetate (0.46 g, 2.31 mmol) were first dissolved in $CHCl_3$ (10 mL). TEA (six drops) was then added and the reaction mixture was stirred at room temperature overnight. After the reaction mixture was quenched with water and extracted with CH_2Cl_2. and then dried over anhydrous MgSO4. After the solvent was removed off under reduced pressure, the crude product was purified by column chromatography (silica gel; eluent: hexane : diethyl ether = 8:2) to afford Star-A (0.35 g, yield: 47%) as a red solid. ^{1}H NMR (600 MHz, Chloroform-*d*) δ 8.43 (d, *J* = 8.3 Hz, 3H), 8.32 (s, 3H), 7.78 – 7.71 (m, 9H), 7.55 – 7.46 (m, 6H), 7.38 – 7.33 (m, 3H), 4.32 – 4.23 (m, 6H), 3.01 (d, *J* = 5.3 Hz, 6H), 2.19 (tt, *J* = 13.6, 11.2, 4.6 Hz, 6H), 1.76-1.33 (m, 29H), 1.05 -0.89 (m, 75H), 0.68 (t, *J* = 7.3 Hz, 6H), 0.60 (m, 36H), ^{13}C NMR (151 MHz, Chloroform-*d*) δ 163.23, 154.62, 147.64, 147.06, 146.12, 145.72, 140.52, 139.27, 137.96, 134.63, 134.19, 127.63, 125.12, 124.31, 124.15, 119.30, 116.03, 97.66, 68.84, 55.91, 38.82, 37.00, 31.48, 30.35, 29.71, 28.94, 28.87, 23.99, 23.79, 22.96, 22.49, 14.06, 13.89, 11.04. HRMS: Calcd for $[C_{122}H_{165}N_3O_6S_6 + H]^+$, m/z = 1945.8972 Found: m/z = 1944.8944 $[M+H]^+$.

Synthesis of **Star-F**: compound 5 (0.25 g, 0.19 mmol) and 2-(5,6-difluoro-3-oxo-2,3-dihydro-1H-inden-1-ylidene) malononitrile (0.53 g, 1.9 mmol) were first dissolved in $CHCl_3$ (60 mL). Piperidine (four drops) was then added and the reaction mixture was stirred at 85 °C overnight. After the reaction mixture was quenched with water and extracted with CH_2Cl_2. and then dried over anhydrous MgSO4. After the solvent was removed off under reduced pressure, the crude product was purified by precipitation methods in methanol solvent, it is purified through filtration. (0.21 g, yield: 52%) as a black solid. ^{1}H NMR (600 MHz, Chloroform-*d*) δ 8.28 (d, *J* = 8.1 Hz, 3H), 7.86 (m, 3H), 7.58 – 7.53 (m, 12H), 7.19 – 7.15 (m, 3H), 7.06 – 7.03 (m, 3H), 3.01 (s, 6H), 2.19 (s, 6H), 1.76-1.33 (m, 40H), 1.05 -0.89 (m, 18H), 0.68-0.60 (m, 12H), ^{13}C NMR (151 MHz, Chloroform-*d*) δ 208.23, 134.35, 130.87, 125.36, 124.94, 51.35, 49.59, 37.09, 32.77, 31.84, 31.45, 29.96, 29.60, 29.24, 28.78, 27.02, 26.06, 25.86, 22.56, 22.36, 19.64, 13.87, 13.68. HRMS: Calcd for $[C_{148}H_{120}F_6N_6O_3S_6 + H]^+$, m/z = 2374.3602 Found: m/z = 2373.5284 $[M+H]^+$.

1H, 13C NMR spectra were recorded on a Bruker BioSpin AG system operated at 600 MHz in deuterated chloroform solution at 298 K, unless specified otherwise. High resolution mass spectra (HRMS) were recorded on a JEOL JMS-700 mass spectrometer under electron impact (EI) or fast atom

bombardment (FAB) conditions in the Korea Basic Science Institute (Daegu, Korea). The elemental analyses were performed using a Carlo Erba Instruments CHNSO EA 1108 analyzer by the Korean Basic Science Institute. The UV-Vis analysis was performed with a Mecasys Optizen Pop UV/Vis spectrophotometer. For Photoluminescence (PL) spectroscopy analysis, thin films were excited at 630 nm or 480nm with a solid state laser in continuous wave operation (MGL-III-532, Changchun New Industries) at an excitation power of 80 mW. The laser beam was expanded to a spot size of 6 mm in diameter in order to probe a rather large sample volume. Photoluminescence was fiber-coupled into a spectrograph (Acton Research SpectraPro 300i) and detected with an intensified CCD (Princeton Research, PiMax 512). The thickness of all films is identical for accuracy of the PL quenching efficiency. Electrochemical cyclic voltammetry (PowerLab/AD instrument model system) were recorded in a computer controlled potentiostat conventional three electrode system in polymer thin films using a glassy carbon disk, platinumwire, and silver wire as a working electrode, counter electrode, and a quasi reference electrode, respectively, in acetonitrile (AN, HPLC grade) solution containing 0.1 M tetrabutylammonium hexafluorophosphate (Bu4NPF6) at a scan rate of 50 mV/s. Ferrocene is used as internal standard to calculate frontier orbital energy levels of polymers.

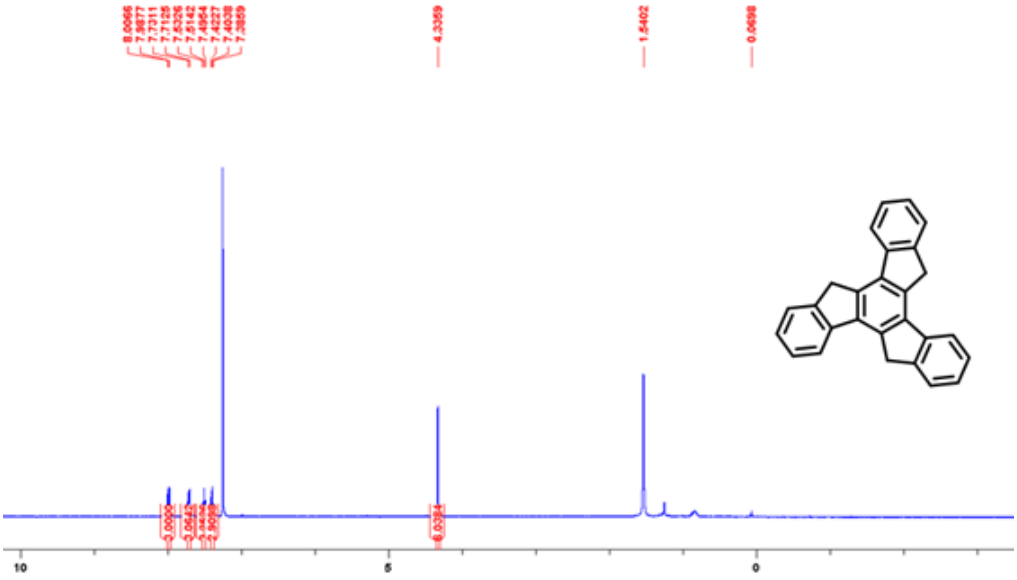

^{1}H NMR of compound 1

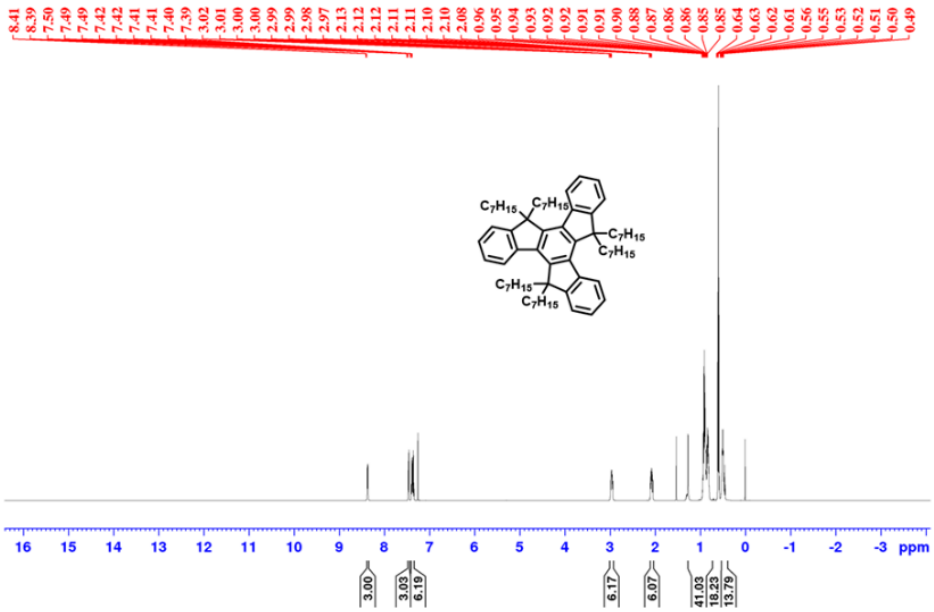

^{1}H NMR of compound 2

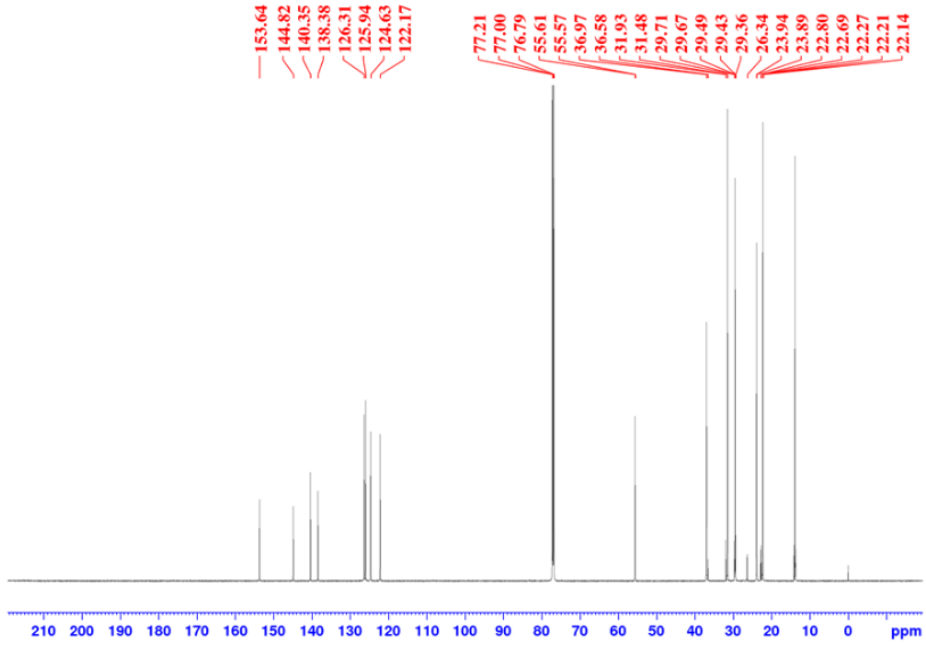

^{13}C NMR of compound 2

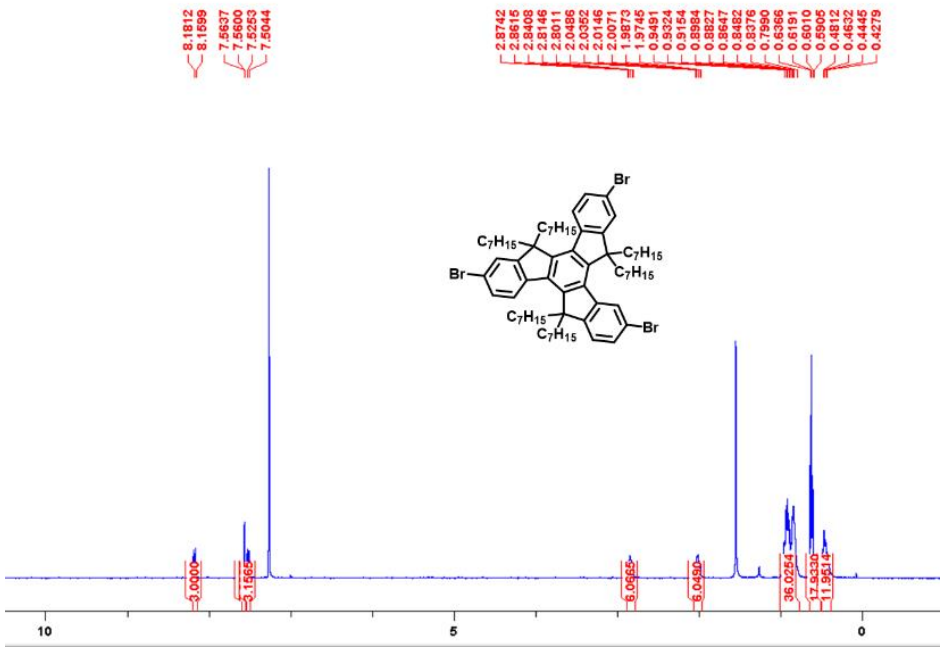

^{1}H NMR of compound 3

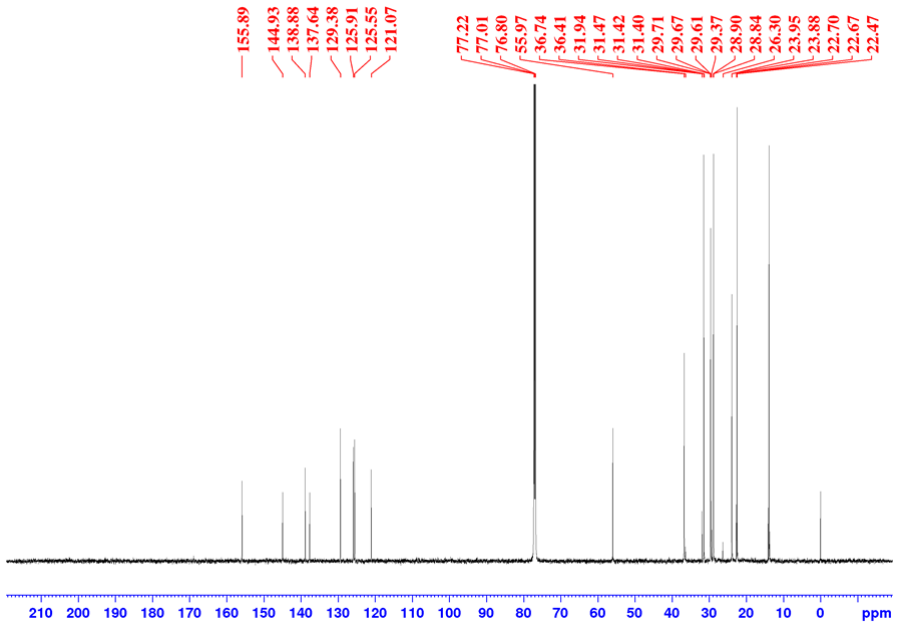

^{13}C NMR of compound 3

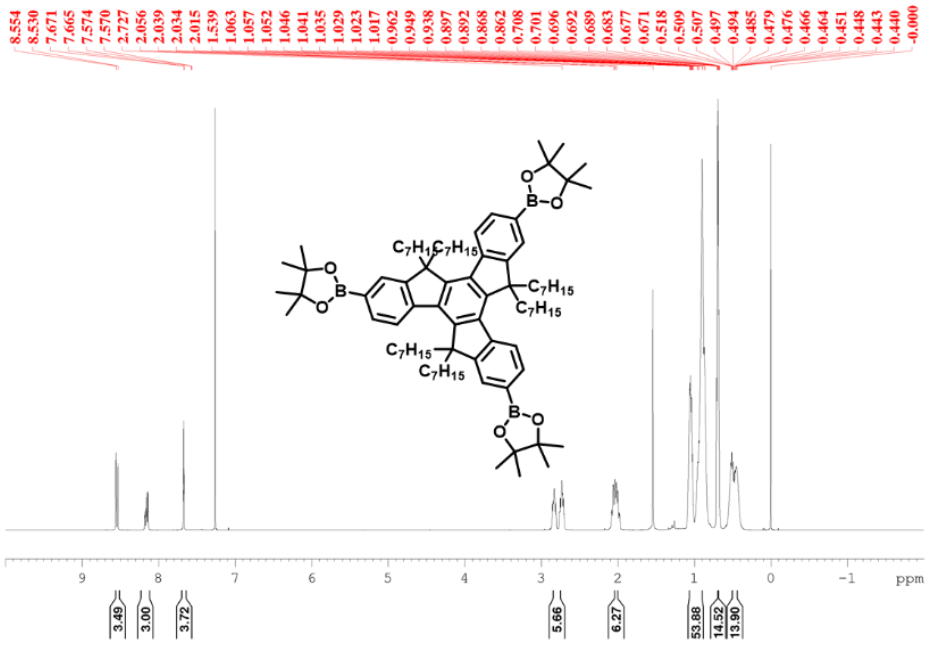

^{1}H NMR of compound 4

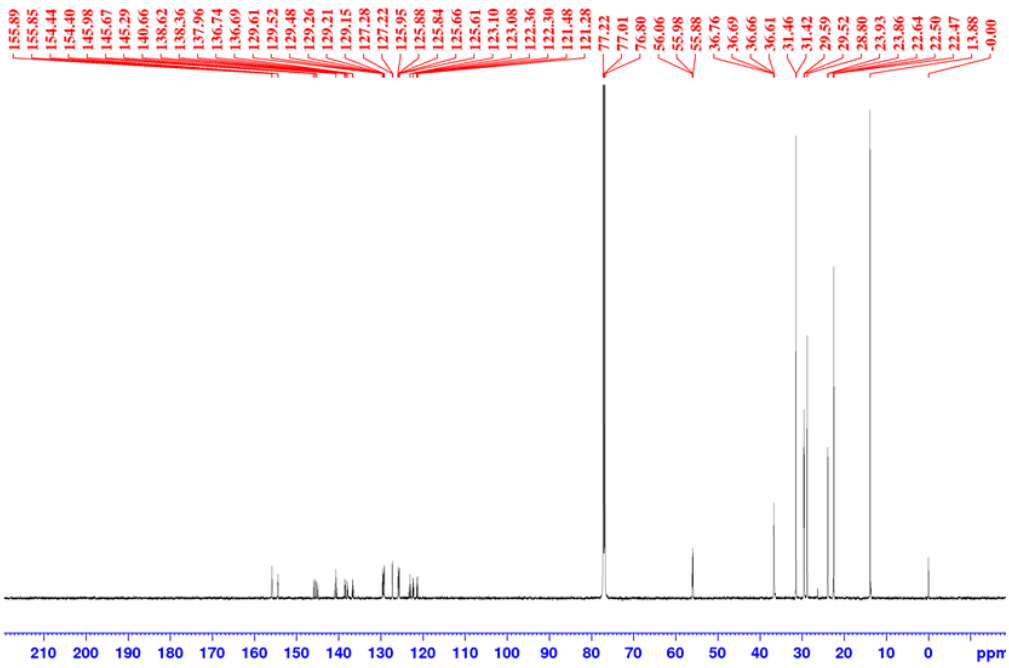

^{13}C NMR of compound 4

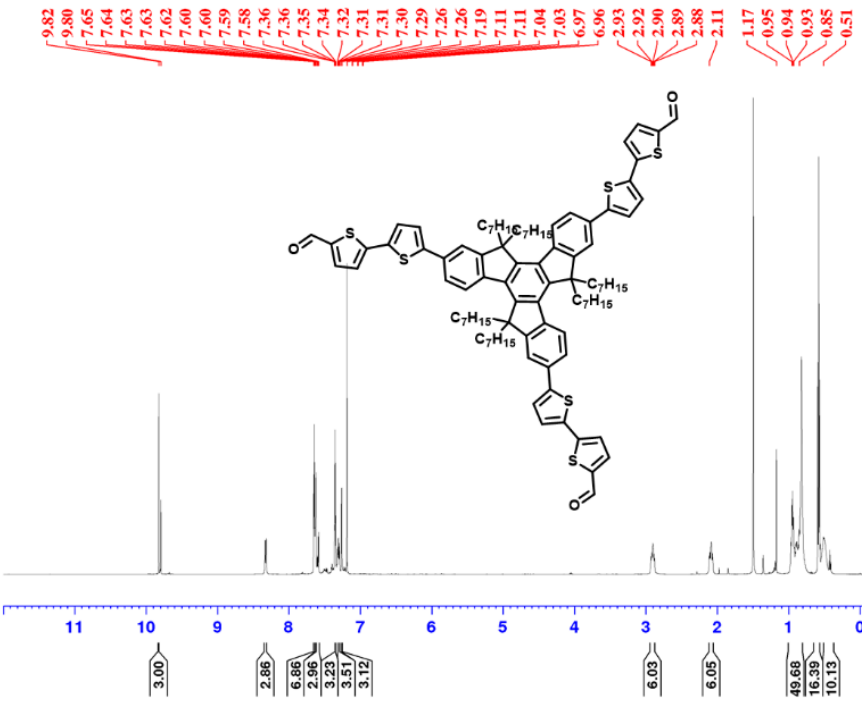

^{1}H NMR of compound 5

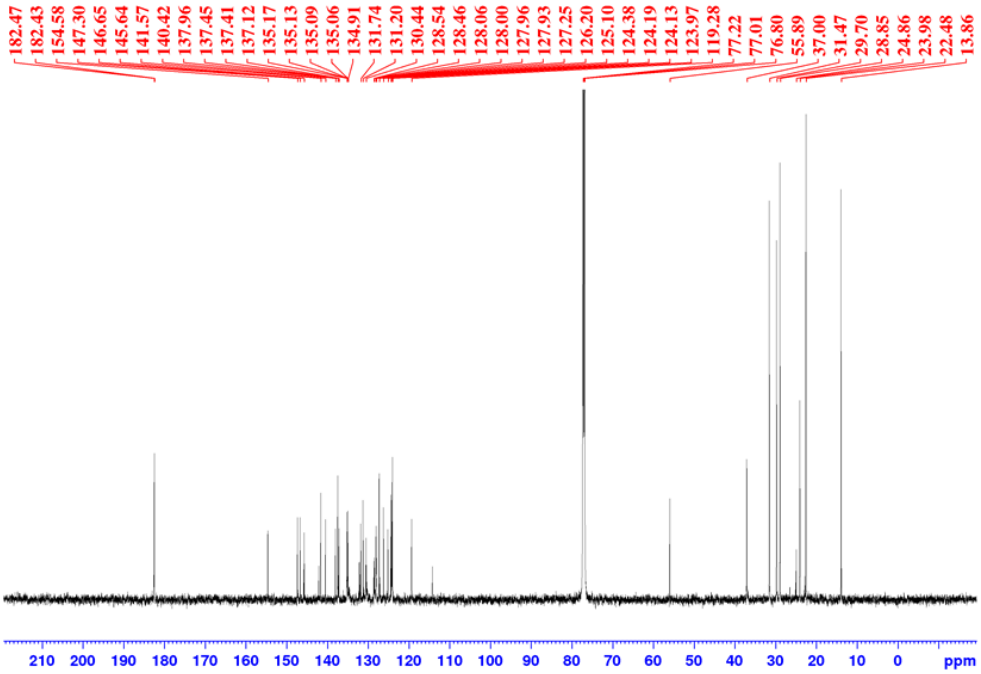

^{13}C NMR of compound 5

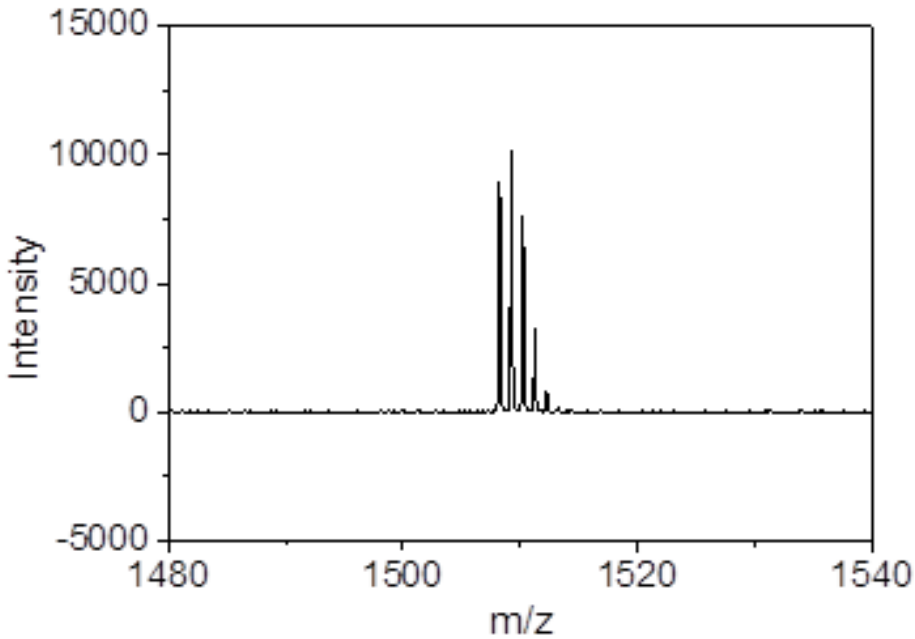

MALDI-TOF of compound 5

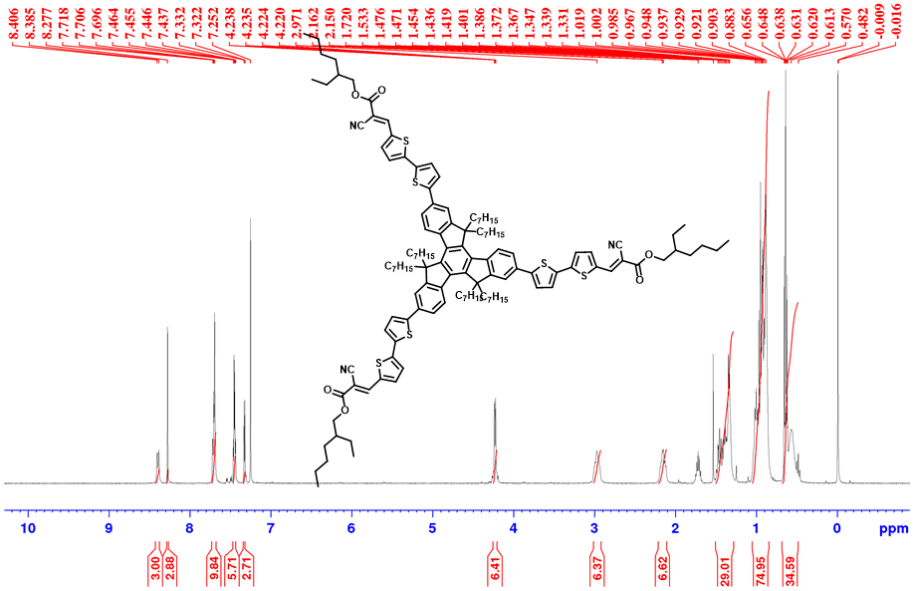

^{1}H NMR of Star-A

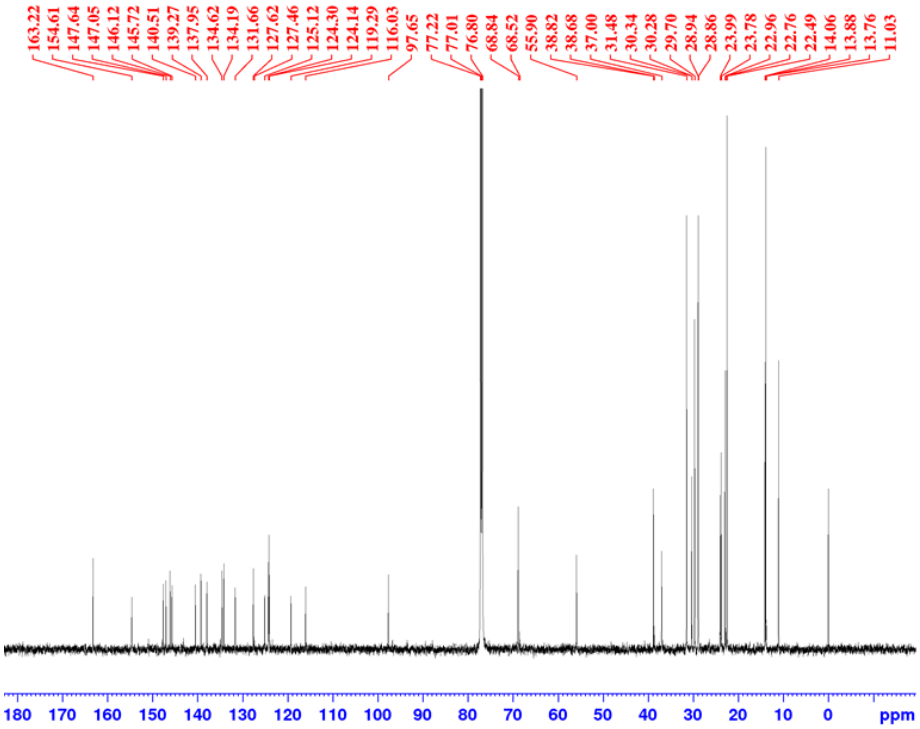

^{13}C NMR of Star-A

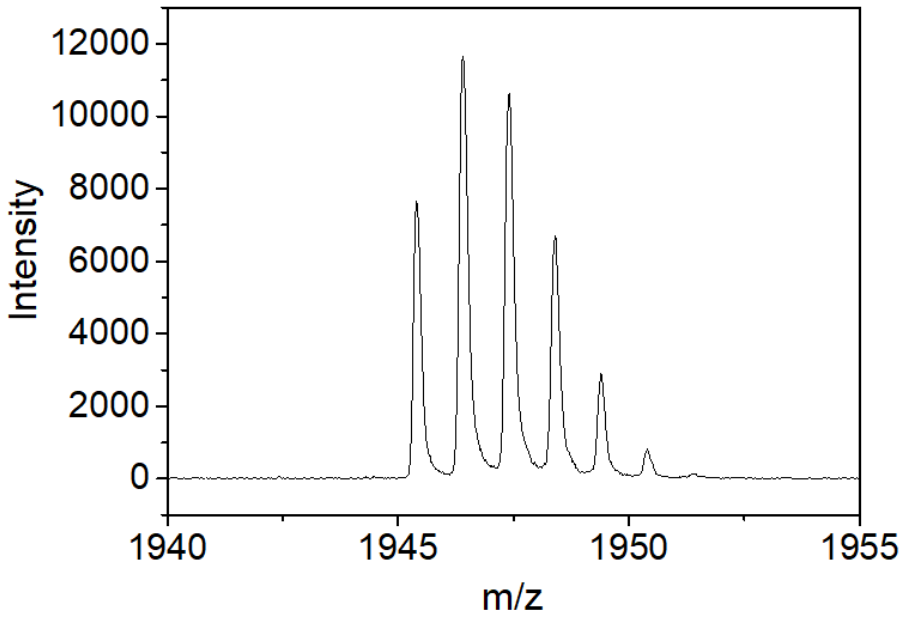

MALDI-TOF of Star-A

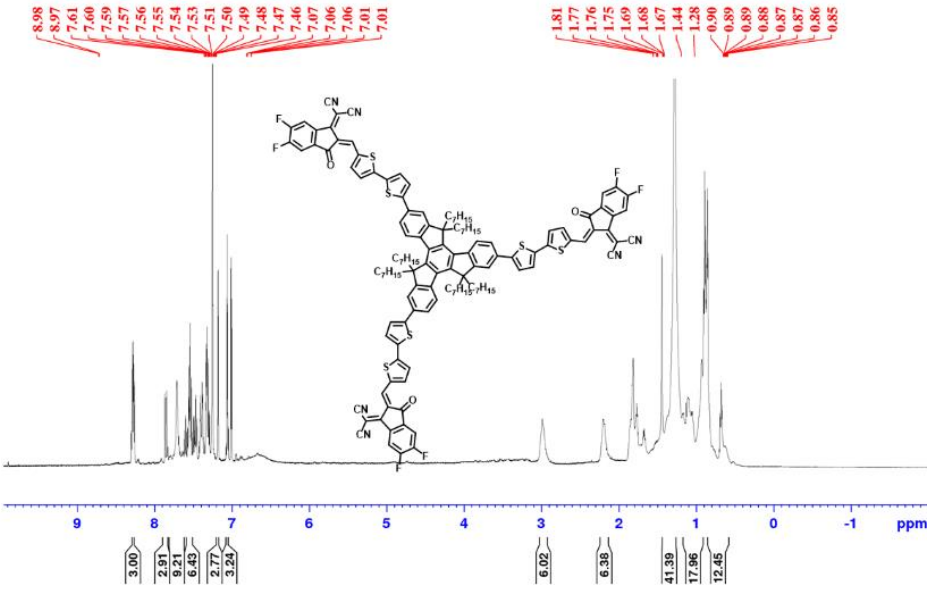

^{1}H NMR of Star-F

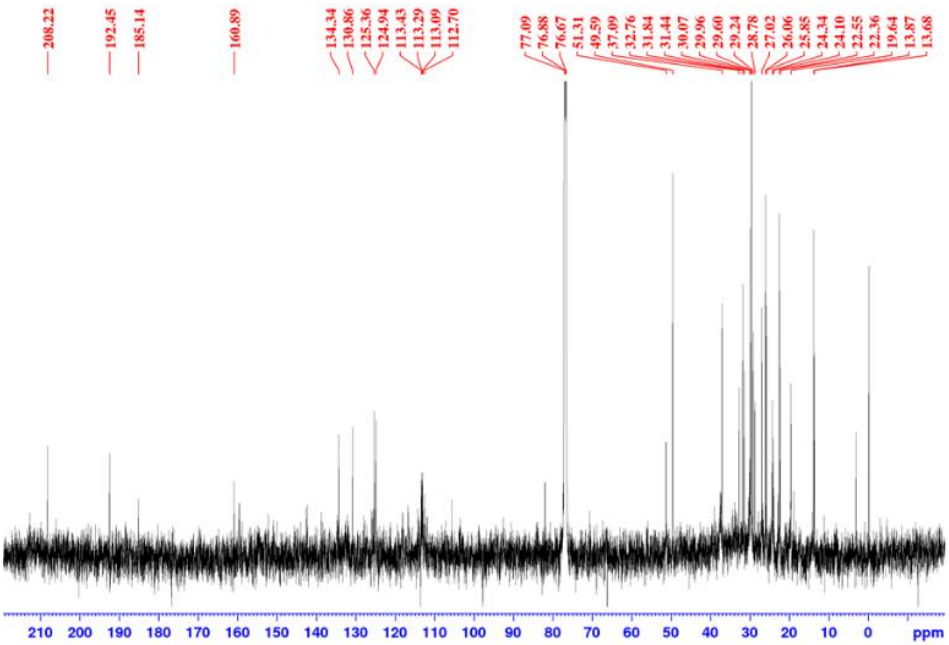

^{13}C NMR of Star-F

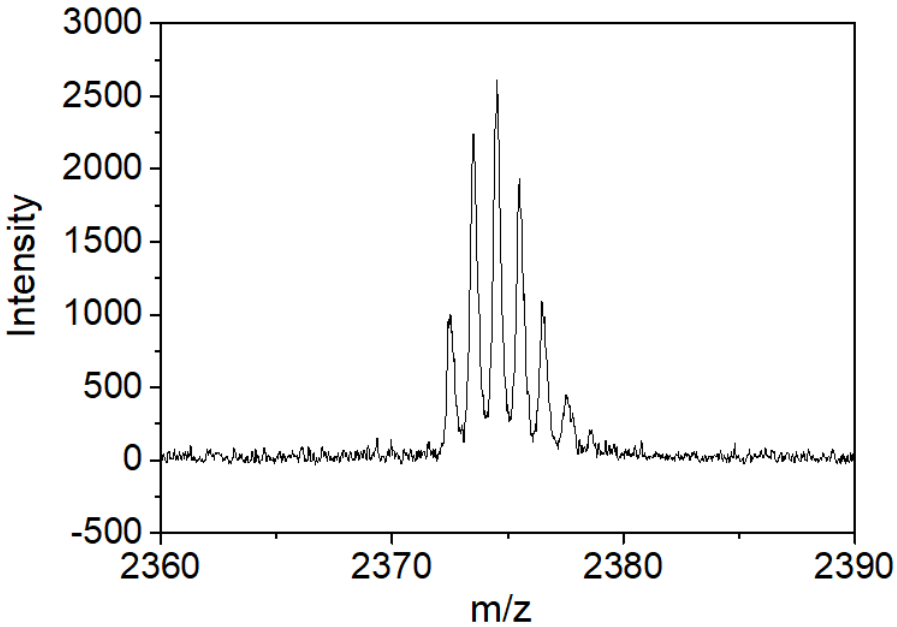

MALDI-TOF of Star-F

Density functional theory (DFT) calculations:

Density functional theory (DFT) calculations with the B3LYP/6-31G (d, p) basis set were performed utilizing Gaussian 09 to evaluate molecular conformations, energy levels and dipole moments. Particularly, Alkyl chains were replaced with a methyl or isobutyl group to simplify calculations and reduce computational time.

Organic solar cell device fabrication:

The OSCs were fabricated with the structure of ITO/PEDOT:PSS/active layer/Phen-NaDPO/Al. The ITO substrates were cleaned by ultrasonication with acetone and IPA for 10 min each and dried in a hot oven for 1 h. Then, the cleaned ITO substrates were treated by UV ozone for 1 h. PEDOT:PSS was spin coated on UV treated ITO substrates and annealed at 150°C for 10 min. For preparation of the active layer, 1:1.2 ratio of PM6:Y6 (16.8 mg/ml) was dissolved in chloroform (CF) with 1-chloronaphthalene (1-CN) (0.5%, v/v). And the Star-A or Star-F solution (1 wt% in CF) was added into PM6:Y6 blended solution with desired amounts (0, 0.5, 1, 2, 3%). The active layer was formed by spin coating at 5000 rpm in N_2-filled glove box. Phen-NaDPO layer was spin coated on active layer with 5000 rpm and Al was deposited by thermal evaporation under 2×10^{-6} Torr. The device area is 0.13 cm^2.

Space-charge limited current (SCLC) fabrication:

The hole and electron mobility of OSCs with and without Star-A or Star-F were measured by the space-charge limited current (SCLC) method. The device structures were ITO/PEDOT:PSS/active layer/MoO_3/Ag for hole-only devices and ITO/ZnO/active layer/Al for electron-only devices. The hole and electron mobility were determined by Mott-Gurney equation: $J_{SCLC} = \frac{9}{8}\varepsilon\varepsilon_0\mu\frac{V^2}{L^3}$, where J is dark current density, ε is the relative dielectric constant of the active layer, ε_0 is the permittivity of free space, μ is the charge carrier mobility, V is the internal voltage in the device, and L is the thickness of the active layer.

GIWAXS and GISAXS measurements:

For preparing grazing-incidence small-angle X-ray scattering (GISAXS) samples, silicon wafers of 1 by 1cm2 were used as substrates. Blend solutions with Star series additives (PM6:Y6, PM6:Y6:Star-A and PM6:Y6:Star-F) were spin coated on the substrates. The GISAXS analysis was conducted in the Pohang Accelerator Laboratory (beamline 9A, Republic of Korea), with incidence angle between 0.1°-0.3°.

3.3 Results and discussion

The synthetic routes of the star additives (Star-A, Star-F) are shown in **Figure 3.2**. The detailed synthetic procedures and characterization data are provided in the supporting information. The UV absorption characterization was performed to observe the relationship between the star additives and PM6 and Y6. The UV-Vis absorption spectra of the star additives in a dilute chloroform solution and the spin-coated film are presented in **Figure 3.3**, where the corresponding absorption properties are summarized in **Table 3.1**. The star additives, which absorb light in the near-ultraviolet region, do not interfere with the absorption of PM6 and Y6, where these additives do not affect the current density or device efficiency. The energy levels of the star additives were examined by cyclic voltammetry and are presented in **Figure 3.4**a-b. The highest occupied molecular orbital (HOMO) energy levels of Star-A and Star-F were calculated to be -5.41 and -5.42 eV, respectively (**Table 3.1**). The LUMO energy levels of the star additives were estimated from the optical bandgaps and HOMO energy levels. The star additives were synthesized with a finely controlled core, linker, and terminal group, which modulate the electron affinity (**Figure 3.4**). Furthermore, we also evaluated the ESP and optimized the structure of the star series through DFT while replacing the alkyl chains with methyl groups to simplify the calculations.

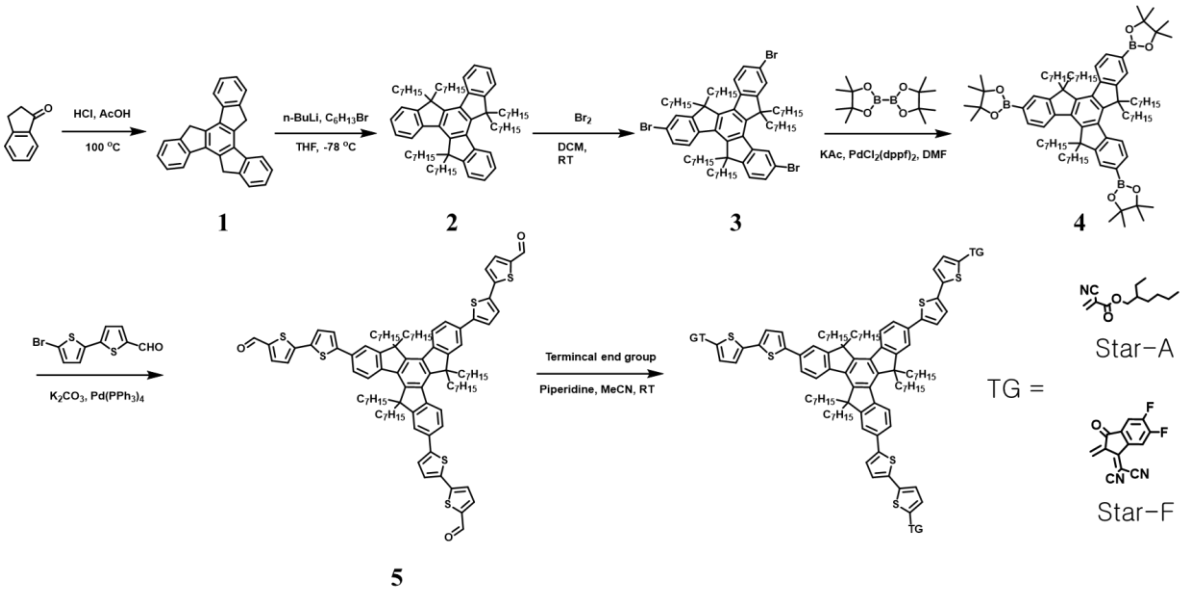

Figure 3.2. Synthesis scheme for Star series.

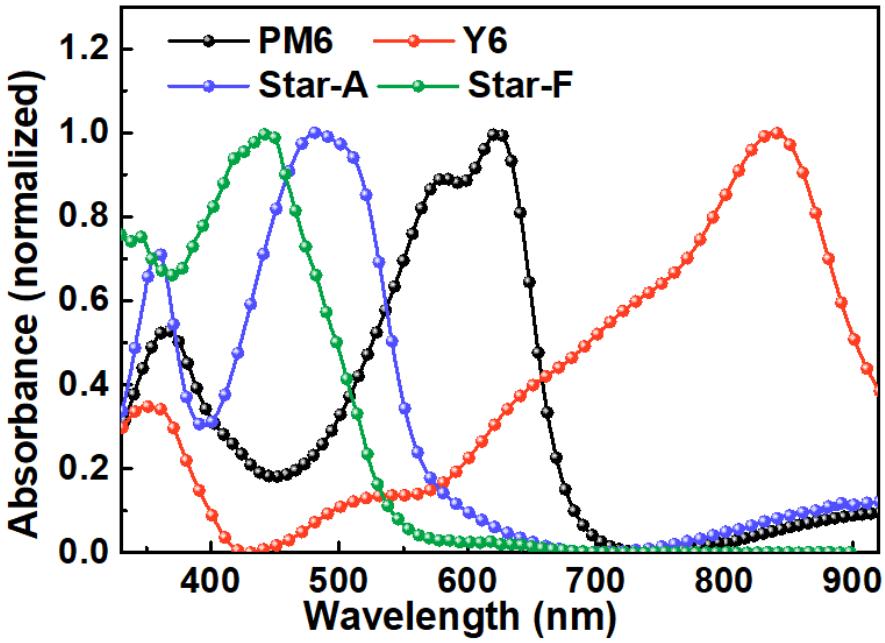

Figure 3.3. Normalized UV–Vis absorption spectra of the neat films (PM6, Y6, Star-A and Star-F).

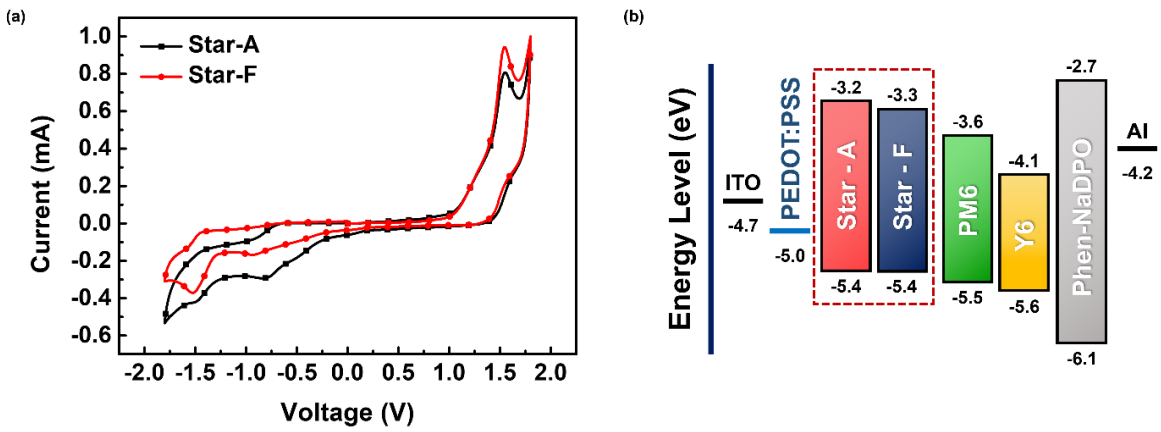

Figure 3.4. (a) Cyclic voltammogram (CV) and (b) Energy level diagram and architecture of the fabricated OSCs with star additives.

Table 3.1. Summary of the optical- and electrochemical properties.

Star additives	λ_{max}^{film} [nm]	λ_{edge}^{film} [nm]	$E_g^{opt.}$ [eV]	HOMO [eV]	LUMO [eV]
Star-A	485	558	2.22	-5.41	-3.19
Star-F	474	584	2.12	-5.42	-3.30

First, analysis of the ESP revealed that Star-A has a stronger negative potential at the terminal than Star-F and Star-F has a relatively stronger positive potential at the center. Overall, the star additives exhibited a positive potential at the center and a negative potential in the edge regions due to a strong electron withdrawing group at the terminal (**Figure 3.5**a). The local distribution of positive and negative potentials can lead to improved molecular compatibility.[129, 130] Next, the optimized geometrical structure was confirmed as a coplanar structure in the core. Although the linker and terminal group have planar structures, the dihedral angle in the region of connection between the linker and the core is twisted by about 25°, which is expected to exhibit a distorting effect. This twisting 3D structure prevents strong self-phase separation in D/A (**Figure 3.5**b and **Figure 3.6**).

To experimentally verify the compatibility impacts of the star additives, we calculated the Flory–Huggins's parameter (χ). We measured the contact angles of each film with water and glycerin, and calculated the surface tension (γ) using Wu's model.[131] In PM6, Y6, Star-A, and Star-F, respectively, the contact angles in water were 106.4°, 100.6°, 102.1°, and 102.6°, and the angles in glycerin were 90.8°, 82.8°, 85.6°, and 86.9° (**Figure 3.5**c and **Figure 3.7**). The corresponding surface tension values were 25.1, 32.5, 29.5, and 27.3 mN m^{-1}, respectively (**Table 3.2**), showing that the star additive surface tension ranges between those of PM6 and Y6. The Flory–Huggins interaction parameter was calculated using $\chi \propto (\sqrt{\gamma_{Donor}} - \sqrt{\gamma_{Acceptor}})^2$.[132] For PM6:Y6, we obtained a relatively high χ of 0.477. However, for PM6:Star-A, PM6:Star-F, Y6:Star-A, and Y6:Star-F, we obtained χ values of 0.177, 0.046, 0.072, and 0.226, respectively. These results imply that the star additives have an intermediate surface energy (**Table 3.3**). Consequently, the intermediate surface energy of the star additive is speculated to increase the miscibility of PM6 and Y6, thereby regulating the strong self-phase separation (**Figure 3.5d**). To verify the effect of the 1-CN solvent additive and star additives on the macroscopic phase

separation morphology, we observed the surface morphology using AFM. Of course, as confirmed in several other reports, the effect of the 1-CN solvent additive on themacroscopic phase separation morphology was very clearly observed in the AFM measurements, as shown in **Figure 3.8**. The PM6:Y6 film with the addition of star additives showed a slightly more developed grain morphology although the fibrillar morphology was almost identical. This proves that the star additives further modulate the nanoscale self-phase separation, optimizing the grain size.

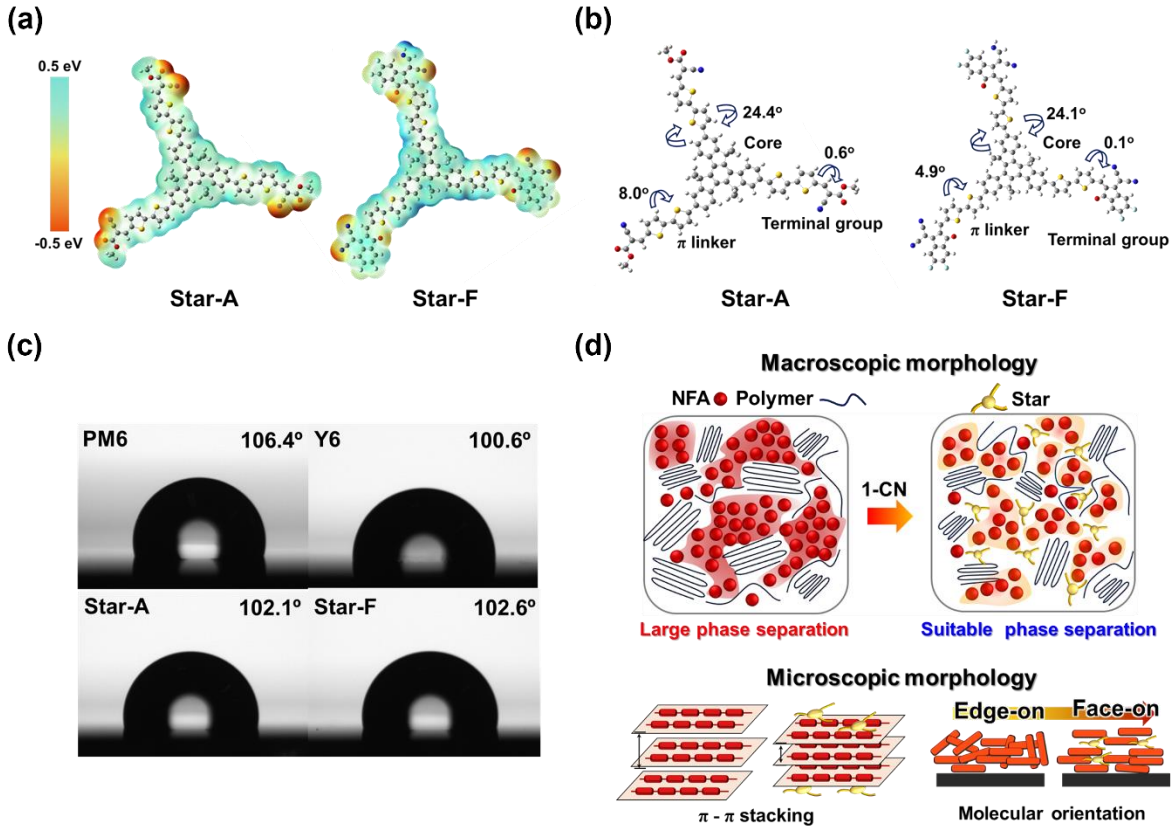

Figure 3.5. (a) Theoretical electrostatic potential distribution (ESP) and (b) optimized geometries and dihedral angles of the star additives (Star-A and Star-F). (c) Contact angles of water on PM6, Y6, Star-A, and Star-F films. (d) Schematic of the effect of introducing solid-solvent hybrid additives in blend systems.

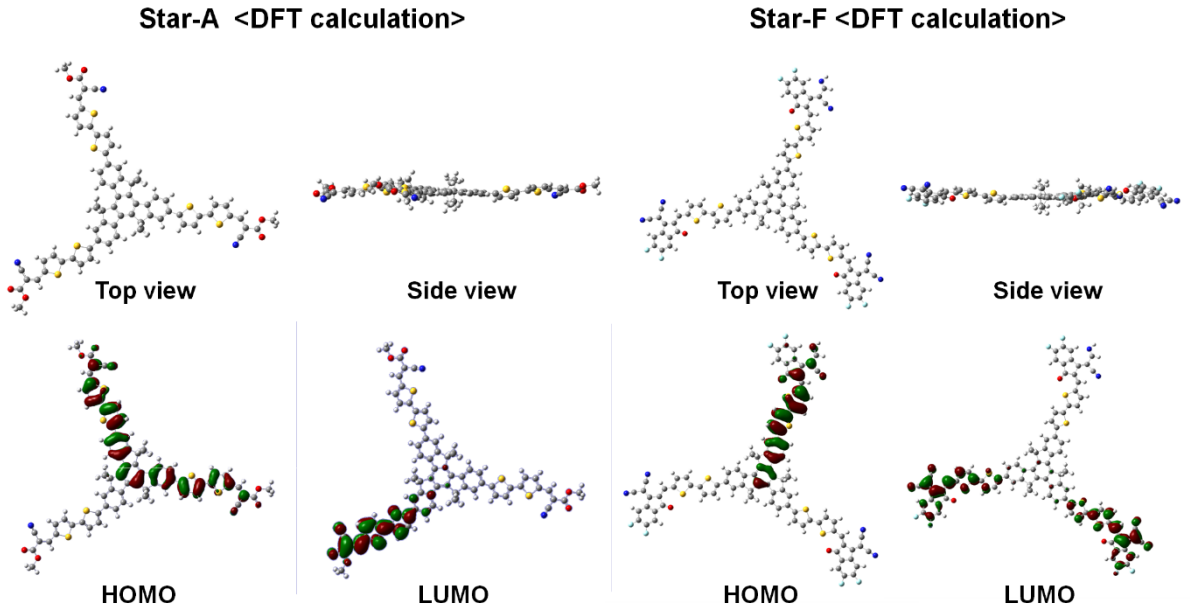

Figure 3.6. DFT calculation at B3LYP/6-31G (d,p) level. Top and side view of optimized molecular geometries of Star additives (Star-A and Star-F) and molecular orbital distribution.

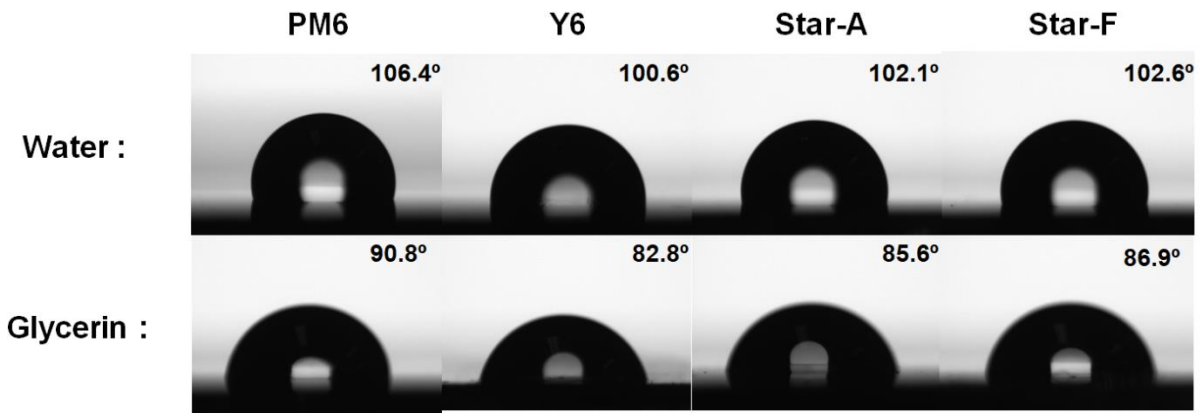

Figure 3.7. Contact angle of water and glycerin for PM6, Y6, Star-A and Star-F**.**

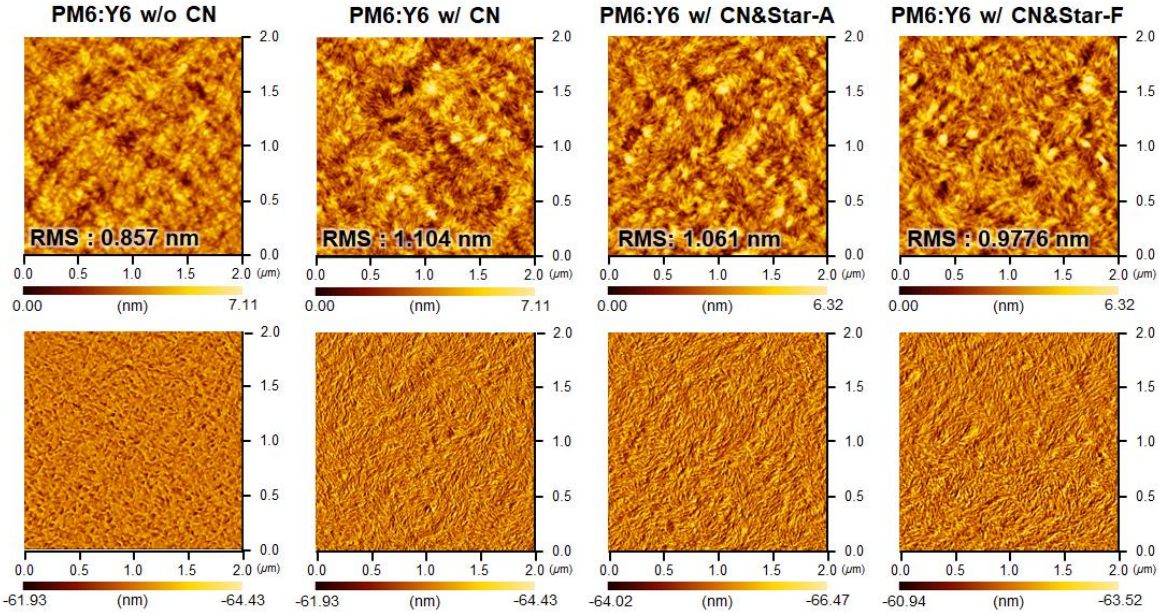

Figure 3.8. AFM height and phase images (2×2 μm^2) of binary and blend film with (or without) solvent additives (i.e. 1-CN) and Star additives.

Table 3.2. Surface energy analysis for Flory-Huggins interaction parameter.

	water	Glycerin	γ [mN m^{-1}]
PM6	106.4	90.8	25.1
Y6	100.6	82.8	32.5
Star-A	102.1	85.6	29.5
Star-F	102.6	86.9	27.3

Table 3.3. Calculation of Flory-Huggins interaction parameter.

$\chi \propto (\sqrt{\gamma_A} - \sqrt{\gamma_B})^2$	PM6:Y6	PM6:Star-A	PM6:Star-F	Y6:Star-A	Y6:Star-F
χ	0.477	0.177	0.046	0.072	0.226

To clearly observe the change in grain size, we carried out GISAXS experiments (**Figure 3.9**a-c). Based on the Guinier approximation given by[133-136]

$$I(Q) = I(0)exp\left(-\frac{Q^2R_g^2}{3}\right) \qquad \text{Equation (3.1)}$$

the gyration radius (R_g) of the donor and acceptor grain was calculated. Note that Q is given by the relation: Q= 4πsin(θ/2)/λ, where θ is the scattering angle and λ is the wavelength of incidence light. I(Q) is the scattering intensity at Q and I(0) is the zero-angle scattering intensity. The average grain size was calculated using the R_g extracted from the slope of ln(I(Q)) in the low-q region (0.005-0.02 Å). The PM6:Y6 blend with only 1-CN solvent additive yielded an average grain size of 96 nm. The PM6:Y6 blend with Star-A addition yielded a value of 81 nm and the PM6:Y6 blend with Star-F addition yielded a size of 78 nm. This result clearly indicates that the solid star additive further optimizes the phase separated grain size by increasing the blend miscibility (better mixing). The formation of a certain level of phase separated morphology by the star-series solid additives can also be confirmed with the solar cells fabricated with Star-A or Star-F alone (**Figure 3.10 and Table 3.4 and 3.5**). Although the results are somewhat lower than that of the device using 1-CN, the solar cells with only Star-A or Star-F alone without the 1-CN additive also showed quite good photovoltaic performances.

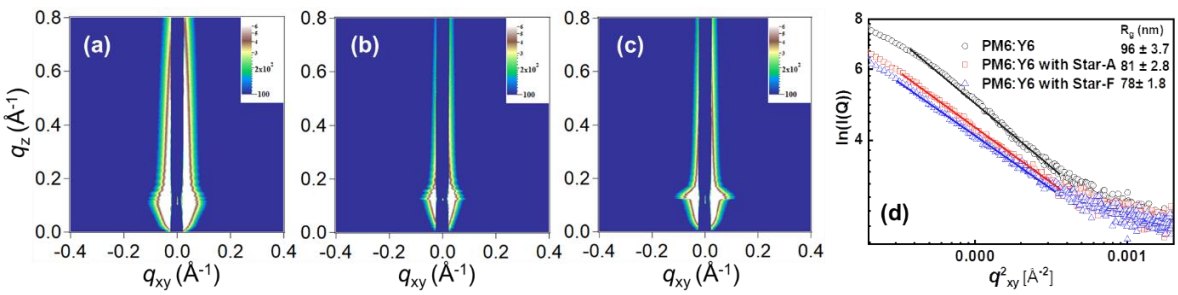

Figure 3.9. 2D-GISAXS patterns of binary and star-additive-blended films: (a) without solid star additives, (b) with Star-A, and (c) with Star-F. (d) In-plane profiles of each film.

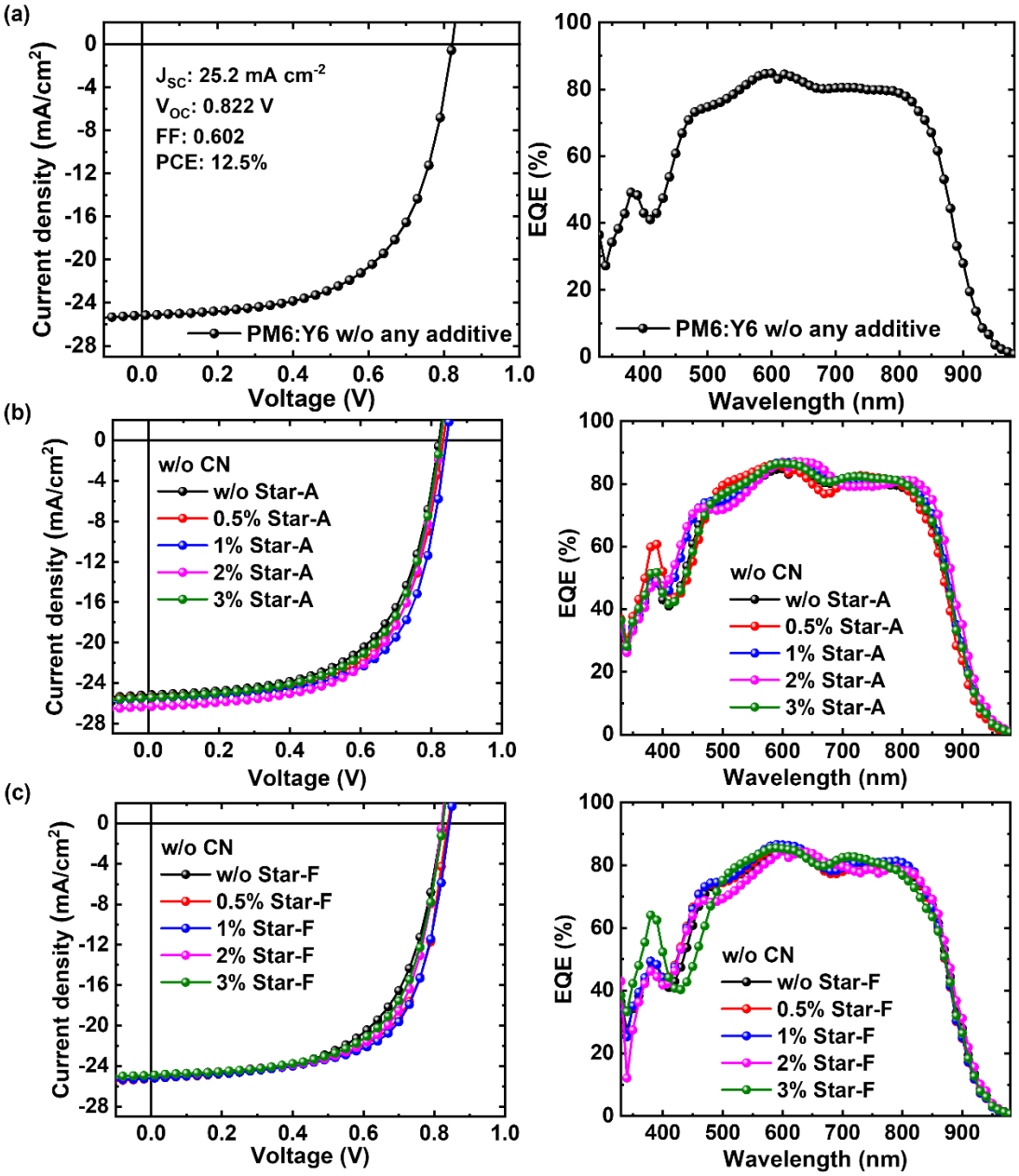

Figure 3.10. Photovoltaic parameters of all OSCs with different solid star additives contents (without solvent additive).

Table 3.4. Device performance parameters of the BHJ OSCs (without CN) with star-A additives.

w/o CN	J_{SC} [mA cm^{-2}]	V_{OC} [V]	FF	PCE [%]
w/o Star-A	25.2	0.822	0.602	12.5
0.5% Star-A	25.4	0.834	0.628	13.3
1% Star-A	25.5	0.843	0.644	13.9
2% Star-A	26.3	0.827	0.622	13.5
3% Star-A	25.4	0.825	0.613	12.9

Table 3.5. Device performance parameters of the BHJ OSCs (without CN) with star-F additives

w/o CN	J_{SC} [mA cm^{-2}]	V_{OC} [V]	FF	PCE [%]
w/o Star-F	25.2	0.822	0.602	12.5
0.5% Star-F	25.2	0.839	0.646	13.7
1% Star-F	25.2	0.843	0.654	13.9
2% Star-F	24.9	0.821	0.654	13.4
3% Star-F	24.9	0.824	0.630	12.9

To investigate the effect of the star additives on the microscopic π-π molecular packing, crystallinity, and crystal orientation inside grains, we conducted GIWAXS measurements. In **Figure 3.11**, the 2D GIWAXS patterns of each film are shown along with out-of-plane (OOP) and in-plane (IP) profiles. The polymer donor PM6 prefers edge-on orientation, while the acceptor Y6 aligns face-on. Star-A and

Star-F exhibit random orientations, implying that the 3D star-shaped structure hardly forms a specific crystal packing. The 2D GIWAXS patterns as well as OOP and IP profiles of PM6:Y6 blended with star additives films indicate a face-on orientation (**Figure 3.12**a). When the Star-A and Star-F additives are introduced, more prominent (010) diffraction peaks located at q_z = 1.73 and 1.72 $Å^{-1}$ appear in the OOP direction (**Figure 3.12**b). The π-π stacking distances calculated for the PM6:Y6:Star-A and PM6:Y6:Star-F blend films were 3.63 and 3.64 Å, respectively, which are shorter than the value of 3.72 Å of the PM6:Y6 binary film (**Table 3.6**). The shorter π-π stacking distance in the star additives enhanced the crystal packing of the blend film (i.e., PM6:Y6 blend) and it contributed to the charge transport efficiency. The full width at half maximum (FWHM) of the (010) diffraction peak was 0.2933 for the PM6:Y6 blend film and 0.2485 and 0.25895 for Star-A and Star-F, respectively. The π-π stacking crystallite coherence length (CCL_{010}) values estimated from Scherrer's equation through the FWHM[137] were 25.28 and 24.26 Å for the films blended with Star-A and Star-F, respectively, which are enhanced compared to that of the PM6:Y6 film (21.42 Å) (**Figure 3.12**c). In addition, the (100) azimuthal plot indicates that both star additives induce strong face-on orientation, facilitating vertical charge transport (**Figure 3.12**d). The full width at half maximum (FWHM) of the (010) diffraction peak was 0.2933 for the PM6:Y6 blend film and 0.2485 and 0.25895 for Star-A and Star-F, respectively. These results indicate that the star-series additives affect the blend film crystal structure by inducing closed π-π stacking in each crystal by embedding the crystal domain, simultaneously modulating the molecular orientation. Therefore, the GIWAXS results indicate that the addition of the star additives ultimately leads to a crystal structure conducive to efficient charge transport in the microscopic morphology.

Table 3.6. Crystal Coherence length of the (010) peak and the d-spacing for the blend film.

	q ($Å^{-1}$)	d-spacing (Å)	FWHM ($Å^{-1}$)	CCL (Å)
PM6:Y6	1.679	3.72	0.29327	21.42
PM6:Y6 with Star-A	1.726	3.63	0.24850	25.28
PM6:Y6 with Star-F	1.730	3.64	0.25895	24.26

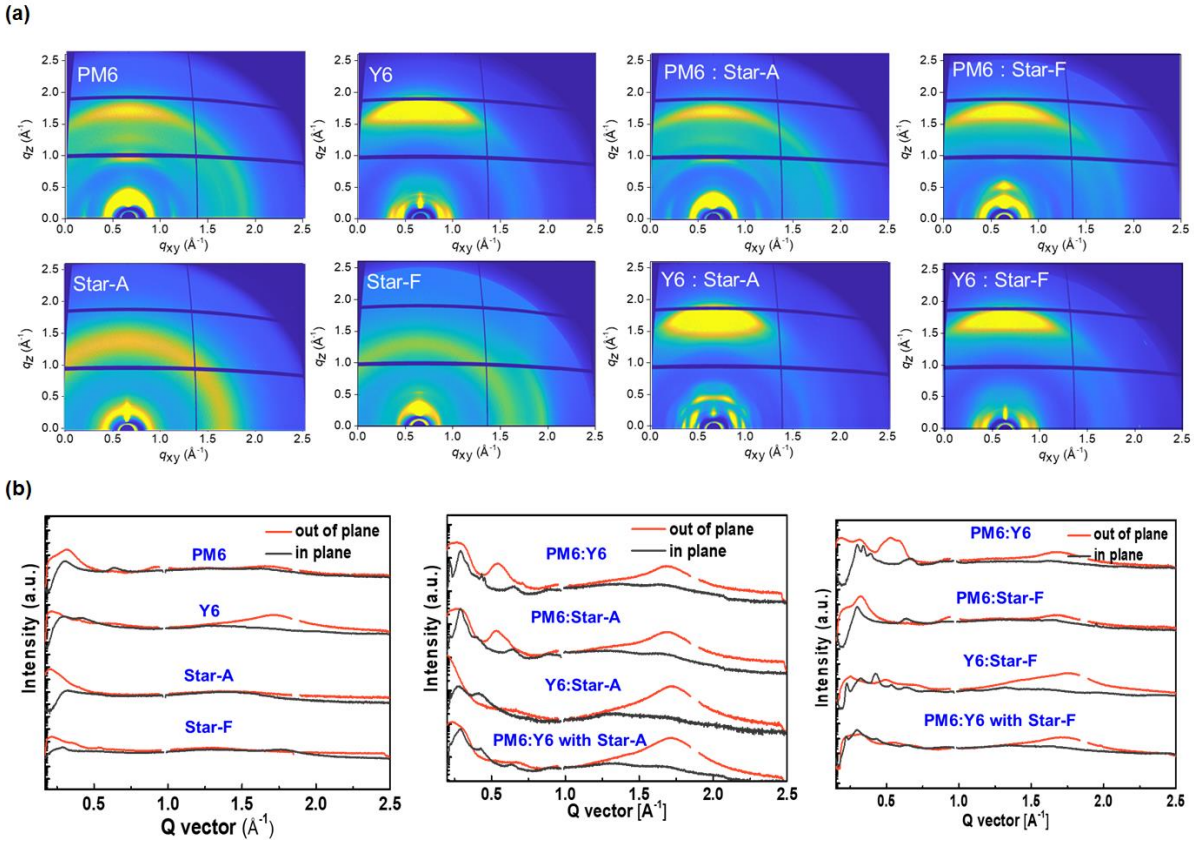

Figure 3.11. The analysis of 2D GIWAX pattern for (a) each neat film PM6, Y6, Star-A, Star-F and blend film and (b) the out-of-plane and in-plane line-cut profiles of the GIWAXS patterns in neat film, Star-A blend film and Star-F blend film.

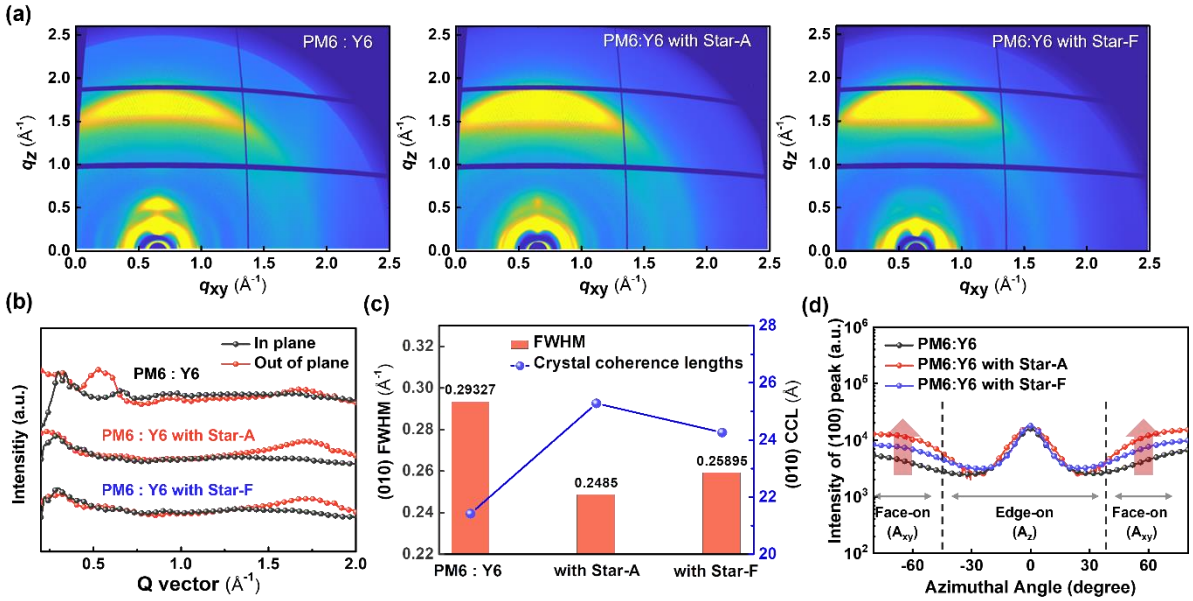

Figure 3.12. (a) 2D-GIWAXS patterns of binary and star additive-blended films. (b) In-plane and out-of-plane profiles. (c) Full width at half maximum (FWHM) and crystal coherence lengths of (010) peaks. (d) Azimuthal-angle scans for the (100) peaks in the GIWAXS patterns.

Further, we fabricated and characterized devices to verify their consistency with the microstructure results detailed above. For reference, we used binary OSCs based on PM6:Y6. The current density-voltage (J_{SC}-V_{OC}) curves of the optimized devices are presented in **Figure 3.13**a and the device parameters are summarized in **Table 3.7**. The optimization of the solid additive concentration is presented in **Figure 3.14 (Table 3.8)** and **Figure 3.15 (Table 3.9)**. The effect of the 1-CN solvent additive is shown in **Figure 3.10**. Significant degradation of photovoltaic properties due to the absence of solvent additives has been discussed in many other literatures and is omitted here. The PM6:Y6 binary OSC exhibited a PCE of 15.6% and V_{OC}, J_{SC}, and *FF* values of 0.850 V, 25.5 mA cm^{-2}, and 71.7%, respectively. Adding Star-A to the blend significantly increased V_{OC} to 0.871 V and *FF* to 74.2%, and slightly increased J_{SC} to 26.6 mA cm^{-2}, resulting in a PCE value of 17.2%. The Star-F blend exhibited slightly increased V_{OC} and *FF* values of 0.863 V and 73.3%, respectively, and a J_{SC} similar to the reference film, along with a PCE of 16.2%. **Figure 3.13**b displays a statistical diagram of the efficiencies. Interestingly, the star additive had the same effects on a variety of blend OSCs (e.g. PM6:ITIC-4F, PTB7-Th:Y6 and PTB7-Th:$PC_{71}BM$), improving the BHJ morphology (**Figure 3.16 and Table 3.10**).

To provide an in-depth understanding of how the star additives improve device parameters, we conducted a detailed device characterization. **Figure 3.13**c shows the photocurrent density (J_{ph}) versus effective voltage (J_{ph}–V_{eff}), which can help investigate the correlation of charge collection and exciton dissociation in the active layer. The detailed results are presented in **Table 3.11**. The J_{ph} increases linearly at the low V_{eff} range and saturates at a high V_{eff} (i.e., V_{eff} = 2 V). In the equation $J_{sat} = qG_{max}L$, G_{max} is the maximum possible exciton generation rate, J_{sat} is the saturation photocurrent density, q is the electronic charge, and L is the active layer thickness. Representing an increase from the 1.54×10^{28} $m^{-3}s^{-1}$ value of the PM6:Y6 blend, G_{max} was 1.68×10^{28} $m^{-3}s^{-1}$ when Star-A was added and it decreased to 1.50×10^{28} $m^{-3}s^{-1}$ for Star-F. These charge generation results are in agreement with the EQE results. We determined the exciton dissociation probability, P(E,T), from the ratio of J_{ph}/J_{sat}, obtaining values of 95.2%, 97.0%, and 97.5% for the PM6:Y6, Star-A, and Star-F blends, respectively. These results imply that both star additives contributed to the improvement of *FF* by promoting exciton dissociation. Next, we investigated the dependence of V_{OC} on the light intensity to analyze the recombination process. Generally, the slope is given by kT/q, where k is the Boltzmann constant, T is temperature in Kelvin, and q is the elementary charge. We obtained slopes of 2.06, 1.60, and 1.53 kT/q for PM6:Y6, PM6:Y6 with Star-A, and PM6:Y6 with Star-F, respectively. These results prove that the trap-assisted recombination is reduced in blend systems containing the star series (**Figure 3.13**d). The J_{SC} and light intensity (J_{SC}–P_{light}) curves are shown in **Figure 3.17**, where the parameter α was 1.012, 1.014, and 1.016 for PM6:Y6, PM6:Y6 with Star-A, and PM6:Y6 with Star-F OSCs, respectively, indicating that the bimolecular recombination effects were almost the same for all films.

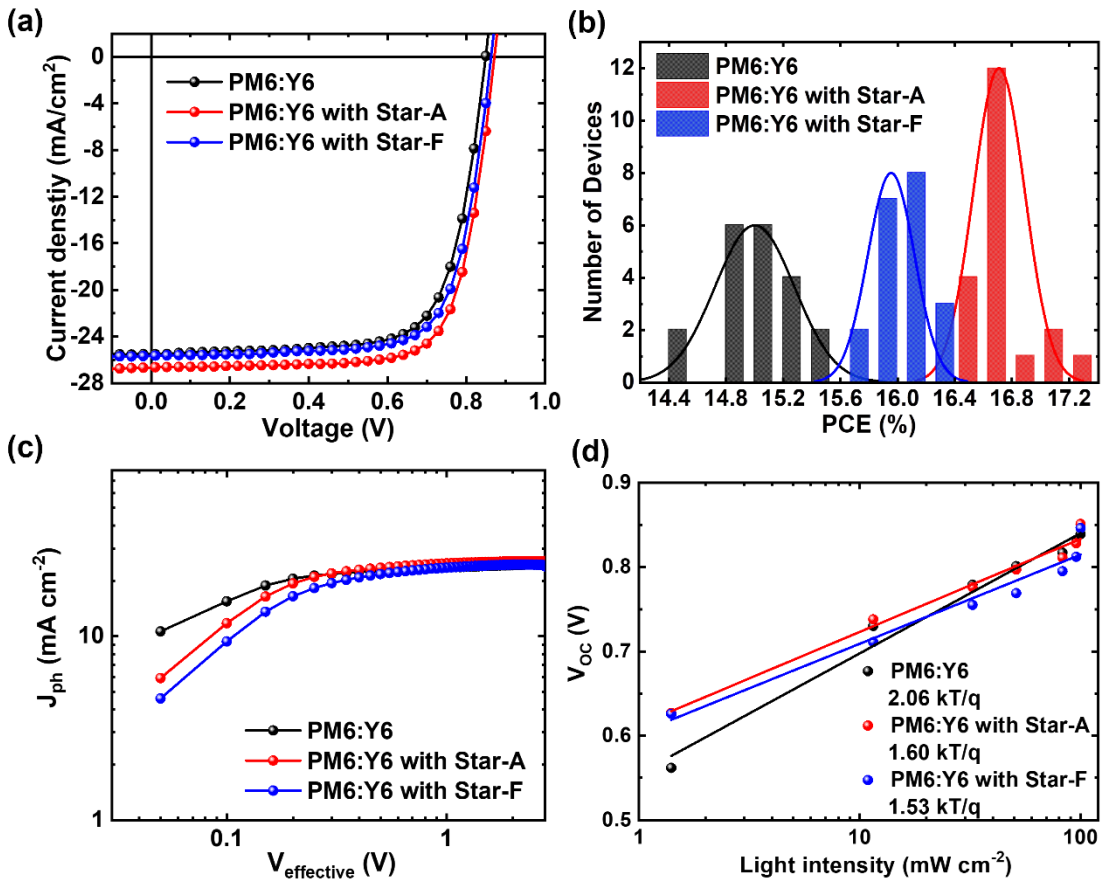

Figure 3.13. (a) Current–voltage (*J–V*) curves of the optimized PM6:Y6 binary and star additive-blended OSCs under AM 1.5G illumination at an intensity of 100 mW cm^{-2}. (b) PCE histograms of fabricated OSCs. (c) Photocurrent density (J_{ph}) vs. effective bias ($V_{effective}$) for the optimized OSCs. (d) *Voc* versus light intensity for the optimized OSCs.

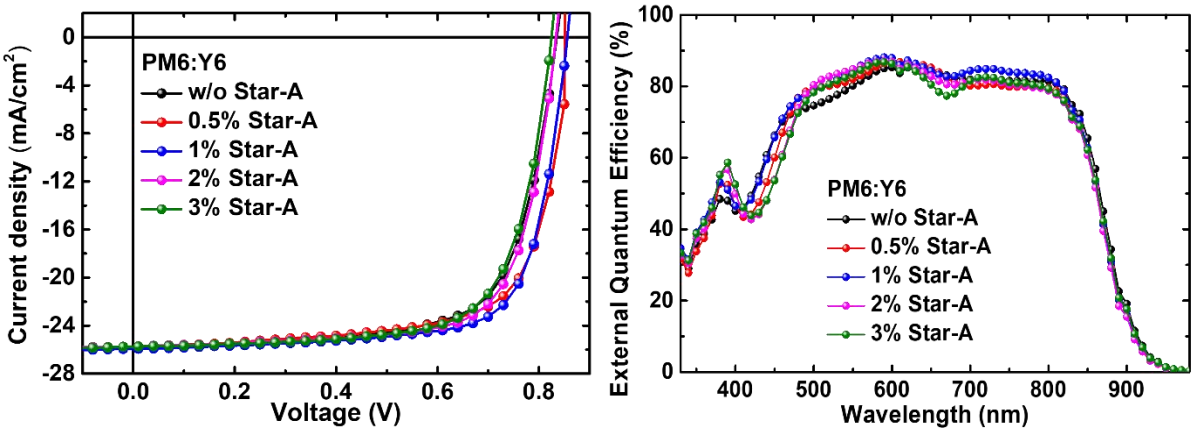

Figure 3.14. Photovoltaic parameters of all OSCs with different Star-A additives contents (hybrid solid-solvent additive).

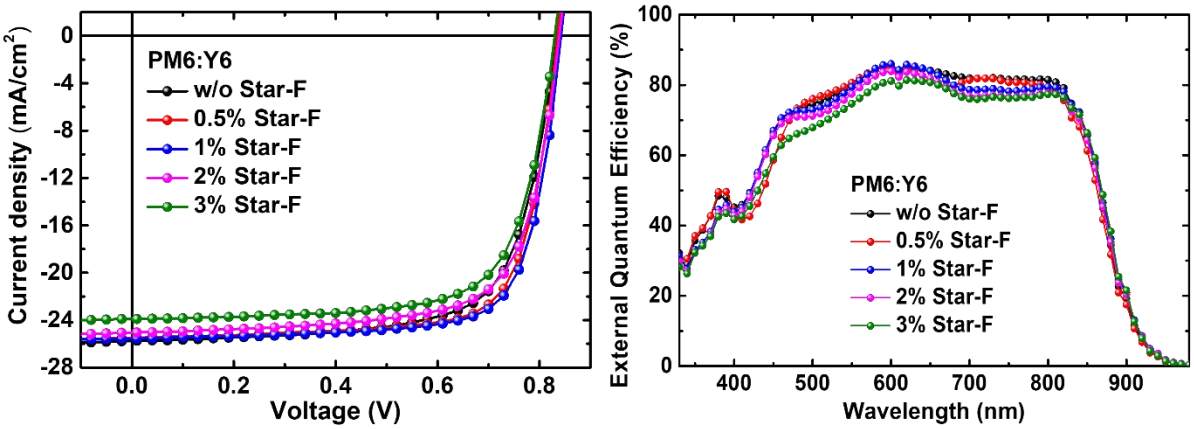

Figure 3.15. Photovoltaic parameters of all OSCs with different Star-F additives contents (hybrid solid-solvent additive).

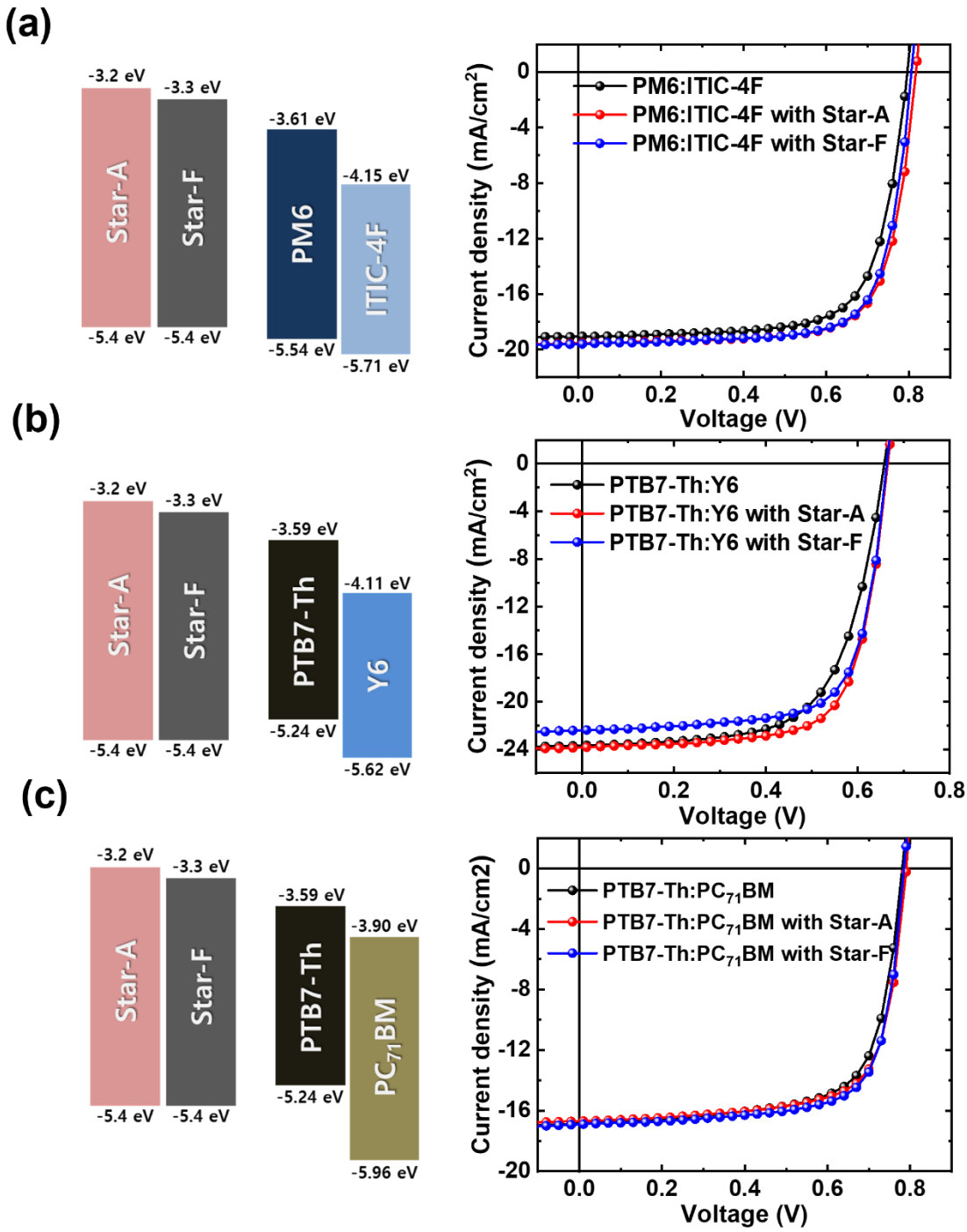

Figure 3.16. Universality of the solid-solvent hybrid additives strategy. Photovoltaic performance of investigated (a) PM6:ITIC-4F, (b) PTB7-Th:Y6, and (c) PTB7-Th:$PC_{71}BM$ blends introduced by star additives.

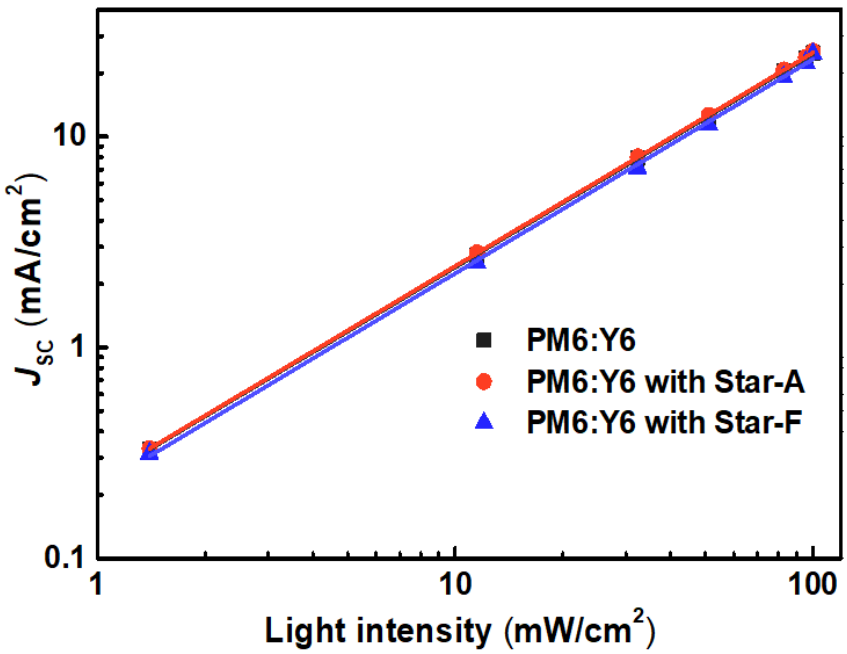

Figure 3.17. J_{SC}–P_{light} curves of the binary and star-additive-blended films.

Table 3.7. Device performance parameters of the optimized BHJ OSCs without and with star additives.

Blend composition	J_{SC} [mA cm^{-2}]	V_{OC} [V]	FF	PCE [%]
PM6:Y6	25.5	0.850	71.7	15.6
PM6:Y6 with Star-A	26.6	0.871	74.2	17.2
PM6:Y6 with Star-F	25.7	0.863	73.3	16.2

Table 3.8. Device performance parameters with different Star-A additives contents (hybrid solid-solvent additive).

	J_{SC} [mA cm^{-2}]	V_{OC} [V]	FF	PCE [%]
w/o Star-A	25.7	0.835	0.702	15.1
0.5% Star-A	25.8	0.851	0.717	15.7
1% Star-A	25.9	0.856	0.733	16.3
2% Star-A	25.8	0.834	0.725	15.6
3% Star-A	25.7	0.825	0.714	15.2

Table 3.9. Device performance parameters with different Star-F additives contents (hybrid solid-solvent additive).

	J_{SC} [mA cm^{-2}]	V_{OC} [V]	FF	PCE [%]
w/o Star-F	25.7	0.836	0.706	15.2
0.5% Star-F	25.5	0.836	0.746	15.9
1% Star-F	25.6	0.842	0.751	16.2
2% Star-F	25.0	0.839	0.713	15.2
3% Star-F	23.9	0.830	0.714	14.2

Table 3.10. Device performance parameters of PM6:ITIC-4F, PTB7-Th:Y6, and PTB7-Th:$PC_{71}BM$ blends introduced by star additives.

		J_{SC} [mA cm^{-2}]	V_{OC} [V]	FF	PCE [%]
PM6:ITIC-4F	w/o	19.1	0.796	0.717	10.9
	w Star-A	19.5	0.817	0.737	11.8
	w Star-F	19.6	0.806	0.740	11.7
PTB7-Th:Y6	w/o	23.7	0.658	0.644	10.0
	w Star-A	23.8	0.665	0.704	11.2
	w Star-F	22.4	0.663	0.711	10.6
PTB7-Th:$PC_{71}BM$	w/o	16.8	0.781	0.702	9.22
	w Star-A	16.7	0.791	0.720	9.51
	w Star-F	16.9	0.785	0.731	9.69

Table 3.11. G_{max} and P(E,T) of the optimized OSCs based on different BHJ blends using star additives.

Blend composition	G_{max} (m^{-3}s^{-1})	P(E,T)
PM6:Y6	1.54×10^{28}	95.2%
PM6:Y6 with Star-A	1.68×10^{28}	97.0%
PM6:Y6 with Star-F	1.50×10^{28}	97.5%

To further study the charge recombination process, we examined the effect of the star series additives on photo-carrier decay dynamics, including charge recombination and charge-extraction processes, through transient photocurrent (TPC) and transient photovoltage (TPV) analyses (**Figure 3.18**a-b). The device without star additives exhibited a charge recombination lifetime (τ_r) of 1.39 μs, where PM6:Y6 with Star-A and Star-F displayed longer lifetimes of 4.94 and 5.86 μs, respectively (**Figure 3.18**a). These results demonstrate that the photo-generated charge recombination process is faster in the device without star additives than in those blended with star additives. The remarkably reduced nonradiative recombination of the OSC blended with the star series indicates the suppression of the charge recombination process and the reduction of energy loss due to a suitable V_{OC}.[138] In the TPC traces (**Figure 3.18**b), the charge-extraction time (τ_t) of the device without star additives was 0.455 μs and the extraction times of the devices blended with Star-A and Star-F were shorter with values of 0.337 and 0.275 μs, respectively. These results indicate that both star additives can effectively enhance the charge extraction.[139] To verify the improvement of charge dynamics, we fabricated a space charge limited current (SCLC) device to investigate the charge mobility by employing electron-only and hole-only devices configurations. The charge mobility curves and values are shown in **Figure 3.18**c, d, and **Table 3.12**. The hole mobility (μ_h) of the devices blended with the star additives are 3.04×10^{-4} (Star-A) and 3.31×10^{-4} $cm^2V^{-1}s^{-1}$ (Star-F), which are significantly higher than that of the binary blend device, 2.06×10^{-4} $cm^2V^{-1}s^{-1}$. The electron mobility (μ_e) follows the same trend as the hole mobility with values of 3.89×10^{-4} and 3.99×10^{-4} $cm^2V^{-1}s^{-1}$ for the devices with Star-A and Star-F, respectively, which are slightly higher than that of the reference device, 3.72×10^{-4} $cm^2V^{-1}s^{-1}$. Furthermore, since the relatively low hole mobility increased significantly, the charge balance, μ_e/μ_h, was 1.81 for PM6:Y6, but 1.28 when Star-A was included, which greatly improved to 1.21 for Star-F. Therefore, we concluded that the star additives reduce charge recombination by regulating the phase separation in the BHJ, which is consistent with our microstructure analyses.

Since the star-series additives were introduced at only 1.0 wt.%, they probably do not significantly influence the energy level distribution of D/A. A small amount of the Star-A and Star-F solid additives does not create a phase of their own. This is why we treat Star-A and Star-F as a solid additive and not the third component of a ternary device. Nevertheless, a clear V_{OC} change was observed in the *J-V* characteristics. Under the situation where the energy level distribution is not likely to change, the change of V_{OC} is probably associated with energy loss of the charge carriers. In terms of the Shockley–Queisser (SQ) model,[140-142] the device performance limit of the OSCs is mainly restricted by the optical bandgap, E_g, of the BHJ photoactive materials and the energy loss, E_{loss}, of the device. Thus, the PCE limit can be overcome via E_{loss} control. In general, E_{loss} during photo-induced charge dissociation and charge recombination processes comprises three parameters, as follows.

$$E_{loss} = \left(E_g - qV_{OC}^{SQ}\right) + qV_{OC}^{rad} + qV_{OC}^{nonrad} = \Delta E_1 + \Delta E_2 + \Delta E_3 \qquad \text{Equation (3.2)}$$

We analyzed the energy loss using the Fourier-transform photocurrent spectroscopy external quantum efficiency (FTPS-EQE) and electroluminescence (EL) spectra measurements (**Figure 3.19**a). Detailed values of the energy loss parameter are presented in **Table 3.13**. The first term (ΔE_1; $E_g - qV_{OC}^{SQ}$) of E_{loss} is associated with the SQ-limit of unavoidable energy loss, determined by E_g and the Schockley–Quisser limit V_{OC} (V_{OC}^{SQ}) of the device. We estimated the E_g by using the bandgap distribution from derivatives of the EQE (**Figure 3.20**).[143] The calculated values of E_g and V_{OC}^{SQ} are similar in the devices with and without star additives. Therefore, we obtained a similar ΔE_1 value of 0.291 eV for the PM6:Y6, PM6:Y6 with Star-A, and PM6:Y6 with Star-F devices.

The second term (ΔE_2; $qV_{OC}^{SQ} - qV_{OC}^{rad}$) of E_{loss} is related to radiative recombination loss and has a similar value for the devices with and without star additives. This is because the energy level of the star series does not significantly affect the D/A energy level offset. However, the third term (ΔE_3; $qV_{OC}^{SQ} - qV_{oc}$), related with nonradiative recombination loss, exhibits lower values for the devices with Star-A (0.224 eV) and Star-F (0.236 eV) than those for the device without star additives (0.240 eV). This indicates that the star series additives effectively reduce nonradiative recombination through morphology improvement, lowering the E_{loss} and increasing V_{OC}. As shown in **Figure 3.19**b, the PM6:Y6 blend device without star additives exhibits a ΔE_{loss} of 0.581 eV, where star additive blending induces ΔE_{loss} decreases of 0.563 eV (Star-A) and 0.575 eV (Star-F). Consequently, as evident in the *FF* and V_{OC} statistical diagrams of the device parameters, star additives increase the *FF* through improved blend morphology, where the effect is particularly prominent for Star-A (**Figure 3.19**c). Interestingly, the Star-A additive suppressed the nonradiative recombination and energy loss, resulting in an improved V_{OC} (**Figure 3.19**d).

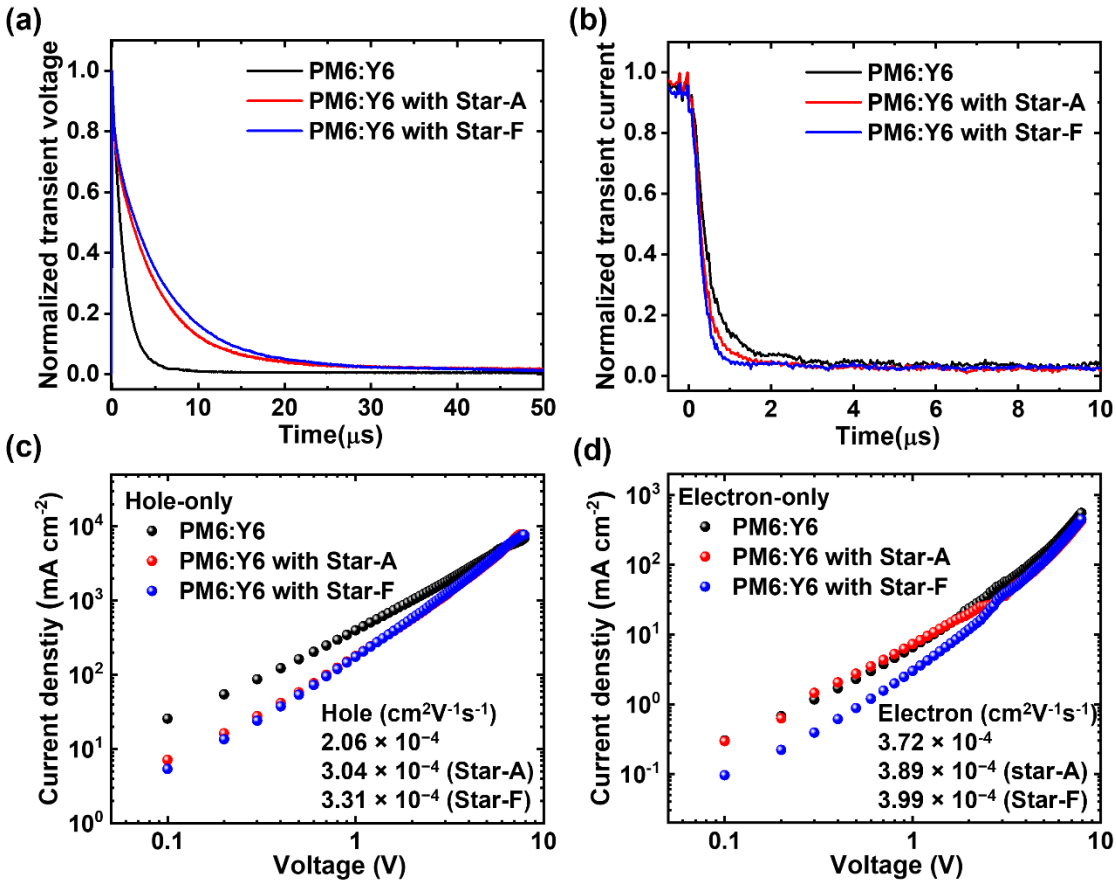

Figure 3.18. (a) Normalized transient photovoltage (TPV) decay of the optimized OSCs. (b) Normalized transient photocurrent (TPC) decay of the optimized OSCs. (c),(d) Current–voltage (*J*–*V*) characteristics of hole-only and electron-only devices, according to the SCLC.

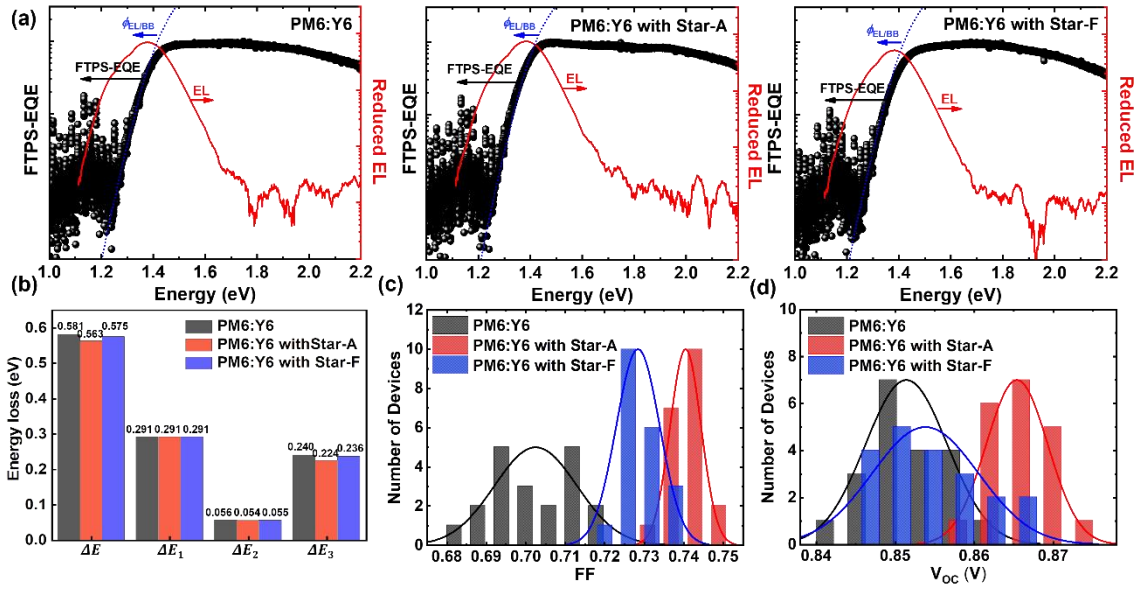

Figure 3.19. (a) FTPS-EQE and EL profiles of the optimized OSCs. The external quantum efficiency is determined by the EL and blackbody emission. (b) Energy loss values, ΔE, ΔE_1, ΔE_2, and ΔE_3, of the optimized OSCs. (c) *FF* and (d) *Voc* histograms of the OSCs.

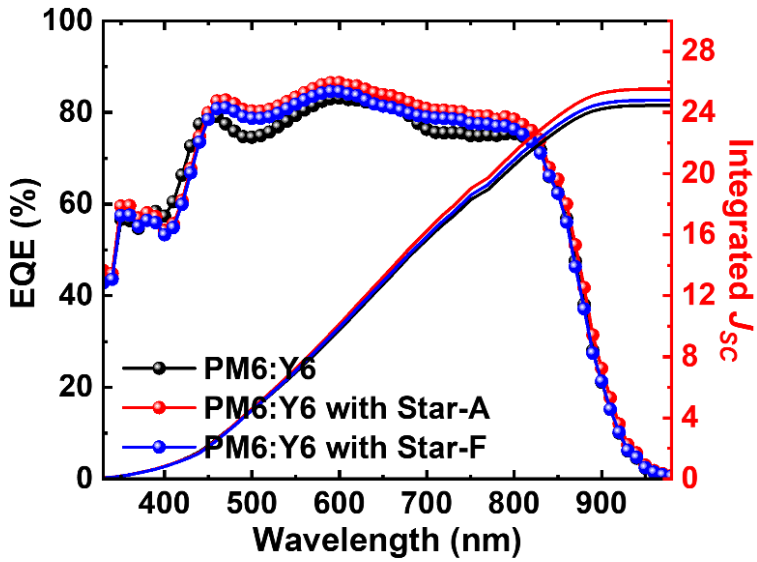

Figure 3.20. External quantum efficiency (EQE) spectra of optimized OSCs.

Table 3.12. Charge mobility and charge mobility ratio calculation from SCLC devices.

	μ_h [$cm^2V^{-1}s^{-1}$]	μ_e [$cm^2V^{-1}s^{-1}$]	μ_h/μ_e	μ_e/μ_h
PM6:Y6	2.06×10^{-4}	3.72×10^{-4}	0.554	1.81
PM6:Y6 with Star-A	3.04×10^{-4}	3.89×10^{-4}	0.781	1.28
PM6:Y6 with Star-F	3.31×10^{-4}	3.99×10^{-4}	0.830	1.21

Table 3.13. Total energy loss (E_{loss}) and various parameters that contribute to E_{loss} in PM6:Y6 and PM6:Y6 with star additive OSCs based on the different BHJ blends.

	E_g [eV]	V_{OC}^{SQ} [eV]	V_{OC}^{rad} [eV]	V_{OC} [eV]	ΔE_1 [eV]	ΔE_2 [eV]	ΔE_3 [eV]	ΔE_{loss} [eV]
PM6:Y6	1.422	1.131	1.075	0.835	0.291	0.056	0.240	0.581
PM6:Y6 with Star-A	1.425	1.134	1.080	0.856	0.291	0.054	0.224	0.563
PM6:Y6 with Star-F	1.424	1.133	1.078	0.842	0.291	0.055	0.236	0.575

3.4 Conclusion

In summary, we introduced a solid-solvent hybrid additive on PM6:Y6 non-fullerene solar cells. For the solvent additive, a well-known 1-CN solvent additive was utilized to optimize the macroscopic donor-acceptor phase separation morphology. For the solid additive to further optimize the microscopic morphology, two types of solid semiconducting additives with 3D star-shaped structures were carefully designed and synthesized based on DFT calculations to provide enhanced electrical properties, partially different ESP properties, and optimized geometrical structures (Star-A, Star-F). As a result, the best efficiency of 17.2% was achieved with only 1% addition of the star-series solid additives. The star-shaped additives enhanced the device *FF* and reduced the energy loss by modulating the BHJ morphology, which improved the charge transport and balance in the blend of PM6 and Y6. In this study, we demonstrated, for the first time, a new approach to improve device efficiency with an improved FF and reduced energy loss by using a solid-solvent hybrid additive composed of a common co-soluble solvent additive and semiconducting solid additives using a novel design strategy. In the field of organic solar cells, our approach will provide new research guidelines for hybrid additive approaches to improve efficiency by controlling both the macroscopic and microscopic morphologies.

Chapter 4. Long-Term Stable Non-Fullerene based Inverted Organic Photovoltaic Devices with an Efficiency of 17.42%

4.1 Research background

Solution-processed organic photovoltaic (OPV) devices based on the bulk-heterojunction (BHJ) active layers have attracted great interest based on their potential as low-cost portable energy sources.[144-148] Recent advances in narrow-bandgap non-fullerene acceptors (NFA) have boosted the power conversion efficiency (PCE) of single-junction OPVs to >17%, which may be sufficient for commercialization.[149-151] Thus far, the Y6 (and its derivatives) has been the current state-of-the-art NFA with the combination of a wide-bandgap polymer donor, PM6 (also known as PBDB-TF).[7, 102, 152, 153] However, all the reported high-efficiency PM6:Y6 based OPV devices (PCE >17%) were fabricated with a conventional architecture (see **Table 4.1** in Supporting Information), which is known to have poor environmental stability.[150, 154]

In the literature, it is widely known that the OPVs with inverted architecture (i-OPV) have superior environmental stability to the conventional structure device (c-OPV) due to the use of higher work-function metal electrodes and non-acidic hole-transport layers (HTLs).[155, 156] The i-OPVs typically employ metal-oxides as the charge transport layers because they have high electron conductivity, excellent optical transmittance, appropriate work function, and good chemical stability. For instance, the non-acidic MoO_3 layer has been employed as an HTL,[157-159] and solution-processed n-type metal oxides such as ZnO, TiO_2, and SnO_2 have often been used for the electron transport layer (ETL).[160-162] Thus far, however, there is no report on the PM6:Y6 based i-OPVs, which can achieve an equivalently high PCE as the c-OPV counterparts. The reported PCEs of the PM6:Y6 based i-OPVs have ranged from 15.7% to 16.5% (See **Table 4.1** in Supporting Information). Furthermore, the reported i-OPVs have not particularly shown improved long-term stability compared to the c-OPV counterpart.

In i-OPVs, the interfacial properties between BHJ active layers and solution-processed metal-oxide charge transport layers are critical in determining their PCE and stability. The interfacial alignment of energy levels between a transparent conductive electrode and active layers influences the internal electric field of the device, while the interfacial defect sites play a vital role in charge recombination.[163-167] Furthermore, the oxygen vacancies on the metal oxides can form net positive charges due to the

empty orbital, which induces coordination with electron-rich functional groups in the active materials.[168, 169] Therefore, the passivation of the metal oxide surface is essential to minimize electron trapping defect sites in the devices. In the literature, several passivation methods to mitigate the defects of metal oxides have been reported. Insertion of self-assembled monolayers (SAMs),[170, 171] or ether group-containing polymers such as poly(ethylene oxide) (PEO) and poly(ethylene glycol) (PEG), and treatment with polar solvents such as ethanolamine and dithiols[172-175] have been attempted. However, most previous studies have focused on improving interfacial charge collection efficiency. In contrast, the long-term effects of defect sites on the stability of devices have not been explored sufficiently.

In this work, we developed the long-term stable PM6:Y6 based i-OPVs with a PCE of 17.42%, which is as high as the current state-of-the-art c-OPVs, by resolving the origins of suboptimal performance. While the defect sites at the BHJ/ZnO-ETL interfaces were the crucial factor for the deterioration of device charge extraction efficiency, they also accelerate the degradation of i-OPVs by propagating deep and shallow traps. After long-term storage or illumination, the short circuit current density (J_{SC}) and fill factor (FF) of i-OPVs were deteriorated by the increase in deep interfacial traps. At the same time, the penetrative oxygen-containing defects generated shallow traps near the band-edge of the Y6 in the active layers reducing the open-circuit voltage (V_{OC}) of i-OPV. The suppression of the interfacial defects by a chemical modification with 1,2-ethanedithiol (EDT), improved the PCE of i-OPV significantly from 15.54% to 17.42%. Furthermore, the inhibition of the oxygen-containing interfacial defects significantly improved the long-term storage- and photo- stability of i-OPVs. The modified i-OPV (mi-OPV) showed 90% and 80% retention of the original PCE after 1200 h of air storage and illumination, respectively, whereas the pristine i-OPV showed only 51% and 54%.

Table 4.1. Summary of high-efficiency OPV devices in the literature.

No.	Active material	Performance				Device structure	Stability			Ref.
		V_{OC} (V)	J_{SC} (mA/cm^2)	FF	PCE (%)		Photo Stability	Storage Stability	Thermal Stability	
1	PBDTSF-TZNT : F8IC : F8OIC : $PC_{71}BM$	0.80	25.28	74.80	15.12	Conventional	Yes	Yes	No	176
2	PM7 : ITC-2Cl : IXIC-4Cl	0.86	23.99	74.70	15.37	Conventional	No	Yes	No	177
3	PM6 : Y6	0.83	25.30	74.80	15.70	Conventional	No	No	No	102
4	PM6 : Y6	0.82	25.20	76.10	15.70	Inverted	No	No	No	178
5	P2f-EHp : Y6	0.81	26.68	74.11	16.02	Conventional	No	No	No	179
6	P2f-EHp : Y6	0.78	24.94	67.30	13.13	Inverted	No	No	No	180
7	PBDB-T -SF : Y6 : ITCT	0.89	24.75	73.67	16.14	Conventional	No	No	No	181
8	W1 : Y6	0.88	25.87	70.70	16.16	Conventional	No	No	No	182
9	PTQ10 : Y6	0.87	24.81	75.10	16.21	Conventional	No	No	No	183
10	PM6 : IT4F : Y6	0.84	25.40	75.90	16.27	Conventional	No	No	No	65
11	PM6 : Y6 : IN-4F	0.85	25.7	74.50	16.3	Conventional	No	No	No	184
12	PSFTZ : Y6	0.81	26.45	76.30	16.35	Conventional	No	No	No	185
13	PM6 : BTP-4F-12	0.86	25.30	76.00	16.40	Conventional	No	No	No	186
14	S1 (Cop) : Y6	0.88	25.4	73.70	16.42	Conventional	No	No	No	187
15	PM6 : BTP-4Cl	0.87	25.40	75.00	16.50	Inverted	No	No	No	188
16	PM6 : $PC_{61}BM$: Y6	0.85	25.40	0.77	16.50	Inverted	No	No	No	189
17	PM6 : IDIC : Y6	0.87	25.39	74.92	16.51	Conventional	No	No	No	190
18	PTQ10 : Y6	0.83	26.65	75.10	16.53	Conventional	No	No	No	191
	SM1 : PM6 : Y6	0.83	25.70	77.50	16.55	Conventional	No	Yes	No	
19	PM6 : Y6	0.84	25.97	0.76	16.56	Conventional	No	No	No	192
20	PM6 : $PC_{71}BM$: Y6	0.85	25.70	76.35	16.67	Conventional	No	Yes	No	193
21	PM6 : $PC_{71}BM$: Y6	0.86	25.10	77.20	16.70	Conventional	No	No	No	194
22	PBDB-T-2Cl : Y6 : $PC_{71}BM$	0.87	25.44	75.66	16.71	Conventional	No	No	No	195
	D16 (PBDTDTTP) : Y6	0.85	26.61	73.80	16.72	Conventional	No	No	No	
23	PM6 : $PC_{71}BM$: N3	0.85	25.71	76.60	16.74	Conventional	No	No	No	196
24	PBDB-T-2F : BTP4Cl-12	0.86	25.60	77.60	17.00	Conventional	Yes	No	No	197
25	PM6 : $PC_{71}BM$: Y6	0.84	26.00	78.00	17.00	Conventional	No	No	No	198

26	PM6 : BTP-M : Y6	0.88	26.56	73.46	17.03	Conventional	Yes	No	No	[199]
27	D-18 : Y6	0.86	27.70	76.60	18.22	Conventional	No	No	No	[151]
28	PM6:Y6	0.85	25.89	78.59	17.23	Conventional	No	Yes	No	[149]
29	PM6:MF1:Y6	0.85	25.68	78.61	17.22	Conventional	No	No	No	[200]
30	PM6:IDMIC-4F:Y6	0.86	25.60	74.20	16.40	Inverted	No	No	No	[201]
31	PM6:Y6:Y6-BO:PCBM	0.85	26.67	78.49	17.84	Conventional	No	No	No	[202]

4.2 Experiment

Device Fabrication:

The i-OPV and mi-OPV were fabricated with the structure of ITO/ZnO/PM6:Y6/MoO_3/Ag and ITO/ZnO:EDT/PM6:Y6/MoO_3/Ag, respectively. The c-OPV was fabricated with the structure of ITO/PEDOT:PSS/PM6:Y6/Phen-NaDPO/Al. The ITO substrates were cleaned with acetone and isopropanol (IPA) using ultra-sonication, then dried in the oven at 100 °C for 1 h. The dried ITO substrates were treated with UV for 1 h. The ZnO layer was coated on the UV-treated ITO substrate by spin coating with a 0.75 M ZnO sol-gel solution at 5000 rpm followed by annealing at 200 °C for 10 min. In the mi-OPV, the 1,2-ethanedithiol (EDT) solution (0.5% v/v) in acetonitrile was treated on the ZnO layer by spin coating at 5000 rpm and annealing at 110 °C for 5 min. Then, the EDT-treated ZnO film coated on ITO substrate was moved into a glovebox under a N_2 atmosphere to deposit the PM6:Y6 active layer. For the preparation of the active layer, the PM6:Y6 blend solutions (1:1.2, w/w) in chloroform (16.8 mg/ml) were combined with 0.5% CN (v/v) and stirred for 3 h. The blend solution was spin-coated on the EDT-treated ZnO film at 5000 rpm. The MoO_3 layer was deposited by thermal evaporation onto the active layer with a 6 nm thickness. The Ag electrode was also deposited by thermal evaporation with a 100 nm thickness under a vacuum pressure of < 10^{-6} Torr.

For c-OPV, PEDOT:PSS was spin-coated on the UV-treated ITO substrate at 4000 rpm for 30 s, followed by thermal annealing at 150 °C for 10 min. The PM6:Y6 active layer and electron transport layer, Phen-NaDPO, were deposited under nitrogen in a glove box. While the PM6:Y6 active layer was prepared at a similar condition with the i-OPV, the Phen-NaDPO solution (2 mg/mL) in methanol was coated on top of the active layer at 5000 rpm, followed by thermal annealing at 70 °C for 1 min. The Al electrode was deposited via thermal evaporation under <10^{-6} Torr to obtain a thickness of 100 nm.

Device Characterization:

The current density-voltage (*J-V*) characteristics of OPVs were obtained using a Keithley 2401 source measurement unit under AM 1.5G simulated illumination (100 mW/cm^2). The intensity of simulated sunlight was calibrated using a standard Si-photodiode detector with a KG-3 filter (Newport Co.). The external quantum efficiency (EQE) spectra of OPVs were measured by the IQE-200B (Newport Co.). The surface morphologies of ZnO and EDT treated ZnO film were measured by using an atomic force microscope (AFM, Nanocute, SII Nano Technology Inc.). CE and TPC/TPV measurements were performed using the analyzer function of an organic semiconductor parameter test system (McScience, T4000) at V_{OC} conditions under illumination with a white LED. The frequency-dependent capacitance was measured by means of impedance spectroscopy (Ivium Technologies, Ivium Stat) at zero bias with frequency range from 1 MHz to 1 Hz under dark conditions. Fourier-transform photocurrent spectroscopy (FT-IR) spectra were obtained using a Bruker INVENIO-R spectrometer. FTIR-EQE was measured in an in-house built FTPS setup, which consisted of an INVENIO-R spectrometer, equipped with quartz beam splitter. The photocurrent produced by the PSC under illumination was amplified using a SR570 low-noise preamplifier (Stanford Research System) and fed back into the external detector port of the FT-IR. The Electroluminescence (EL) spectra were obtained using a MAYA2000 PRO spectrophotometer (Ocean Optics).

4.3 Results and discussion

Figures 4.1a and b show the device structures of c-OPV and i-OPV and the chemical structures of PM6 and Y6, respectively. The c-OPV was fabricated with an architecture of indium-doped tin oxide (ITO)/PEDOT:PSS/PM6:Y6/Phen-NaDPO/Al, whereas the i-OPV was constructed with a structure of ITO/ZnO/PM6:Y6/MoO_x/Ag. As shown in the current-density (*J*) - voltage (*V*) characteristics of the devices in **Figure 4.1c**, the c-OPV showed a PCE of 16.74% with a V_{OC} of 0.852 V, a J_{SC} of 27.21 mA/cm^2, and a FF of 0.73, which is consistent with the literature results.[102, 191] In contrast, the i-OPV showed a considerably lower PCE (15.54%) with a V_{OC} of 0.852 V, a J_{SC} of 26.44 mA/cm^2, and a FF of 0.69, which is also consistent with the literature results as shown in **Table 4.1**. Notably, the highest reported PCE of the i-OPV based on PM6:Y6 (including their derivatives), thus far, was 15.70% (and 16.50% in the ternary device with $PC_{71}BM$).[102, 187] In contrast, the c-OPV devices based on the related materials often demonstrated PCEs over 17%.[149, 150] Therefore, the c-OPV architecture was mainly adopted in the research for PM6:Y6 and its derivative systems. **Figure 4.1d** shows the stability of the

PM6:Y6 based devices without encapsulation. For air storage stability, the devices were stored in dark ambient air (humidity of ~15%), and the PCE of the devices was monitored occasionally. For the photostability test, the devices were illuminated continuously at one-sun using a solar simulator based on a light-emitting diode array under N_2 (in a glove box). The PCE of devices was periodically measured under AM 1.5G one-sun illumination (Xenon lamp) (see the experimental section for more details). Under air storage, both devices (c-OPV and i-OPV) showed similarly significant PCE degradation after 300 h. In the photostability test, the i-OPV showed ~73% retention after 300 h of illumination, whereas the c-OPV device retained only 5% of the initial PCE even after 100 h of illumination.

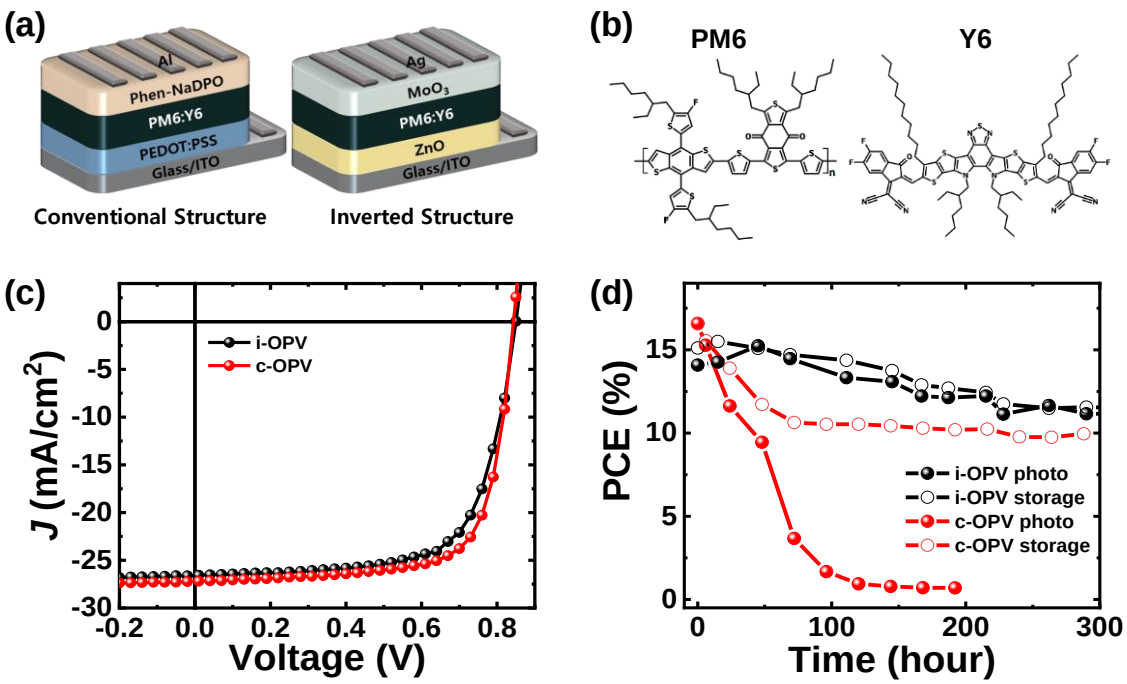

Figure 4.1. Photovoltaic devices and photoactive materials. (a) Device structures of c-OPV and i-OPV. (b) Chemical structures of PM6 and Y6. (c) *J-V* characteristics of the devices, (d) PCE changes of devices with respect to storage and illumination time. For storage stability, the devices were stored under ambient air atmosphere (humidity ~15%), while the photostability was measured by illumination using a light-emitting-diode light source under N_2. All devices were measured without encapsulation.

Apart from our expectations, the stabilities of the i-OPV were not substantially improved compared to those of the c-OPV. To further investigate the stability of i-OPV for a more extended period, storage- and photo- stability were monitored continuously up to 1200 h (**Figure 4.2**). The i-OPV retained ~50% and ~54% of its initial PCE after 1200 h of air storage and illumination, respectively. Fourier-transform infrared spectroscopy (FT-IR) elucidated the mechanism of the degradation process for the i-OPV to determine whether it originated from the chemical changes in the PM6:Y6 photoactive materials. As observed in **Figure 4.3**, there was no change in FT-IR spectra of PM6 and Y6 between fresh and aged (500 h of illumination) samples. Moreover, no particular change in the surface morphology of the PM6:Y6 active layers due to aging was observed in the atomic force microscope (AFM) images (**Figure 4.4**). Therefore, it is presumed that the degradation of the PM6:Y6 based i-OPVs was due to neither chemical nor morphological changes of the active layer.

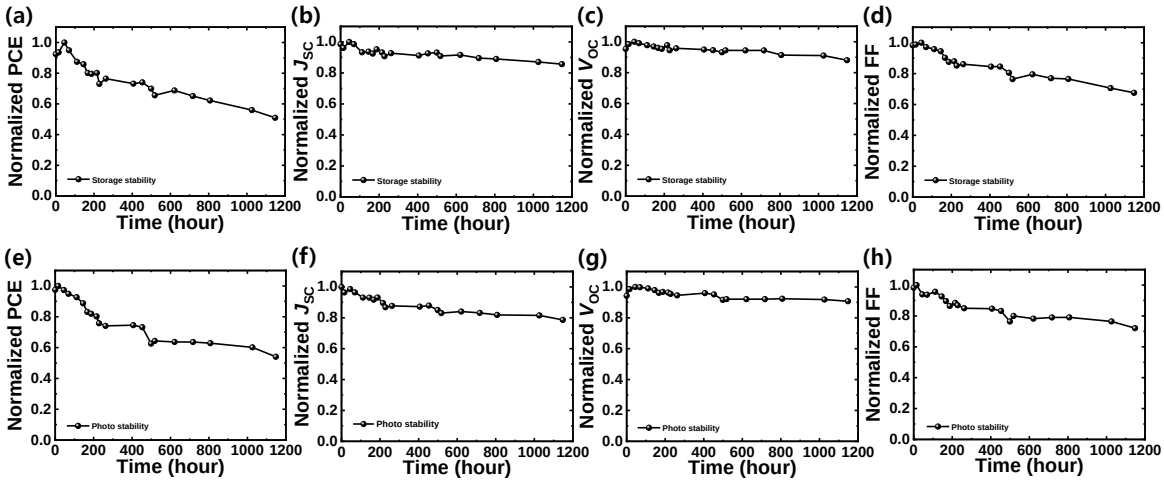

Figure 4.2. Long-term stability of PM6:Y6 based i-OPV. (a-d) Storage stability and (e-h) photostability.

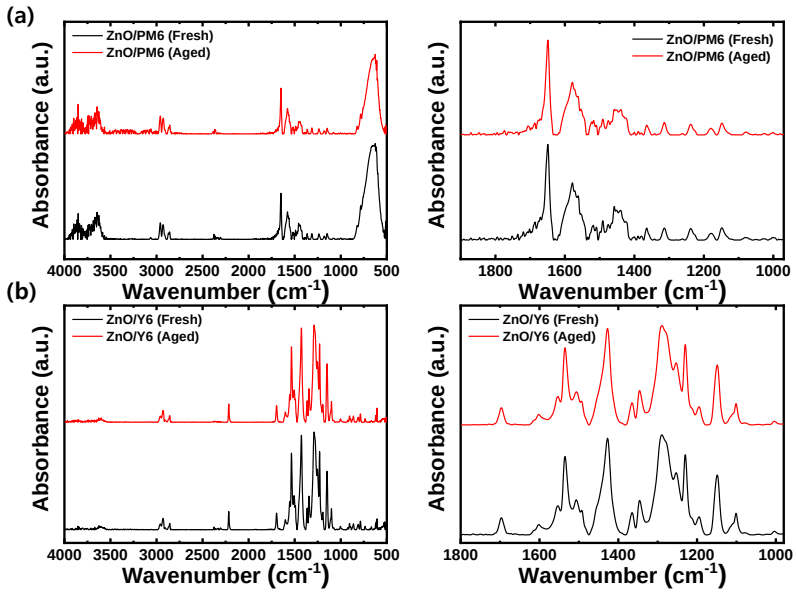

Figure 4.3. Fourier-transform infrared (FT-IR) spectra of the active materials. (a) ZnO/PM6 and (b) ZnO/Y6. Aging was performed by illumination for 500 h.

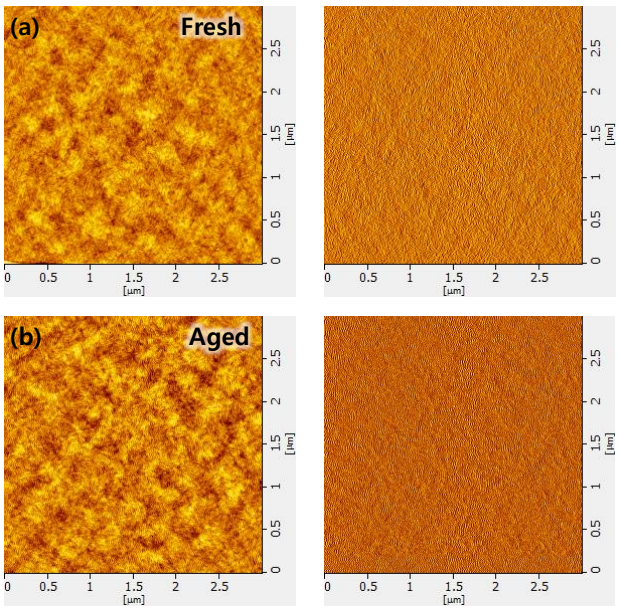

Figure 4.4. Atomic force microscopy (AFM) images of PM6:Y6 films. (a) Fresh sample (left: height image, right phase image) and (b) aged sample (left: height image, right phase image). Aging was carried out by illumination for 500 h.

To further elucidate the origins of degradation, the photocurrent-density (J_{ph}) vs. effective voltage (V_{eff} = V_0 - V) characteristics were analyzed (**Figure 4.5a and Table 4.2**). The extracted charge generation rates (G_{max}) given by $J_{sat} = q \cdot L \cdot G_{max}$ (where q is the elementary charge and L is the thickness of the active layer) were similar for both the fresh i-OPV (1.61×10^{28} $m^{-3}s^{-1}$) and the aged i-OPV by 500 h illumination (1.56×10^{28} $m^{-3}s^{-1}$). However, the charge collection probability (P_C) at the short-circuit condition, which is given by J_{ph}/J_{sat}, of the fresh i-OPV (96.4%) was decreased after aging (93.9%). The lowered P_C indicated reduced charge collection at the short-circuit condition, which is reflected in the device J_{SC} degradation. The charge extraction probability at the maximum power point (MPP) is given as $P_{MPP} = J_{MPP}/J_{sat}$. The P_{MPP} values of the fresh i-OPV and the aged i-OPV were 67.6% and 57.1%, respectively, which is the origin of the decreased FF in the aged i-OPV. The charge recombination property near open-circuit conditions was evaluated by monitoring the device V_{OC} values with respect to light intensity (**Figure 4.5b**). While the aged i-OPV has lower V_{OC} values than that of the fresh sample, the extracted ideality factor (kT/q) was significantly increased from 1.38 kT/q to 2.04 kT/q, which indicates the enhanced trap-assisted recombination. The charge recombination lifetimes (τ_{rec}) of the i-OPV was also determined by fitting the photovoltage decay curves in transient photovoltage (TPV) analysis under open-circuit conditions (**Figure 4.6**). The aged i-OPV device showed a much shorter τ_{rec} (0.39 μs) than the fresh i-OPV device (1.39 μs), confirming the enhanced trap-assisted recombination probability.

The trap density of state (tDOS) of the devices was determined using frequency-dependent capacitance. **Figure 4.5c** shows the distributions of tDOS extracted from the low-frequency regions of **Figure 4.7**, which revealed a higher deep-trap density of the aged i-OPV than the fresh i-OPV. Moreover, the level of the high-frequency plateau of the aged i-OPV, which corresponds to the shallow traps, was also higher than that of fresh i-OPV (**Figure 4.7**). This result indicated that both deep and shallow trap densities were increased by aging i-OPV, which deteriorated the device performance.

To gain more insight on the effects of the traps on the PM6:Y6 active layers by aging, the voltage loss (V_{loss}) change in i-OPV with aging was analyzed using external quantum efficiency (EQE) spectra by Fourier-transform photocurrent spectroscopy (FTPS) and electroluminescence (EL) spectra (**Figures 4.5d and e**). Based on the Shockley-Queisser (SQ) theory,[203, 204] the V_{loss} of OPV device can be defined by three types of losses:

$$V_{loss} = \Delta V_1 + \Delta V_2 + \Delta V_3 = \left(\frac{E_g}{q} - V_{OC}^{SQ}\right) + \left(V_{OC}^{SQ} - V_{OC}^{Rad}\right) + \left(V_{OC}^{Rad} - V_{OC}\right) \quad \text{Equation (4.1)}$$

where E_g is bandgap of device, V_{OC}^{SQ} is maximum V_{OC} by the SQ limit, V_{OC}^{Rad} is V_{OC} in the radiative limit. The ΔV_1 is an unavoidable voltage loss typically in the range of 0.20 – 0.30 V in any solar cell defined by SQ theory. The ΔV_2 is the radiative voltage loss by the effect of radiative recombination and the non-ideal EQE, and the ΔV_3 is the voltage loss due to the non-radiative recombination. The E_g is estimated by calculating the distribution of bandgaps from the photovoltaic EQE.[205] The V_{OC}^{Rad} was derived by the following equation:

$$V_{OC}^{Rad} = \frac{k_B T}{q} ln\left[\frac{J_{SC}}{q\int_{E_g}^{\infty} Q_e(E)\cdot\phi_{BB}(E)dE} + 1\right] \qquad \text{Equation (4.2)}$$

where k_B is Boltzmann constant, T is the temperature, q is electric charge and the term $\phi_{BB}(E)$ is the blackbody spectrum given by:

$$\phi_{BB}(E) = \frac{2\pi E^2}{h^3 c^2} exp\left[-\frac{E}{k_B T}\right] \qquad \text{Equation (4.3)}$$

The $Q_e(E)$ in Eq. (2) was obtained via fitting the fraction of EL emission and blackbody radiation ($\phi_{EL/BB}$) to low energy region of highly-sensitive FTPS-EQE. The total V_{loss} of i-OPVs and the corresponding parameters (i.e., ΔV_1, ΔV_2, and ΔV_3) are summarized in **Table 4.3**.

Notably, a significant increase in radiative voltage loss (ΔV_2) was observed in the aged i-OPV. It is known that the increase in the radiative loss is typically due to the shallow traps located near the band-edge (i.e., singlet state). Many previous studies in the literature confirmed that the penetration of oxygen into the active layer causes the doping of active materials as time goes on, which can increase shallow trap (doping level) density.[206-209] Therefore, the defect-rich interfaces not only resist charge extraction but also influence the energy states of the active layer. In our i-OPV, oxygen-containing defects on the ZnO-ETL can facilitate the formation of shallow traps in the active layer by aging; thus, the V_{OC}^{Rad} was formed at a lower level than V_{OC}^{SQ} due to the energy states of the shallow traps. When the density of the shallow traps increases, radiative decay occurs from the shallow trap level to the HOMO of active materials increased. This was confirmed by the EL emission spectra of the i-OPVs (**Figure 4.5f**). The difference in the EL emission of the two devices was peaked at ~1.44 eV, which is identical with the E_g of Y6. This EL emission near 1.44 eV corresponds to the direct radiative decay from LUMO to HOMO of Y6. In the aged i-OPV, the EL emission near 1.44 eV was reduced because some electrons were transferred into the shallow trap level. Therefore, this decreases in EL emission near 1.44 eV clearly

supports the enhancement of radiative energy loss in aged i-OPV due to the increased shallow trap density.

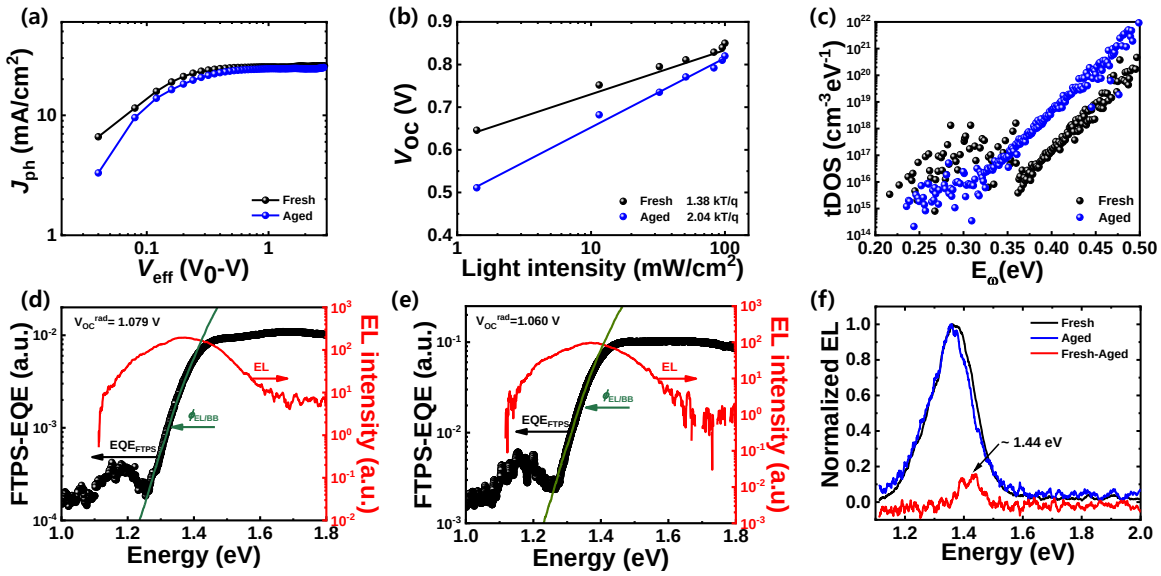

Figure 4.5. Characterizations of i-OPV. (a) J_{ph} vs. V_{eff} curves, (b) V_{OC} as a function of light intensity, (c) distributions of trap density of state (tDOS) from the frequency-dependent capacitance spectra, (d-e) the FTPS-EQE and EL emission spectra of (d) fresh i-OPV and (e) aged i-OPV, and (f) normalized EL spectra of fresh and aged i-OPVs.

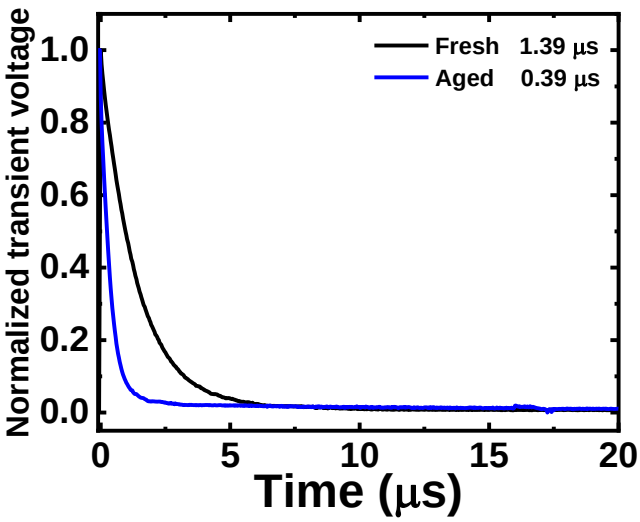

Figure 4.6. TPV analysis under open-circuit conditions of fresh and aged i-OPV.

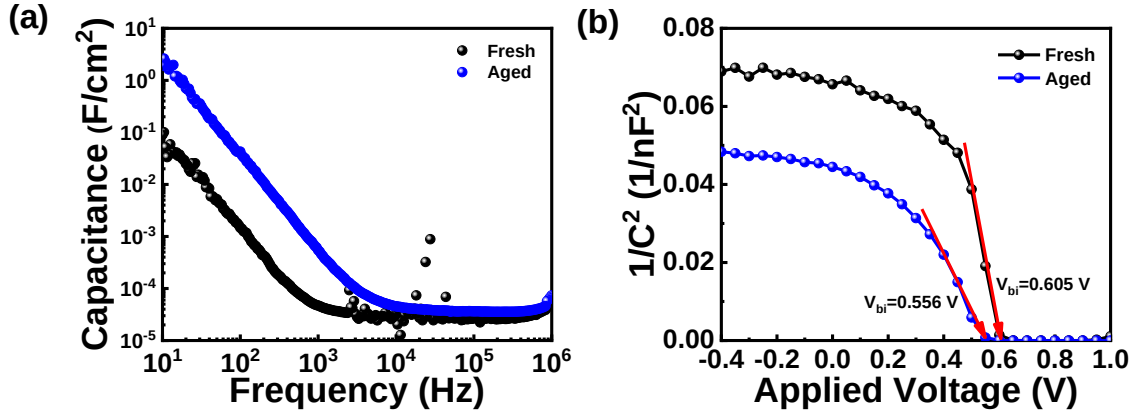

Figure 4.7. (a) Frequency-dependent capacitance spectra and (b) Mott-Schottky plot of i-OPVs.

Table 4.2. Summary of parameters from J_{ph} vs. V_{eff} characterizations.

	G_{max} (m^{-3}s^{-1})	P_C (%)	P_{MPP} (%)
Fresh i-OPV	1.61×10^{28}	96.4	67.6
Aged i-OPV	1.56×10^{28}	93.9	57.1
Fresh mi-OPV	1.73×10^{28}	97.5	79.2
Aged mi-OPV	1.69×10^{28}	95.2	77.3

Table 4.3. Detailed parameters of fresh and aged i-OPVs in V_{loss} analysis. The units of all the parameters are [V].

	E_g	V_{OC}^{SQ}	$\Delta V1$	V_{OC}^{rad}	ΔV_2	V_{OC}	ΔV_3
Fresh i-OPV	1.440	1.198	0.242	1.079	0.119	0.850	0.229
Aged i-OPV	1.440	1.198	0.242	1.060	0.187	0.832	0.228

Based on the long-term stability study of the PM6:Y6 based i-OPVs, we confirmed that the degradation of the device is not attributed to the change in chemical structure or morphology but based on the increase of deep and/or shallow traps originating from the oxygen-related defect sites on ZnO-ETL. Conversely, this provided insight for improvement of the long-term stability and charge extraction of the PM6:Y6 based i-OPV simultaneously. To mitigate the interfacial defects, we selected a chemical modifier, EDT, because of its efficient defect passivation by forming zinc-ethanedithiolates as reported in organic, quantum dot, and perovskite solar cells.[31-33] The modification by EDT was carried out by spin-coating the EDT solution on the pristine ZnO layer followed by thermal treatment at 110 °C for 5 min. As shown in **Figure 4.8a** and **Table 4.4**, the chemically modified i-OPV (mi-OPV) showed substantially improved PCE (17.42%) and FF (0.76) compared to unmodified i-OPV (PCE =15.54% and FF = 0.69). The EQE of mi-OPV was significantly higher than that of the pristine i-OPV in entire wavelengths indicating improved charge collection efficiency (**Figure 4.8b**). The calculated J_{SC} value of mi-OPV from the integration of the EQE curve was 26.169 mA cm^{-2}, which is consistent with that of the *J-V* characteristic (27.845 mA cm^{-2}), confirming the validity of our measurement. The statistical analysis results of the device PCE are shown in **Figure 4.9**. Notably, the PCE of mi-OPV was the highest among the reported PM6:Y6 based i-OPVs (**Table 4.1**) and even comparable (or slightly better) to the state-of-the-art c-OPV counterparts. We attribute the record-high PCE of our mi-OPV to the excellent charge collection property by suppressing interfacial defects.

As shown in **Figure 4.8c and Table 4.2**, the G_{max} values of i-OPV and mi-OPV were almost identical, indicating similar charge generation rates in the two devices. However, the *P*c and P_{MPP} values of mi-OPV (97.5% and 79.2%) were considerably higher than those of i-OPV (96.4% and 67.6%). Since the PM6:Y6 active layer with identical thickness was used in both devices, the improved *P*c and P_{MPP} values of the mi-OPV are possibly owing to the reduced charge recombination. In the J_{SC} vs. light intensity plots (**Figure 4.8d, Figure 4.10, Table 4.5 and 4.6**), the fitted α value of both devices approached unity, indicating near freedom from bimolecular recombination loss. The substantially lower ideality factor of mi-OPV (1.14 kT/q) compared to i-OPV (1.38 kT/q), obtained from the plot of V_{OC} values with respect to light intensity, confirmed the reduction in trap-assisted recombination (**Figure 4.8e, Figure 4.10, Table 4.5 and 4.6**). This lower trap-assisted interfacial recombination was confirmed by charge extraction (CE) measurement (**Figure 4.11**). The mi-OPV showed significantly enhanced charge extraction density compared to that of the i-OPV (**Figure 4.8f**).

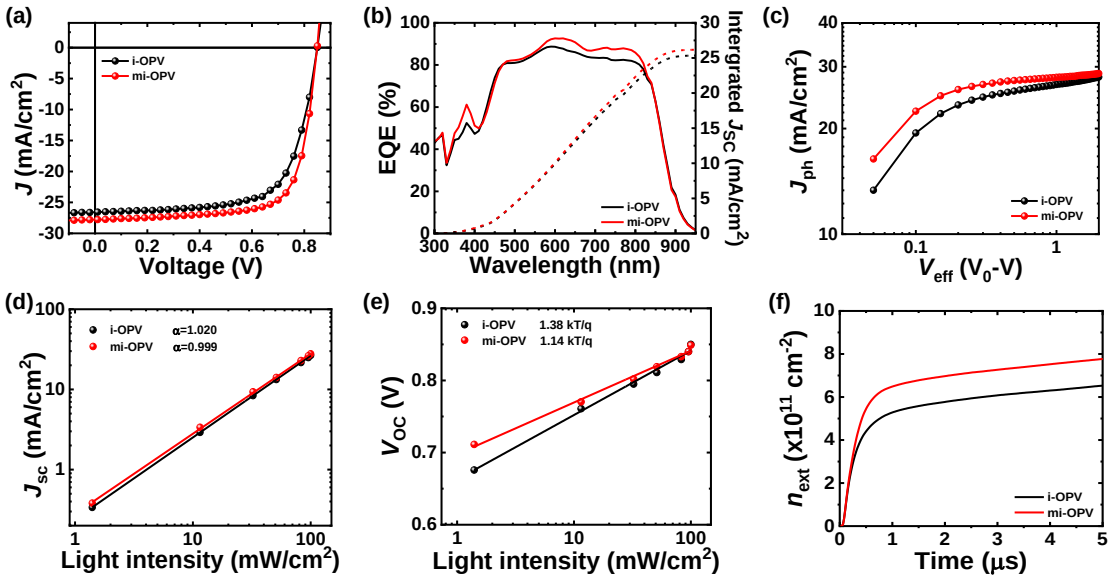

Figure 4.8. Photovoltaic performance of mi-OPV. (a) *J-V* characteristics, (b) external quantum efficiency (EQE), (c) J_{ph} vs. V_{eff} plot, (d) J_{SC} as a function of light intensity, (e) V_{OC} as a function of light intensity, and (f) extracted charge density (n_{ext}) from charge extraction measurement.

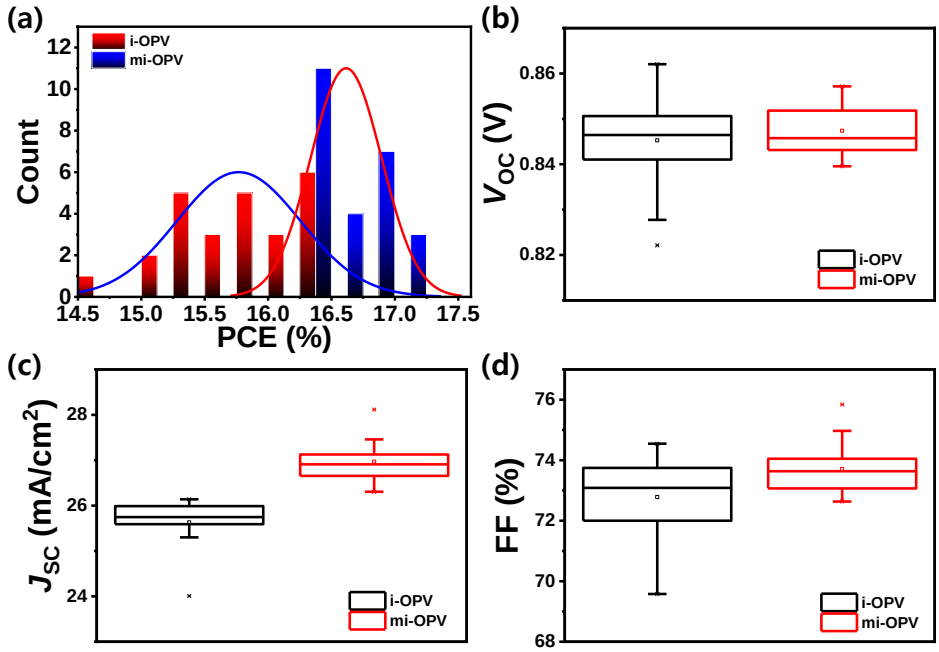

Figure 4.9. The statistical performance distribution of i-OPV and mi-OPV. (a) PCE, (b) V_{OC}, (c) J_{SC} and (d) FF.

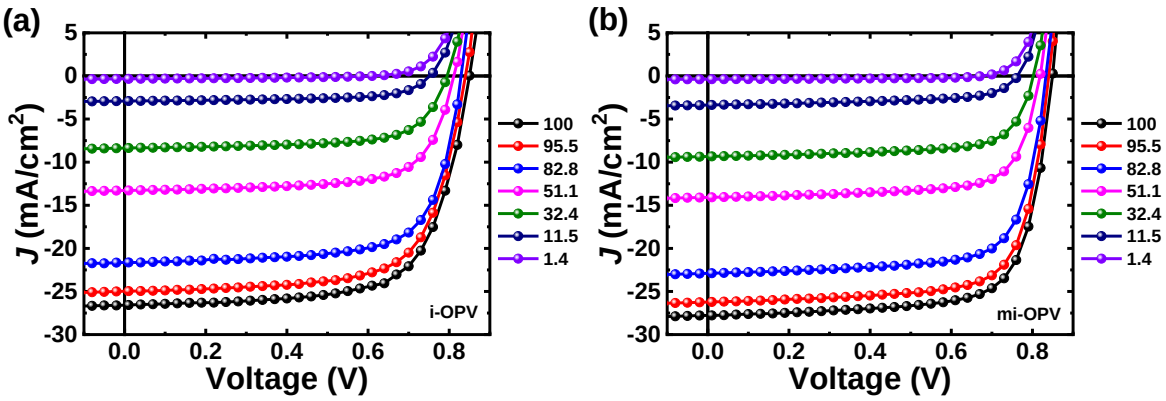

Figure 4.10. *J-V* characteristics at different light intensities of i-OPV and mi-OPV.

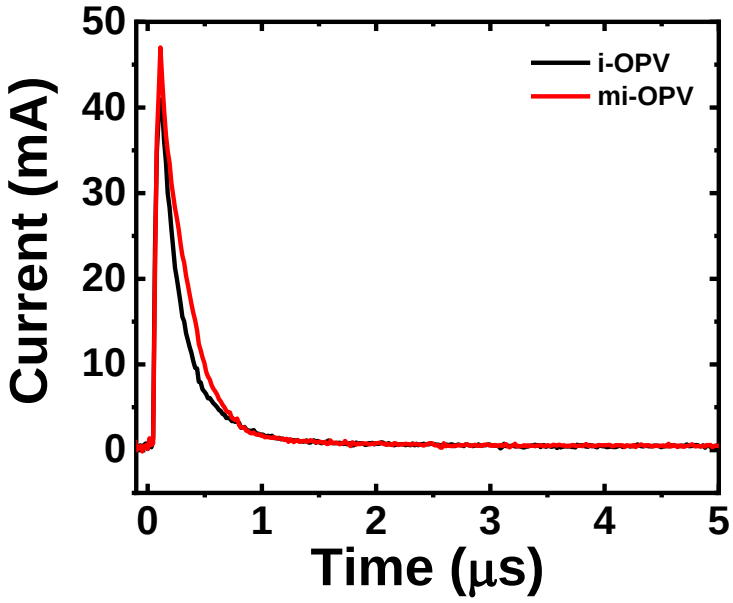

Figure 4.11. Charge extraction measurement of i-OPV and mi-OPV.

Table 4.4. Summary of photovoltaic parameters of i-OPVs.

	V_{OC} (V)	J_{SC} (mA cm^{-2})	FF	PCE (%)	J_{SC}^{EQE} (mA cm^{-2})
i-OPV	0.852	26.443	0.690	15.54	25.345
mi-OPV	0.856	27.845	0.760	17.42	26.169

Table 4.5. Photovoltaic parameters of i-OPV J-V at different light intensities.

Light intensity	J_{SC} (mA/cm^2)	V_{OC}	FF	Efficiency (%)
100	26.5	0.850	0.684	15.5
95.5	24.9	0.840	0.690	14.9
82.8	21.6	0.829	0.709	12.7
51.1	13.2	0.811	0.700	7.55
32.4	8.37	0.795	0.690	4.59
11.5	2.91	0.752	0.655	1.44
1.4	0.339	0.611	0.374	0.0776

Table 4.6. Photovoltaic parameters of mi-PSC *J-V* at different light intensities.

Light intensity	J_{SC} (mA/cm^2)	V_{OC}	FF	Efficiency (%)
100	27.7	0.849	0.731	17.2
95.5	26.2	0.840	0.735	16.2
82.8	22.9	0.833	0.734	14.0
51.1	14.1	0.819	0.725	8.36
32.4	9.34	0.802	0.709	5.31
11.5	3.37	0.763	0.608	1.57
1.4	0.382	0.676	0.523	0.136

Finally, we investigated the effects of trap passivation on the long-term stability (~1200 h) of i-OPVs. **Figure 4.12** shows the storage- and photostability of i-OPV and mi-OPV without encapsulation. The stability of mi-OPV was remarkably higher than the pristine i-OPV. The mi-OPV retained ~95% and ~90% of its original PCE after 500 h and 1200 h of storage in air, respectively, whereas the i-OPV retained only ~70% and ~50% of its PCE (**Figure 4.12a**). In photostability, the PCE of mi-OPV was retained ~90% and ~80% after illumination of 500 h and 1200 h, which is significantly higher than that of i-OPV (~50% retention after 1200 h), as shown in **Figure 4.12e**. Notably, we claim that the mi-OPV in this report has a notably high PCE and stability compared to the previously reported i-OPVs in the literature.

Because the air-storage stability of the mi-OPV was excellent until 1200 h (**Figure 4.12a**), we focused on the degradation of mi-OPV under long-term illumination for further investigation. The degradation of the mi-OPV became apparent in J_{SC} and FF (relatively more minor in V_{OC}). **Figure 4.13a** shows the J_{ph}-V_{eff} characteristics of mi-OPVs, and the extracted G_{max} and *P*c values are listed in **Table 4.2**. After 500 h of illumination, the *P*c value of mi-OPV was reduced from 97.5% to 95.2%, while the G_{max} was similar. Meanwhile, the P_{MPP} values were also not decreased considerably (79.2% vs. 77.3%), which is consistent with the change in FF. From the V_{OC} changes with respect to light intensity (**Figure 4.13b**),

the 500 h illuminated mi-OPV showed a similar ideality factor (1.19 kT/q) to the pristine mi-OPV (1.14 kT/q), which is consistent with the marginal degradation in V_{OC}. **Figure 4.13c** shows the distributions of tDOS of the mi-OPV, determined using frequency-dependent capacitance. The increase in the deep-trap density of mi-OPV after aging under illumination was less than that of the pristine i-OPV (see **Figure 4.5c**). The level of the high-frequency plateau, corresponding to the shallow traps, was not noticeably changed in the mi-OPV (**Figure 4.14**). This result indicated the effective passivation of deep and shallow traps is responsible for the improved long-term stability of mi-OPV. Furthermore, the V_{loss} analysis of the mi-OPVs also showed that the ΔV_2, typically due to the shallow traps, was not changed in the aged mi-OPV (**Figures 4.13d, 4.13e, and Table 4.7**). In addition, no appreciable difference was observed between the EL emission spectra of the aged mi-OPV and the fresh mi-OPV (**Figure 4.13f**). As discussed in the case of i-OPV, if the shallow traps formed by aging, the EL intensity around 1.44 eV, which is the bandgap of Y6, would be altered. No change in the EL emission of the aged mi-OPV at ~1.44 eV supported that the passivation of the penetrative interfacial defects suppressed the formation of shallow traps in the active layer.

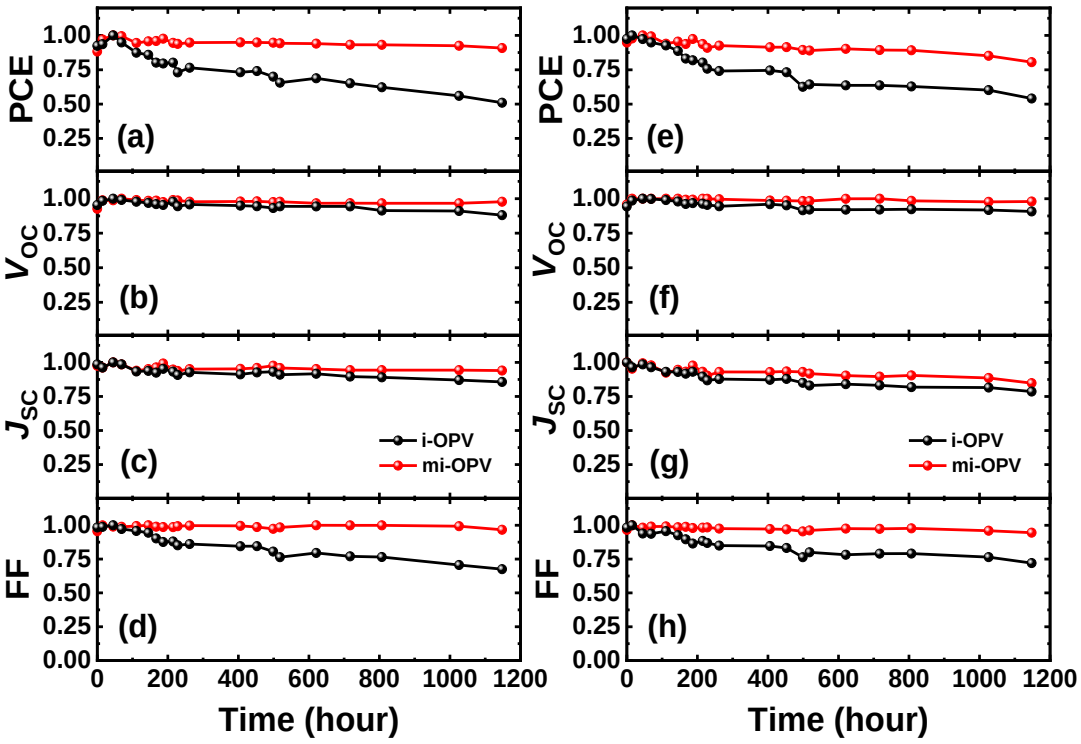

Figure 4.12. Long-term stability of i-OPV and mi-OPV. (a-d) Storage stability and (e-h) photostability. The device parameters are normalized values.

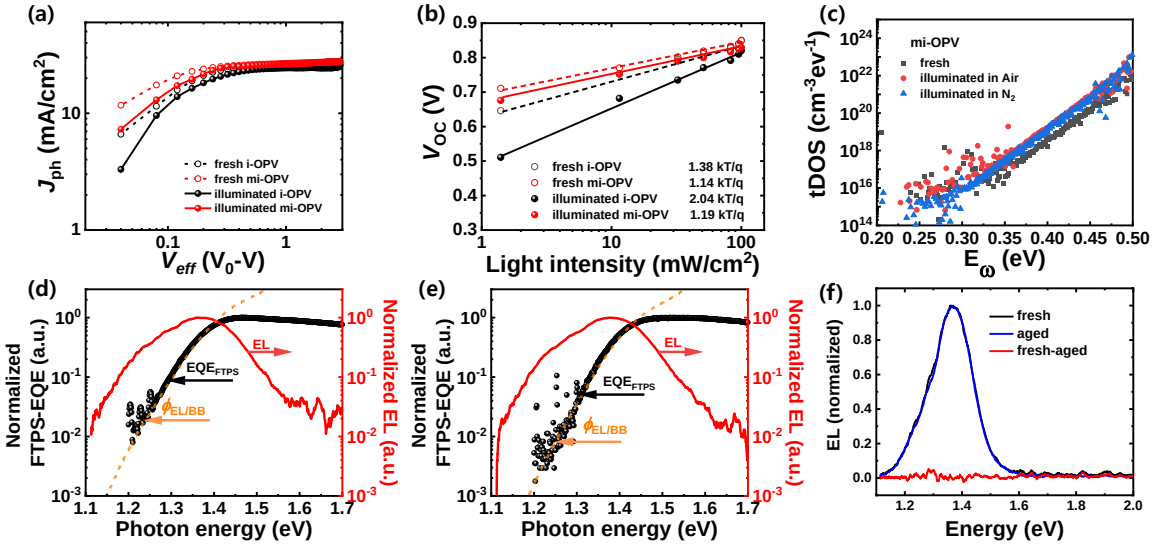

Figure 4.13. Characterizations of mi-OPVs. (a) J_{ph} vs. V_{eff} curves, (b) V_{OC} as a function of light intensity, (c) distributions of trap density of state (tDOS) from the frequency-dependent capacitance spectra, (d-e) the FTPS-EQE and EL emission spectra of (d) fresh mi-OPV and (e) aged mi-OPV, and (f) normalized EL spectra of fresh and aged mi-OPVs.

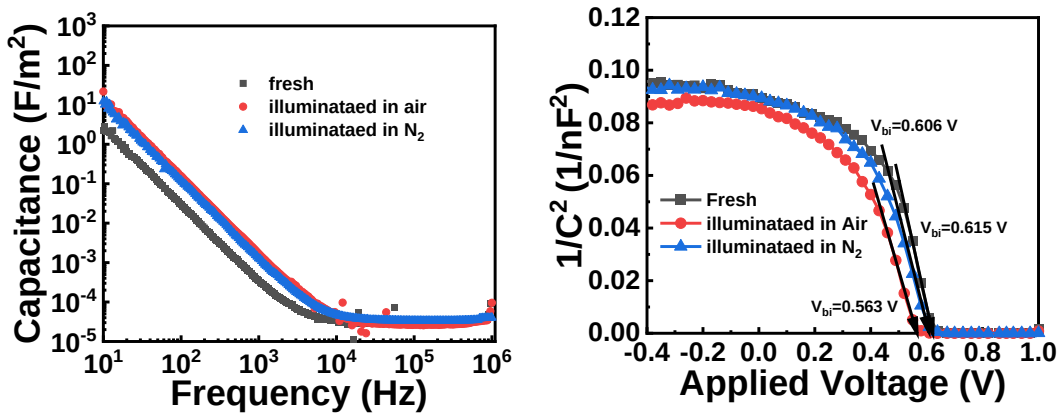

Figure 4.14. (a) Frequency-dependent capacitance spectra and (b) Mott-Schottky plot of mi-OPV.

Table 4.7. Detailed parameters of fresh and aged mi-OPVs in V_{loss} analysis. The units of all the parameters are [V].

	E_{g}	V_{OC}^{SQ}	$\Delta V1$	V_{OC}^{rad}	ΔV_2	V_{OC}	ΔV_3
fresh mi-OPV	1.428	1.188	0.240	1.134	0.054	0.852	0.282
aged mi-OPV	1.428	1.188	0.240	1.142	0.046	0.849	0.293

4.4 Conclusion

The long-term stable PM6:Y6 based i-OPV with PCE comparable to state-of-the-art c-OPV was developed. The origins of the deteriorated PCE and long-term stability of the reported PM6:Y6 based i-OPV, deep and shallow traps at the ETL/PM6:Y6 interface and within the PM6:Y6 active layer, were investigated and resolved. The interfacial defects increased deep trap density in the i-OPV to reduce charge extraction efficiency by trap-assisted recombination. Furthermore, the penetrative oxygen-containing defects generated shallow traps in the PM6:Y6 active layer by aging, which also causes an additional V_{loss}. The suppression of these interfacial defects by a chemical modification effectively improved the charge collection efficiency of the i-OPV. The mi-OPV achieved a PCE of 17.43%, which is the highest PCE among the reported i-OPV devices. Moreover, the long-term stability of the mi-OPV was significantly improved by the suppression of the formation of deep and shallow traps. After 1200 h of air storage and illumination, the mi-OPV retained ~90% and ~80% of its initial PCE, whereas the pristine i-OPV only retained ~50% and 54%, respectively.

Chapter 5. Summary

In order to enhance the performance of the organic solar cells, adjusting the morphology of photoactive layer and eliminating the trap states is essential. Therefore, in this study, various strategies of ternary blend, solid-solvent hybrid additive method, and interfacial treatment are applied to device.

In chapter 1, the fundamental contents in which working principle and characterization as well as strategies to improve the performance of OSCs are described.

In chapter 2, the fullerene acceptor, which has historically been used in bulk-heterojunction (BHJ) organic solar cells, is being replaced by non-fullerene acceptors due to its problem of high energy loss (E_{loss}). To reduce the energy loss in BHJ organic solar cells as a means to improve open-circuit voltage (V_{OC}), several approaches have been applied to diminish recombination loss, notably enhancements to film morphology and decreasing of trap states by improving the crystallinity of active components. However, the adjustment of trap density by means of morphology control only has an inevitable limit. In this work, we have investigated the use of a ternary configuration as an alternative way to mitigate the energy loss in fullerene-based BHJ solar cells. A ternary system based on the wide-band-gap polymer PBDTTPD-HT, the small molecule DRCN5T, and $PC_{71}BM$ showed cascading charge transfer from PBDTTPD-HT through DRCN5T to $PC_{71}BM$, an indirect electron transfer that avoided the deep charge transfer state between PBDTTPD-HT and $PC_{71}BM$. DRCN5T:$PC_{71}BM$ mixture has a high E_{CT} level close to the singlet state energy of DRCN5T, leading to low energy loss between DRCN5T and $PC_{71}BM$ and thereby greatly reducing the probability of first-order recombination. Consequently, the incorporation of a small amount of DRCN5T as a secondary donor into the PBDTTPD-HT:$PC_{71}BM$ system enhanced overall PCE, an effect mostly attributed to enhancement of V_{OC} by means of eliminating charge transfer energy losses.

In chapter 3, most organic solar cells based on a bulk heterojunction type active layer are fabricated with the assistance of high boiling point solvent additives to optimize the phase separation of the donor and acceptor. The macroscopic phase separation can be controlled by this solvent additive. However, the control of the microscopic morphology (e.g., π-π stacking, orientation) of the inside phase is still dependent on the interaction energy and self-assembly characteristics of each donor and acceptor. In this work, we introduce a solid-solvent hybrid additive method on PM6:Y6 solar cells to optimize both the macroscopic donor-acceptor phase separation and the microscopic morphology at the same time. For the solvent additive, the well-known 1-CN solvent additive was used to optimize the macroscopic donor-acceptor phase separation. For the solid additive, newly synthesized 3D star-shaped solid additives (Star-A and Star-F), which were delicately designed to achieve adequate electrical properties,

electrostatic potential, and geometrical structure, were used to further optimize the microscopic morphology. Grazing-incidence small-angle X-ray scattering (GISAXS) and grazing-incidence wide-angle X-ray scattering (GIWAXS) measurements showed that the star additives not only induce the dense and enhanced microscopic intermolecular π-π stacking within the phase, but also further optimize the phase separation. By applying the hybrid additive method, enhanced PM6:Y6 solar cells were achieved with only 1% addition of the star-series solid additives.

In chapter 4, we developed the PM6:Y6 based inverted structure organic photovoltaic (i-OPV) with improved power conversion efficiency (PCE) and long-term stability by resolving the origins of performance deterioration in the reported i-OPVs. The deep defects between the metal oxide-based electron-transport layer and PM6:Y6 bulk-heterojunction photoactive layer interface were responsible for the suboptimal PCE and facilitated degradation of the i-OPVs. While the density of the deep traps is increased during the storage of i-OPV, the penetrative oxygen-containing defects additionally generated shallow traps below the band-edge of Y6, causing an additional loss in the open-circuit voltage. The suppression of interfacial defects by chemical modification effectively improved the PCE and long-term stability of i-OPV. The modified i-OPV (mi-OPV) achieved a PCE of 17.42%, which is the highest value among the reported PM6:Y6 based i-OPV devices. Moreover, the long-term stability was significantly improved: ~90% and ~80% retention of its initial PCE after 1200 h of air storage and illumination, respectively.

References

1. Best Research-Cell Efficiency Chart (NREL), https://www.nrel.gov/pv/cell-efficiency.html).
2. C. W. Tang, *Appl. Phys. Lett.*, 1986, **48**, 183-185.
3. N. S. Sariciftci, L. Smilowitz, A. J. Heeger and F. Wudl, *Science*, 1992, **258**, 1474-1476.
4. G. Yu, J. Gao, J. C. Hummelen, F. Wudl and A. J. Heeger, *Science*, 1995, **270**, 1789-1791.
5. G. Li, V. Shrotriya, J. S. Huang, Y. Yao, T. Moriarty, K. Emery and Y. Yang, *Nat. Mater.*, 2005, **4**, 864-868.
6. J. Y. Kim, K. Lee, N. E. Coates, D. Moses, T. Q. Nguyen, M. Dante and A. J. Heeger, *Science*, 2007, **317**, 222-225.
7. Y. Lin, J. Wang, Z. G. Zhang, H. Bai, Y. Li, D. Zhu and X. Zhan, *Adv. Mater.*, 2015, **27**, 1170-1174.
8. Z. Xiao, X. Jia and L. Ding, *Sci. Bull.*, 2017, **62**, 1562-1564.
9. M. Zhang, L. Zhu, G. Zhou, T. Hao, C. Qiu, Z. Zhao, Q. Hu, B. W. Larson, H. Zhu, Z. Ma, Z. Tang, W. Feng, Y. Zhang, T. P. Russell and F. Liu, *Nat Commun*, 2021, **12**, 309.
10. P. Heremans, D. Cheyns and B. P. Rand, *Acc. Chem. Res.*, 2009, **42**, 1740-1747.
11. J. L. Bredas, J. E. Norton, J. Cornil and V. Coropceanu, *Acc. Chem. Res.*, 2009, **42**, 1691-1699.
12. S. H. Bae, H. X. Zhao, Y. T. Hsieh, L. J. Zuo, N. De Marco, Y. S. Rim, G. Li and Y. Yang, *Chem*, 2016, **1**, 197-219.
13. A. Gusain, R. M. Faria and P. B. Miranda, *Front Chem*, 2019, **7**, 61.
14. J. D. Servaites, M. A. Ratner and T. J. Marks, *Energy Environ. Sci.*, 2011, **4**, 4410-4422.
15. J. Z. Yao, T. Kirchartz, M. S. Vezie, M. A. Faist, W. Gong, Z. C. He, H. B. Wu, J. Troughton, T. Watson, D. Bryant and J. Nelson, *Phys. Rev. Appl.*, 2015, **4**, 014020.
16. N. K. Elumalai and A. Uddin, *Energy Environ. Sci.*, 2016, **9**, 391-410.
17. W. Li, K. H. Hendriks, A. Furlan, M. M. Wienk and R. A. Janssen, *J. Am. Chem. Soc.*, 2015, **137**, 2231-2234.
18. J. Benduhn, K. Tvingstedt, F. Piersimoni, S. Ullbrich, Y. L. Fan, M. Tropiano, K. A. McGarry, O. Zeika, M. K. Riede, C. J. Douglas, S. Barlow, S. R. Marder, D. Neher, D. Spoltore and K. Vandewal, *Nat. Energy*, 2017, **2**, 17053.
19. B. Qi and J. Wang, *Phys. Chem. Chem. Phys.*, 2013, **15**, 8972-8982.
20. B. Xiao, P. Calado, R. C. I. MacKenzie, T. Kirchartz, J. Yan and J. Nelson, *Phys. Rev. Appl.*, 2020, **14**.
21. N. Gasparini, A. Salleo, I. McCulloch and D. Baran, *Nat. Rev. Mater.*, 2019, **4**, 229-242.
22. J. Lee, S. M. Lee, S. Chen, T. Kumari, S. H. Kang, Y. Cho and C. Yang, *Adv. Mater.*, 2019, **31**,

1804762.
23. R. N. Yu, H. F. Yao and J. H. Hou, *Adv. Energy Mater.*, 2018, **8**, 1702814.
24. M. Koppe, H.-J. Egelhaaf, G. Dennler, M. C. Scharber, C. J. Brabec, P. Schilinsky and C. N. Hoth, *Adv. Funct. Mater.*, 2010, **20**, 338-346.
25. S. Li, Y. Sun, B. Zhou, Q. Fu, L. Meng, Y. Yang, J. Wang, Z. Yao, X. Wan and Y. Chen, *ACS Appl. Mater. Interfaces*, 2021, **13**, 40766-40777.
26. J. Huang and H. Yu, *ACS Appl. Mater. Interfaces*, 2021, **13**, 46927-46937.
27. Q. Liu, Y. Wang, J. Fang, H. Liu, L. Zhu, X. Guo, M. Gao, Z. Tang, L. Ye, F. Liu, M. Zhang and Y. Li, *Nano Energy*, 2021, **85**, 105963.
28. P. Bi, S. Zhang, Z. Chen, Y. Xu, Y. Cui, T. Zhang, J. Ren, J. Qin, L. Hong, X. Hao and J. Hou, *Joule*, 2021, **5**, 2408-2419.
29. O. V. Mikhnenko, H. Azimi, M. Scharber, M. Morana, P. W. M. Blom and M. A. Loi, *Energy Environ. Sci.*, 2012, **5**, 6960-6965.
30. J. K. Lee, W. L. Ma, C. J. Brabec, J. Yuen, J. S. Moon, J. Y. Kim, K. Lee, G. C. Bazan and A. J. Heeger, *J. Am. Chem. Soc.*, 2008, **130**, 3619-3623.
31. J. Zhao, S. Zhao, Z. Xu, B. Qiao, D. Huang, L. Zhao, Y. Li, Y. Zhu and P. Wang, *ACS Appl. Mater. Interfaces*, 2016, **8**, 18231-18237.
32. D. Yang, F. C. Lohrer, V. Korstgens, A. Schreiber, S. Bernstorff, J. M. Buriak and P. Muller-Buschbaum, *ACS Energy Lett.*, 2019, **4**, 464-470.
33. B. J. Tremolet de Villers, K. A. O'Hara, D. P. Ostrowski, P. H. Biddle, S. E. Shaheen, M. L. Chabinyc, D. C. Olson and N. Kopidakis, *Chemistry of Materials*, 2016, **28**, 876-884.
34. R. Yu, H. Yao, L. Hong, Y. Qin, J. Zhu, Y. Cui, S. Li and J. Hou, *Nat. Commun.*, 2018, **9**, 4645.
35. R. Yu, H. Yao, Z. Chen, J. Xin, L. Hong, Y. Xu, Y. Zu, W. Ma and J. Hou, *Adv. Mater.*, 2019, **31**, 1900477.
36. L. Liu, Y. Kan, K. Gao, J. Wang, M. Zhao, H. Chen, C. Zhao, T. Jiu, A. K. Jen and Y. Li, *Adv. Mater.*, 2020, **32**, 1907604.
37. P. Fan, W. Sun, X. Zhang, Y. Wu, Q. Hu, Q. Zhang, J. Yu and T. P. Russell, *Adv. Funct. Mater.*, 2020, **31**.
38. D. He, F. Zhao, J. Xin, J. J. Rech, Z. Wei, W. Ma, W. You, B. Li, L. Jiang and Y. Li, *Adv. Energy Mater.*, 2018, **8**, 1802050.
39. A. J. Parnell, A. J. Cadby, A. D. F. Dunbar, G. L. Roberts, A. Plumridge, R. M. Dalgliesh, M. W. A. Skoda and R. A. L. Jones, *J. Polym. Sci., Part B: Polym. Phys.*, 2016, **54**, 141-146.
40. C. H. Peters, I. T. Sachs-Quintana, W. R. Mateker, T. Heumueller, J. Rivnay, R. Noriega, Z. M. Beiley, E. T. Hoke, A. Salleo and M. D. McGehee, *Adv. Mater.*, 2012, **24**, 663-668.

41. T. M. Clarke, C. Lungenschmied, J. Peet, N. Drolet, K. Sunahara, A. Furube and A. J. Mozer, *Adv. Energy Mater.*, 2013, **3**, 1473-1483.
42. S. X. Li, W. Q. Liu, M. M. Shi, J. Q. Mai, T. K. Lau, J. H. Wan, X. H. Lu, C. Z. Li and H. Z. Chen, *Energy Environ. Sci.*, 2016, **9**, 604-610.
43. Y. Y. Jiang, L. L. Sun, F. Y. Jiang, C. Xie, L. Hu, X. Y. Dong, F. Qin, T. F. Liu, L. Hu, X. S. Jiang and Y. H. Zhou, *Mater. Horizons*, 2019, **6**, 1438-1443.
44. Y. W. Wang, W. X. Lan, N. Li, Z. J. Lan, Z. Li, J. N. Jia and F. R. Zhu, *Adv. Energy Mater.*, 2019, **9**, 1900157.
45. O. Inganas, *Adv. Mater.*, 2018, **30**, 1800388.
46. G. Li, R. Zhu and Y. Yang, *Nat. Photonics*, 2012, **6**, 153.
47. D. Dang, D. Yu and E. Wang, *Adv. Mater.*, 2019, **31**, 1807019.
48. N. Li, I. McCulloch and C. J. Brabec, *Energy Environ. Sci.*, 2018, **11**, 1355-1361.
49. X. Y. Du, T. Heumueller, W. Gruber, A. Classen, T. Unruh, N. Li and C. J. Brabec, *Joule*, 2019, **3**, 215-226.
50. E. M. Speller, A. J. Clarke, J. Luke, H. K. H. Lee, J. R. Durrant, N. Li, T. Wang, H. C. Wong, J. S. Kim, W. C. Tsoi and Z. Li, *J. Mater. Chem. A*, 2019, **7**, 23361-23377.
51. J. Hou, O. Inganas, R. H. Friend and F. Gao, *Nat Mater*, 2018, **17**, 119-128.
52. Z. Luo, H. Bin, T. Liu, Z. G. Zhang, Y. Yang, C. Zhong, B. Qiu, G. Li, W. Gao, D. Xie, K. Wu, Y. Sun, F. Liu, Y. Li and C. Yang, *Adv. Mater.*, 2018, **30**, 1706124.
53. S. Dai, T. Li, W. Wang, Y. Xiao, T. K. Lau, Z. Li, K. Liu, X. Lu and X. Zhan, *Adv. Mater.*, 2018, **30**, 1706571.
54. W. Li, Z. Xiao, J. L. Cai, J. A. Smith, E. L. K. Spooner, R. C. Kilbride, O. S. Game, X. Y. Meng, D. H. Li, H. J. Zhang, M. X. Chen, R. S. Gurney, D. Liu, R. A. L. Jones, D. G. Lidzey, L. M. Ding and T. Wang, *Nano Energy*, 2019, **61**, 318-326.
55. J. N. Song, M. Zhang, M. Yuan, Y. H. Qian, Y. M. Sun and F. Liu, *Small Methods*, 2018, **2**, 1700229.
56. F. W. Zhao, C. R. Wang and X. W. Zhan, *Adv. Energy Mater.*, 2018, **8**, 1703147.
57. S. Park, M. J. Cha, J. H. Seo, J. Heo, D. Chan Lim and S. Cho, *ACS Appl. Mater. Interfaces*, 2018, **10**, 41578-41585.
58. S. Nho, G. Baek, S. Park, B. R. Lee, M. J. Cha, D. C. Lim, J. H. Seo, S. H. Oh, M. H. Song and S. Cho, *Energy Environ. Sci.*, 2016, **9**, 240-246.
59. J. J. M. Halls, C. A. Walsh, N. C. Greenham, E. A. Marseglia, R. H. Friend, S. C. Moratti and A. B. Holmes, *Nature*, 1995, **376**, 498-500.
60. S. H. Liao, H. J. Jhuo, P. N. Yeh, Y. S. Cheng, Y. L. Li, Y. H. Lee, S. Sharma and S. A. Chen,

Sci. Rep., 2015, **4**, 6813.

61. D. Veldman, S. C. J. Meskers and R. A. J. Janssen, *Adv. Funct. Mater.*, 2009, **19**, 1939-1948.
62. M. C. Scharber, *Adv. Mater.*, 2016, **28**, 1994-2001.
63. T. M. Burke, S. Sweetnam, K. Vandewal and M. D. McGehee, *Adv. Energy Mater.*, 2015, **5**, 1500123.
64. L. Liu, Y. Kan, K. Gao, J. Wang, M. Zhao, H. Chen, C. Zhao, T. Jiu, A. K. Y. Jen and Y. Li, *Adv. Mater.*, 2020, **32**, 1907604.
65. X. Xu, K. Feng, Z. Bi, W. Ma, G. Zhang and Q. Peng, *Adv. Mater.*, 2019, **31**, 1901872.
66. H. Sun, T. Liu, J. Yu, T. K. Lau, G. Zhang, Y. Zhang, M. Su, Y. Tang, R. Ma, B. Liu, J. Liang, K. Feng, X. Lu, X. Guo, F. Gao and H. Yan, *Energy Environ. Sci.*, 2019, **12**, 3328.
67. K. Vandewal, K. Tvingstedt, A. Gadisa, O. Inganas and J. V. Manca, *Nat Mater*, 2009, **8**, 904-909.
68. E. T. Hoke, K. Vandewal, J. A. Bartelt, W. R. Mateker, J. D. Douglas, R. Noriega, K. R. Graham, J. M. J. Frechet, A. Salleo and M. D. McGehee, *Adv. Energy Mater.*, 2013, **3**, 220-230.
69. D. Baran, T. Kirchartz, S. Wheeler, S. Dimitrov, M. Abdelsamie, J. Gorman, R. S. Ashraf, S. Holliday, A. Wadsworth, N. Gasparini, P. Kaienburg, H. Yan, A. Amassian, C. J. Brabec, J. R. Durrant and I. McCulloch, *Energy Environ. Sci.*, 2016, **9**, 3783-3793.
70. L. Y. Zhu, Y. P. Yi and Z. X. Wei, *J. Phys. Chem. C*, 2018, **122**, 22309-22316.
71. X. Liu, Y. X. Li, K. Ding and S. Forrest, *Phys. Rev. Appl.*, 2019, **11**, 024060.
72. F. D. Eisner, M. Azzouzi, Z. Fei, X. Hou, T. D. Anthopoulos, T. J. S. Dennis, M. Heeney and J. Nelson, *J. Am. Chem. Soc.*, 2019, **141**, 6362-6374.
73. L. P. Duan, N. K. Elumalai, Y. Zhang and A. Uddin, *Sol. Energy Mater. Sol. Cells*, 2019, **193**, 22-65.
74. N. Y. Doumon, M. V. Dryzhov, F. V. Houard, V. M. Le Corre, A. Rahimi Chatri, P. Christodoulis and L. J. A. Koster, *ACS Appl. Mater. Interfaces*, 2019, **11**, 8310-8318.
75. B. Wang, Y. Y. Fu, C. Yan, R. Zhang, Q. Q. Yang, Y. C. Han and Z. Y. Xie, *Front. Chem.*, 2018, **6**, 198.
76. W. T. Hadmojo, F. T. A. Wibowo, D. Y. Ryu, I. H. Jung and S. Y. Jang, *ACS Appl. Mater. Interfaces*, 2017, **9**, 32939-32945.
77. B. Kan, M. Li, Q. Zhang, F. Liu, X. Wan, Y. Wang, W. Ni, G. Long, X. Yang, H. Feng, Y. Zuo, M. Zhang, F. Huang, Y. Cao, T. P. Russell and Y. Chen, *J. Am. Chem. Soc.*, 2015, **137**, 3886-3893.
78. M. Babics, T. N. Duan, A. H. Balawi, R. Z. Liang, F. Cruciani, I. D. Carja, D. Gottlieb, I. McCulloch, K. Vandewal, F. Laquai and P. M. Beaujuge, *ACS Appl. Energy Mater.*, 2019, **2**,

2717-2722.
79. W. T. Hadmojo, F. T. A. Wibowo, W. Lee, H. K. Jang, Y. Kim, S. Sinaga, M. Park, S. Y. Ju, D. Y. Ryu, I. H. Jung and S. Y. Jang, *Adv. Funct. Mater.*, 2019, **29**, 1808731.
80. R. Z. Liang, Y. Zhang, V. Savikhin, M. Babics, Z. Kan, M. Wohlfahrt, N. Wehbe, S. Liu, T. Duan, M. F. Toney, F. Laquai and P. M. Beaujuge, *Adv. Energy Mater.*, 2019, **9**, 1802836.
81. V. D. Mihailetchi, L. J. Koster, J. C. Hummelen and P. W. Blom, *Phys. Rev. Lett.*, 2004, **93**, 216601.
82. X. L. Ma, Y. Mi, F. J. Zhang, Q. S. An, M. Zhang, Z. H. Hu, X. F. Liu, J. Zhang and W. H. Tang, *Adv. Energy Mater.*, 2018, **8**, 1702854.
83. V. D. Mihailetchi, J. Wildeman and P. W. Blom, *Phys. Rev. Lett.*, 2005, **94**, 126602.
84. L. Zhang, N. Yi, W. Zhou, Z. Yu, F. Liu and Y. Chen, *Adv. Sci.*, 2019, **6**, 1900565.
85. Y. S. Chen, P. Ye, Z. G. Zhu, X. L. Wang, L. Yang, X. Z. Xu, X. X. Wu, T. Dong, H. Zhang, J. H. Hou, F. Liu and H. Huang, *Adv. Mater.*, 2017, **29**, 1603154.
86. X. Xu, Z. Bi, W. Ma, Z. Wang, W. C. H. Choy, W. Wu, G. Zhang, Y. Li and Q. Peng, *Adv. Mater.*, 2017, **29**, 1704271.
87. L. Y. Lu, W. Chen, T. Xu and L. P. Yu, *Nat. Commun.*, 2015, **6**, 7327.
88. A. K. Kyaw, D. H. Wang, V. Gupta, W. L. Leong, L. Ke, G. C. Bazan and A. J. Heeger, *ACS Nano*, 2013, **7**, 4569-4577.
89. H. N. Tran, D. H. Kim, S. Park and S. Cho, *Curr. Appl. Phys.*, 2018, **18**, 534-540.
90. C. G. Shuttle, A. Maurano, R. Hamilton, B. O'Regan, J. C. de Mello and J. R. Durrant, *Appl. Phys. Lett.*, 2008, **93**, 183501.
91. H. Jiang, X. Li, J. Wang, S. Qiao, Y. Zhang, N. Zheng, W. Chen, Y. Li and R. Yang, *Adv. Funct. Mater.*, 2019, **29**, 1903596.
92. V. C. Nikolis, J. Benduhn, F. Holzmueller, F. Piersimoni, M. Lau, O. Zeika, D. Neher, C. Koerner, D. Spoltore and K. Vandewal, *Adv. Energy Mater.*, 2017, **7**, 1700855.
93. S. M. Menke, N. A. Ran, G. C. Bazan and R. H. Friend, *Joule*, 2018, **2**, 25-35.
94. S. Ullbrich, J. Benduhn, X. Jia, V. C. Nikolis, K. Tvingstedt, F. Piersimoni, S. Roland, Y. Liu, J. Wu, A. Fischer, D. Neher, S. Reineke, D. Spoltore and K. Vandewal, *Nat. Mater.*, 2019, **18**, 459-464.
95. G. C. Han and Y. P. Yi, *Adv. Theory Simul.*, 2019, **2**, 1900067.
96. A. Karki, A. J. Gillett, R. H. Friend and T.-Q. Nguyen, *Adv. Energy Mater.*, 2021, **11**, 2003441.
97. M. Kim, S. U. Ryu, S. A. Park, K. Choi, T. Kim, D. Chung and T. Park, *Adv. Funct. Mater.*, 2020, **30**, 1904545.
98. S. E. Root, S. Savagatrup, A. D. Printz, D. Rodriquez and D. J. Lipomi, *Chem. Rev.*, 2017, **117**,

6467-6499.

99. J. W. Jung and W. H. Jo, *Chemistry of Materials*, 2015, **27**, 6038-6043.

100. S. U. Ryu, Z. Abbas, A. Cho, H. Lee, C. E. Song, H. K. Lee, S. K. Lee, W. S. Shin, S.-J. Moon, T. Park, H. I. Kim and J.-C. Lee, *Adv. Energy Mater.*, 2020, **10**, 1903846.

101. J. Song, C. Li, L. Zhu, J. Guo, J. Xu, X. Zhang, K. Weng, K. Zhang, J. Min, X. Hao, Y. Zhang, F. Liu and Y. Sun, *Adv. Mater.*, 2019, **31**, 1905645.

102. J. Yuan, Y. Zhang, L. Zhou, G. Zhang, H.-L. Yip, T.-K. Lau, X. Lu, C. Zhu, H. Peng, P. A. Johnson, M. Leclerc, Y. Cao, J. Ulanski, Y. Li and Y. Zou, *Joule*, 2019, **3**, 1140-1151.

103. K. Jiang, Q. Wei, J. Y. L. Lai, Z. Peng, H. K. Kim, J. Yuan, L. Ye, H. Ade, Y. Zou and H. Yan, *Joule*, 2019, **3**, 3020-3033.

104. C. Sun, S. Qin, R. Wang, S. Chen, F. Pan, B. Qiu, Z. Shang, L. Meng, C. Zhang, M. Xiao, C. Yang and Y. Li, *J. Am. Chem. Soc.*, 2020, **142**, 1465-1474.

105. Z. Zhou, W. Liu, G. Zhou, M. Zhang, D. Qian, J. Zhang, S. Chen, S. Xu, C. Yang, F. Gao, H. Zhu, F. Liu and X. Zhu, *Adv. Mater.*, 2020, **32**, 1906324.

106. J. Lv, H. Tang, J. Huang, C. Yan, K. Liu, Q. Yang, D. Hu, R. Singh, J. Lee, S. Lu, G. Li and Z. Kan, *Energy Environ. Sci.*, 2021, **14**, 3044-3052.

107. X. Xue, K. Weng, F. Qi, Y. Zhang, Z. Wang, J. Ali, D. Wei, Y. Sun, F. Liu and M. Wan, *Adv. Energy Mater.*, 2019, **9**, 1802686.

108. H. Li, G. Sini, J. Sit, A. J. Moulé and J.-L. Bredas, *Energy Environ. Sci.*, 2020, **13**, 601-615.

109. Y. L. Lin, M. A. Fusella and B. P. Rand, *Adv. Energy Mater.*, 2018, **8**, 1702816.

110. K. A. Mazzio and C. K. Luscombe, *Chemical Society Reviews*, 2015, **44**, 78-90.

111. H. Lee, C. Park, D. H. Sin, J. H. Park and K. Cho, *Adv. Mater.*, 2018, **30**, 1800453.

112. L. Liu, Y. Kan, K. Gao, J. Wang, M. Zhao, H. Chen, C. Zhao, T. Jiu, A.-K.-Y. Jen and Y. Li, *Adv. Mater.*, 2020, **32**, 1907604.

113. J. Han, F. Bao, D. Huang, X. Wang, C. Yang, R. Yang, X. Jian, J. Wang, X. Bao and J. Chu, *Adv. Funct. Mater.*, 2020, **30**, 2003654.

114. C. McDowell, M. Abdelsamie, K. Zhao, D. M. Smilgies, G. C. Bazan and A. Amassian, *Adv. Energy Mater.*, 2015, **5**, 1501121.

115. J. Oh, S. Jung, M. Jeong, B. Lee, J. Lee, Y. Cho, S. M. Lee, S. Chen, Z.-G. Zhang, Y. Li and C. Yang, *J. Mater. Chem. C*, 2019, **7**, 4716-4724.

116. A. L. Kanibolotsky, I. F. Perepichka and P. J. Skabara, *Chem. Soc. Rev.*, 2010, **39**, 2695-2728.

117. J. M. Ren, T. G. McKenzie, Q. Fu, E. H. H. Wong, J. Xu, Z. An, S. Shanmugam, T. P. Davis, C. Boyer and G. G. Qiao, *Chem. Rev.*, 2016, **116**, 6743-6836.

118. C. McDowell, M. Abdelsamie, M. F. Toney and G. C. Bazan, *Adv. Mater.*, 2018, **30**, 1707114.

119. H. Y. Chung, J. Oh, J.-H. Park, I. Cho, W. S. Yoon, J. E. Kwon, D. Kim and S. Y. Park, *J. Phys. Chem.*, 2020, **124**, 18502-18512.
120. J. Zhang, H. S. Tan, X. Guo, A. Facchetti and H. Yan, *Nat. Energy*, 2018, **3**, 720-731.
121. Y. Lin, J. Wang, Z.-G. Zhang, H. Bai, Y. Li, D. Zhu and X. Zhan, *Adv. Mater.*, 2015, **27**, 1170-1174.
122. Y. Lin, Z.-G. Zhang, H. Bai, J. Wang, Y. Yao, Y. Li, D. Zhu and X. Zhan, *Energy Environ. Sci.*, 2015, **8**, 610-616.
123. Y. Lin, F. Zhao, Q. He, L. Huo, Y. Wu, T. C. Parker, W. Ma, Y. Sun, C. Wang, D. Zhu, A. J. Heeger, S. R. Marder and X. Zhan, *J. Am. Chem. Soc.*, 2016, **138**, 4955-4961.
124. W. Zhao, S. Li, H. Yao, S. Zhang, Y. Zhang, B. Yang and J. Hou, *J. Am. Chem. Soc.*, 2017, **139**, 7148-7151.
125. W. Wu, G. Zhang, X. Xu, S. Wang, Y. Li and Q. Peng, *Advan. Funct. Mater.*, 2018, **28**, 1707493.
126. S. Holliday, R. S. Ashraf, C. B. Nielsen, M. Kirkus, J. A. Röhr, C.-H. Tan, E. Collado-Fregoso, A.-C. Knall, J. R. Durrant, J. Nelson and I. McCulloch, *J. Am. Chem. Soc.*, 2015, **137**, 898-904.
127. K. Wang, Y. Firdaus, M. Babics, F. Cruciani, Q. Saleem, A. El Labban, M. A. Alamoudi, T. Marszalek, W. Pisula, F. Laquai and P. M. Beaujuge, *Chem. Mater.*, 2016, **28**, 2200-2208.
128. H. I. Kim, M. Kim, C. W. Park, H. U. Kim, H.-K. Lee and T. Park, *Chem. Mater.*, 2017, **29**, 6793-6798.
129. G. D'Avino, L. Muccioli, F. Castet, C. Poelking, D. Andrienko, Z. G. Soos, J. Cornil and D. Beljonne, *J. Phys.: Condens. Matter*, 2016, **28**, 433002.
130. J. Fu, S. Chen, K. Yang, S. Jung, J. Lv, L. Lan, H. Chen, D. Hu, Q. Yang, T. Duan, Z. Kan, C. Yang, K. Sun, S. Lu, Z. Xiao and Y. Li, *iScience*, 2020, **23**, 100965.
131. Q. An, J. Wang, X. Ma, J. Gao, Z. Hu, B. Liu, H. Sun, X. Guo, X. Zhang and F. Zhang, *Energy Environ. Sci.*, 2020, **13**, 5039-5047.
132. H. Wang, Z. Zhang, J. Yu, X. Liu, S. Qu, S. Guang and W. Tang, *J. Mater. Chem. A*, 2019, **7**, 21903-21910.
133. P. Bi, F. Zheng, X. Yang, M. Niu, L. Feng, W. Qin and X. Hao, *J. Mater. Chem. A*, 2017, **5**, 12120-12130.
134. Y.-C. Huang, C.-S. Tsao, C.-M. Chuang, C.-H. Lee, F.-H. Hsu, H.-C. Cha, C.-Y. Chen, T.-H. Lin, C.-J. Su, U. S. Jeng and W.-F. Su, *J. Phys. Chem.*, 2012, **116**, 10238-10244.
135. H.-C. Liao, C.-S. Tsao, T.-H. Lin, C.-M. Chuang, C.-Y. Chen, U. S. Jeng, C.-H. Su, Y.-F. Chen and W.-F. Su, *J. Am. Chem. Soc.*, 2011, **133**, 13064-13073.
136. W. Zheng and R. B. Best, *J. Mol. Biol.*, 2018, **430**, 2540-2553.
137. S. Y. Son, Y. Kim, J. Lee, G.-Y. Lee, W.-T. Park, Y.-Y. Noh, C. E. Park and T. Park, *J. Am. Chem.*

Soc., 2016, **138**, 8096-8103.

138. L. Zhu, M. Zhang, G. Zhou, T. Hao, J. Xu, J. Wang, C. Qiu, N. Prine, J. Ali, W. Feng, X. Gu, Z. Ma, Z. Tang, H. Zhu, L. Ying, Y. Zhang and F. Liu, *Adv. Energy Mater.*, 2020, **10**, 1904234.
139. R. Hamilton, C. G. Shuttle, B. O'Regan, T. C. Hammant, J. Nelson and J. R. Durrant, *J. Phys. Chem. Lett.*, 2010, **1**, 1432-1436.
140. W. Gao, T. Liu, R. Sun, G. Zhang, Y. Xiao, R. Ma, C. Zhong, X. Lu, J. Min, H. Yan and C. Yang, *Adv. Sci.*, 2020, **7**, 1902657.
141. J. F. Guillemoles, T. Kirchartz, D. Cahen and U. Rau, *Nat. Photonics*, 2019, **13**, 501-505.
142. D. Veldman, S. C. J. Meskers and R. A. J. Janssen, *Adv. Funct. Mater.*, 2009, **19**, 1939-1948.
143. U. Rau, B. Blank, T. C. M. Müller and T. Kirchartz, *Phys. Rev. Appl.*, 2017, **7**, 044016.
144. Q. Wang, Y. P. Qin, M. M. Li, L. Ye and Y. H. Geng, *Adv. Energy Mater.*, 2020, **10**, 26.
145. W. Liu, X. Xu, J. Yuan, M. Leclerc, Y. P. Zou and Y. F. Li, *ACS Energy Lett.*, 2021, **6**, 598-608.
146. Y. Wang, J. Lee, X. Hou, C. Labanti, J. Yan, E. Mazzolini, A. Parhar, J. Nelson, J. S. Kim and Z. Li, *Adv. Energy Mater.*, 2020, **11**, 41.
147. F. W. Zhao, H. T. Zhang, R. Zhang, J. Yuan, D. He, Y. P. Zou and F. Gao, *Adv. Energy Mater.*, 2020, **10**, 20.
148. A. Karki, A. J. Gillett, R. H. Friend and T. Q. Nguyen, *Adv. Energy Mater.*, 2020, **11**, 30.
149. J. Yao, B. Qiu, Z. G. Zhang, L. Xue, R. Wang, C. Zhang, S. Chen, Q. Zhou, C. Sun, C. Yang, M. Xiao, L. Meng and Y. Li, *Nat. Commun.*, 2020, **11**, 2726.
150. H. N. Tran, S. Park, F. T. A. Wibowo, N. V. Krishna, J. H. Kang, J. H. Seo, H. Nguyen-Phu, S. Y. Jang and S. Cho, *Adv. Sci.*, 2020, **7**, 2002395.
151. Q. Liu, Y. Jiang, K. Jin, J. Qin, J. Xu, W. Li, J. Xiong, J. Liu, Z. Xiao and K. Sun, *Sci. Bull.*, 2020, **65**, 272-275.
152. W. Zhao, S. Li, H. Yao, S. Zhang, Y. Zhang, B. Yang and J. Hou, *J. Am. Chem. Soc.*, 2017, **139**, 7148-7151.
153. S. Li, L. Ye, W. Zhao, H. Yan, B. Yang, D. Liu, W. Li, H. Ade and J. Hou, *J. Am. Chem. Soc.*, 2018, **140**, 7159-7167.
154. D. Kim, J. Ryu, F. T. A. Wibowo, S. Y. Park, J. Y. Kim, S. Y. Jang and S. Cho, *ACS Appl. Energy Mater.*, 2020, **3**, 8375-8382.
155. S. K. Hau, H. L. Yip, N. S. Baek, J. Y. Zou, K. O'Malley and A. K. Y. Jen, *Appl. Phys. Lett.*, 2008, **92**, 3.
156. Z. C. He, C. M. Zhong, S. J. Su, M. Xu, H. B. Wu and Y. Cao, *Nat. Photonics*, 2012, **6**, 591-595.
157. F. Hermerschmidt, A. Savva, E. Georgiou, S. M. Tuladhar, J. R. Durrant, I. McCulloch, D. D.

C. Bradley, C. J. Brabec, J. Nelson and S. A. Choulis, *ACS Appl. Mater. Interfaces*, 2017, **9**, 14136-14144.

158. C. Tao, S. P. Ruan, X. D. Zhang, G. H. Xie, L. Shen, X. Z. Kong, W. Dong, C. X. Liu and W. Y. Chen, *Appl. Phys. Lett.*, 2008, **93**, 3.

159. N. K. Elumalai, A. Saha, C. Vijila, R. Jose, Z. Jie and S. Ramakrishna, *Phys. Chem. Chem. Phys.*, 2013, **15**, 6831-6841.

160. Y. Sun, J. H. Seo, C. J. Takacs, J. Seifter and A. J. Heeger, *Adv. Mater.*, 2011, **23**, 1679-1683.

161. M. J. Tan, S. Zhong, J. Li, Z. Chen and W. Chen, *ACS Appl. Mater. Interfaces*, 2013, **5**, 4696-4701.

162. Z. Q. Liang, Q. F. Zhang, L. Jiang and G. Z. Cao, *Energy Environ. Sci.*, 2015, **8**, 3442-3476.

163. S. R. Cowan, P. Schulz, A. J. Giordano, A. Garcia, B. A. MacLeod, S. R. Marder, A. Kahn, D. S. Ginley, E. L. Ratcliff and D. C. Olson, *Adv. Funct. Mater.*, 2014, **24**, 4671-4680.

164. S. Kumar, D. Panigrahi and A. Dhar, *Appl. Surf. Sci.*, 2018, **435**, 855-862.

165. B. R. Lee, E. D. Jung, Y. S. Nam, M. Jung, J. S. Park, S. Lee, H. Choi, S. J. Ko, N. R. Shin, Y. K. Kim, S. O. Kim, J. Y. Kim, H. J. Shin, S. Cho and M. H. Song, *Adv. Mater.*, 2014, **26**, 494-500.

166. B. Wang, M. Zhang, X. Cui, Z. Wang, M. Rager, Y. Yang, Z. Zou, Z. L. Wang and Z. Lin, *Angew. Chem. Int. Ed. Engl.*, 2020, **59**, 1611-1618.

167. A. Klasen, P. Baumli, Q. Sheng, E. Johannes, S. A. Bretschneider, I. M. Hermes, V. W. Bergmann, C. Gort, A. Axt, S. A. L. Weber, H. Kim, H. J. Butt, W. Tremel and R. Berger, *J. Phys. Chem. C*, 2019, **123**, 13458-13466.

168. L. Nian, W. Zhang, S. Wu, L. Qin, L. Liu, Z. Xie, H. Wu and Y. Ma, *ACS Appl. Mater. Interfaces*, 2015, **7**, 25821-25827.

169. C. Z. Li, J. Huang, H. Ju, Y. Zang, J. Zhang, J. Zhu, H. Chen and A. K. Jen, *Adv. Mater.*, 2016, **28**, 7269-7275.

170. S. K. Hau, H. L. Yip, H. Ma and A. K. Y. Jen, *Appl. Phys. Lett.*, 2008, **93**, 441.

171. Y. E. Ha, M. Y. Jo, J. Park, Y.-C. Kang, S. I. Yoo and J. H. Kim, *J. Phys. Chem.*, 2013, **117**, 2646-2652.

172. R. Azmi, C. L. Lee, I. H. Jung and S. Y. Jang, *Adv. Energy Mater.*, 2018, **8**, 1702934.

173. R. Azmi, S. H. Oh and S. Y. Jang, *ACS Energy Lett.*, 2016, **1**, 100-106.

174. S. Bai, Y. Z. Jin, X. Y. Liang, Z. Z. Ye, Z. W. Wu, B. Q. Sun, Z. F. Ma, Z. Tang, J. P. Wang, U. Wurfel, F. Gao and F. L. Zhang, *Adv. Energy Mater.*, 2015, **5**, 1401606.

175. J. C. Yu, D. B. Kim, G. Baek, B. R. Lee, E. D. Jung, S. Lee, J. H. Chu, D. K. Lee, K. J. Choi, S. Cho and M. H. Song, *Adv. Mater.*, 2015, **27**, 3492-3500.

176. X. P. Xu, M. Deng, Y. W. Lee, H. Y. Woo, X. H. Zou, Y. Jiang, L. Y. Yu, Y. Li and Q. Peng, *J. Mater. Chem. A*, 2019, **7**, 24937-24946.
177. T. Liu, Z. Luo, Y. Chen, T. Yang, Y. Xiao, G. Zhang, R. Ma, X. Lu, C. Zhan, M. Zhang, C. Yang, Y. Li, J. Yao and H. Yan, *Energy Environ. Sci.*, 2019, **12**, 2529-2536.
178. B. Fan, D. Zhang, M. Li, W. Zhong, Z. Zeng, L. Ying, F. Huang and Y. Cao, *Sci. China Chem.*, 2019, **62**, 746-752.
179. Y. Chang, T.-K. Lau, M.-A. Pan, X. Lu, H. Yan and C. Zhan, *Mater. Horizons*, 2019, **6**, 2094-2102.
180. T. Wang, J. Qin, Z. Xiao, X. Meng, C. Zuo, B. Yang, H. Tan, J. Yang, S. Yang, K. Sun, S. Xie and L. Ding, *Sci. Bull.*, 2020, **65**, 179-181.
181. C. Sun, F. Pan, S. Chen, R. Wang, R. Sun, Z. Shang, B. Qiu, J. Min, M. Lv, L. Meng, C. Zhang, M. Xiao, C. Yang and Y. Li, *Adv. Mater.*, 2019, **31**, e1905480.
182. Q. An, X. Ma, J. Gao and F. Zhang, *Sci. Bull.*, 2019, **64**, 504-506.
183. D. Su, M.-A. Pan, Z. Liu, T.-K. Lau, X. Li, F. Shen, S. Huo, X. Lu, A. Xu, H. Yan and C. Zhan, *Chem. of Mater.*, 2019, **31**, 8908-8917.
184. L. Hong, H. Yao, Z. Wu, Y. Cui, T. Zhang, Y. Xu, R. Yu, Q. Liao, B. Gao, K. Xian, H. Y. Woo, Z. Ge and J. Hou, *Adv. Mater.*, 2019, **31**, e1903441.
185. H. Sun, T. Liu, J. Yu, T.-K. Lau, G. Zhang, Y. Zhang, M. Su, Y. Tang, R. Ma, B. Liu, J. Liang, K. Feng, X. Lu, X. Guo, F. Gao and H. Yan, *Energy Environ. Sci.*, 2019, **12**, 3328-3337.
186. Y. Cui, H. Yao, J. Zhang, T. Zhang, Y. Wang, L. Hong, K. Xian, B. Xu, S. Zhang, J. Peng, Z. Wei, F. Gao and J. Hou, *Nat. Commun.*, 2019, **10**, 2515.
187. R. Yu, H. Yao, Y. Cui, L. Hong, C. He and J. Hou, *Adv. Mater.*, 2019, **31**, e1902302.
188. K. Li, Y. Wu, Y. Tang, M. A. Pan, W. Ma, H. Fu, C. Zhan and J. Yao, *Adv. Energy Mater.*, 2019, **9**, 11.
189. Y. Wu, Y. Zheng, H. Yang, C. Sun, Y. Dong, C. Cui, H. Yan and Y. Li, *Sci. China Chem.*, 2019, **63**, 265-271.
190. T. Yan, J. Ge, T. Lei, W. Zhang, W. Song, B. Fanady, D. Zhang, S. Chen, R. Peng and Z. Ge, *J. Mater. Chem. A*, 2019, **7**, 25894-25899.
191. Q. Liao, Q. Kang, Y. Yang, C. An, B. Xu and J. Hou, *Adv. Mater.*, 2020, **32**, e1906557.
192. T. Yan, W. Song, J. Huang, R. Peng, L. Huang and Z. Ge, *Adv. Mater.*, 2019, **31**, e1902210.
193. M.-A. Pan, T.-K. Lau, Y. Tang, Y.-C. Wu, T. Liu, K. Li, M.-C. Chen, X. Lu, W. Ma and C. Zhan, *J. Mater. Chem. A*, 2019, **7**, 20713-20722.
194. J. Gao, J. Wang, Q. An, X. Ma, Z. Hu, C. Xu, X. Zhang and F. Zhang, *Sci. China Chem.*, 2019, **63**, 83-91.

195. J. Xiong, K. Jin, Y. Jiang, J. Qin, T. Wang, J. Liu, Q. Liu, H. Peng, X. Li, A. Sun, X. Meng, L. Zhang, L. Liu, W. Li, Z. Fang, X. Jia, Z. Xiao, Y. Feng, X. Zhang, K. Sun, S. Yang, S. Shi and L. Ding, *Sci. Bull.*, 2019, **64**, 1573-1576.
196. K. Jiang, Q. Y. Wei, J. Y. L. Lai, Z. X. Peng, H. Kim, J. Yuan, L. Ye, H. Ade, Y. P. Zou and H. Yan, *Joule*, 2019, **3**, 3020-3033.
197. Y. Cui, H. Yao, L. Hong, T. Zhang, Y. Tang, B. Lin, K. Xian, B. Gao, C. An, P. Bi, W. Ma and J. Hou, *Nat. Sci. Rev.*, 2020, **7**, 1239-1246.
198. Y. Lin, B. Adilbekova, Y. Firdaus, E. Yengel, H. Faber, M. Sajjad, X. Zheng, E. Yarali, A. Seitkhan, O. M. Bakr, A. El-Labban, U. Schwingenschlogl, V. Tung, I. McCulloch, F. Laquai and T. D. Anthopoulos, *Adv. Mater.*, 2019, **31**, e1902965.
199. L. Zhan, S. Li, T.-K. Lau, Y. Cui, X. Lu, M. Shi, C.-Z. Li, H. Li, J. Hou and H. Chen, *Energy Environ. Sci.*, 2020, **13**, 635-645.
200. Q. An, J. Wang, W. Gao, X. Ma, Z. Hu, J. Gao, C. Xu, M. Hao, X. Zhang, C. Yang and F. Zhang, *Sci. Bull.*, 2020, **65**, 538-545.
201. D. Li, X. Chen, J. Cai, W. Li, M. Chen, Y. Mao, B. Du, J. A. Smith, R. C. Kilbride, M. E. O'Kane, X. Zhang, Y. Zhuang, P. Wang, H. Wang, D. Liu, R. A. L. Jones, D. G. Lidzey and T. Wang, *Sci. China Chem.*, 2020, **63**, 1461-1468.
202. M. Zhang, L. Zhu, T. Hao, G. Zhou, C. Qiu, Z. Zhao, N. Hartmann, B. Xiao, Y. Zou, W. Feng, H. Zhu, M. Zhang, Y. Zhang, Y. Li, T. P. Russell and F. Liu, *Adv. Mater.*, 2021, **33**, e2007177.
203. W. Shockley and H. J. Queisser, *J. Appl. Phys.*, 1961, **32**, 510-519.
204. T. Kirchartz and U. Rau, *Phys. Status Solidi (A) Appl. Mater. Sci.*, 2008, **205**, 2737-2751.
205. U. Rau, B. Blank, T. C. M. Muller and T. Kirchartz, *Phys. Rev. Appl.*, 2017, **7**, 044016.
206. N. Aristidou, C. Eames, I. Sanchez-Molina, X. Bu, J. Kosco, M. S. Islam and S. A. Haque, *Nat. Commun.*, 2017, **8**, 15218.
207. P. Cheng and X. Zhan, *Chem. Soc. Rev.*, 2016, **45**, 2544-2582.
208. A. Seemann, T. Sauermann, C. Lungenschmied, O. Armbruster, S. Bauer, H. J. Egelhaaf and J. Hauch, *Sol. Energy*, 2011, **85**, 1238-1249.
209. J. Schafferhans, A. Baumann, A. Wagenpfahl, C. Deibel and V. Dyakonov, *Org. Electron.*, 2010, **11**, 1693-1700.

국문 초록

유기 태양전지의 성능 향상을 위한 효과적인 전략에 대한 연구

울산대학교 대학원

물 리 학 과

김 도 희

이산화탄소 배출량 급증으로 야기된 전 지구적 기후변화와 같은 심각한 환경 문제 극복을 위해 신재생 에너지 기술 개발이 활발히 이루어지고 있다. 유기태양전지는 손쉬운 가동성과 낮은 생산 비용, 기계적 유연성 등의 장점으로 인해 미래 에너지원으로 많은 주목을 받고 있다. 최근, 근적외선 영역 흡수를 갖고 물질의 화학적 구조와 에너지 레벨 조절이 가능한 non-fullerene acceptor (NFA)가 개발되어 18% 이상의 광전변환 효율을 갖는 유기태양전지가 구현되었다. 그러나 상용화를 위해 더 높은 광전변환 효율과 장기 안정성이 필요하다.

일반적인 유기태양전지의 구동은 광 유도 전하이동 현상을 기반으로 한다. 입사된 빛에 의해 여기된 전자-정공쌍은 엑시톤을 형성하고, 형성된 엑시톤은 donor-acceptor의 경계에서 분리된다. 따라서 엑시톤의 효과적인 분리는 유기태양전지 광전변환 효율에 상당한 영향을 미친다. 엑시톤 분리는 donor와 acceptor 계면에서 발생하기 때문에 각 donor와 acceptor의 phase가 엑시톤 확산거리보다 클 경우, 엑시톤은 donor와 acceptor 계면에 도달하기 전에 재결합된다. 따라서, 적절한 phase를 형성하도록 광 흡수층의 morphology를 최적화하는 것은 광전변환 효율 향상을 위한 필수 요소 중 하나이다. 또한, charge transfer state와 interface trap을 포함하는 다양한 trap sites를 제거하는 것도 유기태양전지의 높은 광전변환 효율과 안정성을 얻기 위한 필수 요소이다. 따라서 본 연구에서는 유기태양전지의 성능 향상과 안정성 확보를 위해 ternary blend, additive engineering, 계면 처리법 등 다양한 기술들을 적용해 보았다.

첫번째, 큰 에너지 손실 특성을 갖는 fullerene 기반 유기태양전지의 에너지 손실 문제 완화를 위해 ternary blend system을 적용하였다. Wide bandgap을 갖는 polymer donor인 PBDTTPD-HT와 $PC_{71}BM$ 기반의 binary system에 단분자 donor인 DRCN5T를 도입하여 ternary blend system의 광 흡수층을 형성하였다. 도입된 DRCN5T는 bridge 역할을 하여 PBDTTPD-HT에

서 $PC_{71}BM$으로 간접적 전자 이동을 가능하게 하였고, cascading charge transfer를 형성하였다. 결과적으로 소량의 DRCN5T를 PBDTTPD-HT:$PC_{71}BM$에 도입하여 PBDTTPD-HT와 $PC_{71}BM$ 간 deep charge transfer state를 피함으로써 V_{OC}를 증가시키고 소자의 광전변환 효율을 향상 시켰다.

두번째, PM6:Y6를 기반으로 하는 광 흡수층에 solid-solvent hybrid additive법을 적용하여 donor와 acceptor의 macroscopic phase separation과 π-π stacking, orientation과 같은 microscopic morphology를 동시에 최적화하였다. Solvent additive인 1-chloronaphthalene (CN)을 사용하여 광 흡수층의 macroscopic morphology를 최적화하고, 새롭게 합성한 3D 구조의 Star-A 또는 Star-F solid additive를 사용하여 microscopic morphology를 최적화하였다. Solid additive가 morphology에 미치는 영향을 grazing-incidence small-angle X-ray scattering (GISAXS)와 grazing-incidence wide-angle X-ray scattering (GIWAXS) 측정을 통해 확인한 결과, intermolecular π-π stacking과 phase separation을 향상시키는 것을 확인하였다. 따라서 1%의 소량 solid additive와 solvent additive를 hybrid로 사용하여 광 흡수층의 morphology를 최적화함으로써 소자의 성능을 향상시켰다.

세번째, 유기태양전지의 성능 향상과 장기 안정성 확보를 위해 계면 처리법을 적용하였다. 광 흡수층과 금속 산화물 기반 전자 수송층 계면에서 발생하는 deep trap과 유입된 산소로 인한 shallow trap은 trap-assisted 재결합을 증가시키고 charge extraction 효율을 감소시켜 소자의 V_{OC}와 장기 안정성 저하를 가져온다. 이에 광 흡수층과 전자 수송층 계면 결함을 화학적 처리를 통해 억제하였다. 이는 소자 효율을 17.43%로 향상시키고, 소자 안정성을 1200 시간 동안 90%로 유지시켰다.

결론적으로 본 연구에서는 ternary blend와 additive engineering, 계면 처리법을 이용하여 광 흡수층의 morphology를 최적화하고 defect state를 억제함으로써, 유기태양전지의 성능 향상과 장기 안정성 확보를 위한 다양한 전략들을 제시한다.